ANTONIO CAPRETTI

LINEAR AND NONLINEAR PLASMONICS

LINEAR AND NONLINEAR PLASMONICS

ANTONIO CAPRETTI

M.D., Università degli Studi di Napoli Federico II, 2009
B.D., Università degli Studi di Napoli Federico II, 2007

Dissertation submitted in partial fulfillment of the requirements for the

DOCTORAL DEGREE IN ELECTRICAL ENGINEERING

Department of Electrical Engineering and Information Technology
Università degli Studi di Napoli Federico II

March 31st, 2013

The content of the present Dissertation has been partially developed in the Electrical Engineering and Computer Science Department of Boston University, within the Nanomaterials and Nanostructure Optics group of Prof. Luca Dal Negro. Specifically, all the experimental activities on Nonlinear Plasmonics have been performed in Boston.

Antonio Capretti: *Linear and Nonlinear Plasmonics,* Dissertation submitted in partial fulfillment of the requirements for the Doctoral Degree in Electrical Engineering, March 31st, 2013

LINEAR AND NONLINEAR PLASMONICS

ANTONIO CAPRETTI

Department of Electrical Engineering and Information Technology
Università degli Studi di Napoli Federico II

Doctoral supervisors (alphabetical order):
PROF. LUCA DAL NEGRO
Department of Electrical Engineering and Computer Science
Boston University
PROF. GIOVANNI MIANO
Department of Electrical Engineering and Information Technology
Università degli Studi di Napoli Federico II
PROF. GIOVANNI PIERO PEPE
Department of Physics & CNR-SPIN
Università degli Studi di Napoli Federico II

ABSTRACT

In the present Thesis, the electromagnetic properties of metal nanostructures are theoretically and experimentally investigated, for applications ranging from chemical sensing to integrated optical devices. Collective resonances of the conduction electrons occur on the surface of metal particles with nanoscale sizes, if visible or infrared light interacts with them. These resonances, usually referred to as Localized Surface Plasmons (LSPs), are able to confine the incident light into regions of sub-wavelength dimensions. The electric field in proximity of the metal surface can be orders of magnitude higher than the incident field. This effect, usually known as field enhancement, is traditionally used to increase the cross-section of optical phenomena, for instance the Raman scattering and the harmonic generation, by means of specific planar aggregates of metal nanoparticles, such as arrays and nanolenses.

IN THE FIRST PART OF THIS THESIS, NOVEL CONFIGURATIONS OF PLASMONIC NANOLENSES ARE ENGINEERED IN ORDER TO OPTIMIZE THE FIELD ENHANCEMENT AND THE SPECTRAL RESPONSE OF THE METAL NANOPARTICLES, AND GENERAL DESIGN RULES ARE DERIVED. Specifically, metal nanostructures composed by two different interacting metals, such as gold and silver, are studied. These devices, usually called heterostructures, feature very specific spectral properties, derived from the different LSP frequencies of the two metals. Their properties in planar arrangement for sensing applications are studied. Furthermore, an optimization method is applied to the engineering of plasmonic nanolenses. As a result, novel configurations are found that maximize the field enhancement in a selected probing point. The radiative coupling between the metal nanoparticles is found to be under-estimated in comparison with the near-field coupling, that was traditionally studied in the literature. These results are experimentally validated by surface-enhanced Raman scattering measurements.

In the second part of the Thesis, the nonlinear optical properties of metal nanoparticles are investigated, for both fundamental and practical purposes. Nonlinear Plasmonics is a promising field for the realization of integrated optical devices, but the origin of the second-order nonlinearities from metal nanostructures is not completely understood. Consequently, the relative contributions of the two main sources of nonlinearities, namely the metal surface and the bulk, are here investigated with the main goal to accurately design novel devices based on plasmonic nonlinear effects. First, the analytical solution of second-harmonic scattering from metal nanospheres is developed, by expanding the fields and the sources in vector spherical wavefunctions. For the first time, both the bulk and surface sources are considered in a full-wave approach. Then, second-harmonic generation measurements are performed on gold colloids, and multipolar contributions are found to be significant for large-size particles. The experimental results are combined with numerical calculations, and the relative contributions of surface and bulk sources are estimated for gold nanoparticles. Eventually, second-harmonic generation experiments are performed on planar arrays of gold nanoparticles, demonstrating the significant contributions of multipolar sources. In particular, their relative magnitude is found to be extremely sensitive to the array geometry and the particle distance.

In conclusion, in the present Thesis linear and nonlinear optical processes from plasmonic nanostructures are investigated. General principles for the design of plasmonic nanolenses are found. Moreover, the relative contributions of surface and bulk second-order sources are investigated for gold nanoparticles. Planar nanolenses and arrays are experimentally and theoretically investigated, for both linear and nonlinear photonic applications.

PUBLICATIONS

Some ideas and figures have appeared previously in the following publications:

- SECOND HARMONIC GENERATION IN METAL NANO-SPHERES: FULL-WAVE ANALYTICAL SOLUTION WITH BOTH LOCAL-SURFACE AND NONLOCAL-BULK NONLINEAR SOURCES
  Antonio Capretti, Carlo Forestiere, Luca Dal Negro and Giovanni Miano
  arXiv:1301.1628 [physics.optics] 2013, submitted for peer-review
- MULTIPOLAR SECOND HARMONIC GENERATION FROM PLANAR ARRAYS OF AU NANOPARTICLES
  Antonio Capretti, Gary F. Walsh, Salvatore Minissale, Jacob Trevino, Carlo Forestiere, Giovanni Miano, and Luca Dal Negro
  Optics Express, Vol. 20, Issue 14, pp. 15797-15806, 2012
- GENETICALLY ENGINEERED PLASMONIC NANOARRAYS
  Carlo Forestiere, Alyssa J. Pasquale, Antonio Capretti, Giovanni Miano, Antonello Tamburrino, Sylvanus Y. Lee, Bjorn M. Reinhard, and Luca Dal Negro
  Nano Lett., 2012, 12 (4), pp 2037-2044

- MULTIPOLAR SECOND HARMONIC GENERATION FROM PLASMONIC ARRAYS
  Antonio Capretti, Gary F. Walsh, Salvatore Minissale, Jacob Trevino, Carlo Forestiere, Giovanni Miano, and Luca Dal Negro
  Frontiers in Optics, Rochester NY, October 14th, 2012
- ENHANCED SECOND HARMONIC GENERATION FROM APERIODIC ARRAYS OF GOLD NANOPARTICLES
  Antonio Capretti, Gary F. Walsh, Jacob Trevino, Giovanni Miano, and Luca Dal Negro
  APS March Meeting 2012, Volume 57, Number 1, Boston MA, February 28th, 2012
- GENETIC OPTIMIZATION OF OPTICAL NANOANTENNAS
  Carlo Forestiere, Alyssa Pasquale, Antonio Capretti, Sylvanus Lee, Giovanni Miano, Antonello Tamburrino, Luca Dal Negro
  APS March Meeting 2012, Volume 57, Number 1, Boston MA, February 27th, 2012

to my family

ACKNOWLEDGMENTS

In 2010 I joined the Doctoral Course in Electrical Engineering at the University of Naples Federico II with the strong desire to explore the field of Plasmonics. I thank my Doctoral supervisors Prof. G. Miano, Prof. G. P. Pepe and Prof. L. Dal Negro for giving me the priceless possibility to investigate this exciting field with a multidisciplinary approach that has greatly enriched myself.

I first met Prof. G. Miano in 2008 during my M.D. studies. I express my gratitude to him for having continuously shared his wide knowledge with me during my Doctoral activity. His rigorous approach to the research has considerably shaped the present Dissertation. I thank him for his invaluable guidance.

Prof. G.P. Pepe was my M.D. Thesis supervisor in 2009. I would like to express my genuine thanks to him for his precious teachings and for having brought novel ideas and interesting collaborations to my Doctoral activity within the CNR-SPIN Institute.

Lastly, in chronological order, Prof. L. Dal Negro welcomed me in 2011 into his research group, where I spent half of my Doctoral studies. I am grateful to him for his fundamental guidance and for making many experimental resources available to me. He has also allowed me to carry research in the inspiring and international environment of the BU Photonics Center.

I wish to thank the Doctoral Coordinator Prof. G. Rubinacci for his constant support, and all the members of the Department of Electrical Engineering of the University of Naples Federico II. Additionally, I would like to thank Prof. C. De Rosa and Prof. F. Auriemma of the Department of Chemistry. I sincerely express my thanks to all the students and post-docs who shared their time with me in the laboratories, in front of a computer monitor or in the free time. I indeed thank Carlo, Emanuele, Salvo, Selcuk, Rocco, Alyssa, Gary, Sylvanus, Jacob, Nate, Lin, Alex, Tom and many others.

I wish to express once again my gratitude to my parents Mario and Rosanna, who have supported me and my studies for a very long time. I will never thank you enough. I thank them and my sister Chiara for being examples of workers of rare intensity. I thank Sara, who continuously supported me during my stay in Boston. The distance has made our special link more durable and strong.

Finally, I thank all the old and new friends who have been there for me, both in the new and the old continent.

CONTENTS

ACRONYMS

LSP	Localized Surface Plasmon
SPP	Surface Plasmon Polariton
SH	Second Harmonic
NIM	Negative Index Material
LHM	Left Handed Material
RHM	Right Handed Material
SVWF	Spherical Vector WaveFunction
NFE	Near Field Enhancement
SRR	Split Ring Resonator
SERS	Surface Enhanced Raman Scattering
EBL	Electron Beam Lithography
SEM	Scanning Electron Microscopy
BCP	Block CoPolymer
DNA	DeoxyRibonucleic Acid
SIE	Surface Integral Equation
VIE	Volume Integral Equation
GA	Genetic Algorithm
FDTD	Finite Difference Time Domain
FEM	Finite Element Method

Part I

INTRODUCTION AND GENERAL FRAMEWORK

1

BEYOND NATURAL MEDIA

Artificial media showing physical properties not found in natural ones are generally referred to as *metamaterials*. In principle, a large variety of physical properties can be artificially tuned, e. g. mechanical and acoustical [1, 2]. However, the most explored metamaterials are those involving electromagnetic properties [3, 4], ranging from the UV to the microwave electromagnetic spectrum. The onset of metamaterials in the scientific scenario has been catalyzed by a significant improvement of fabrication techniques. Nowadays, a large-scale accurate and reproducible patterning of a variety of materials at micro- and nano- scale is allowed [5, 6].

In the last decades, novel chemical techniques have been proposed, based on the spontaneous organization of elementary components (i. e. , atoms, molecules or more complex structures) into ordered patterns, by minimizing the total free energy of the system [7]. These *self-assembly* processes are usually led by weak interactions (e. g. , Van der Waals, hydrogen bonds, etc.), with respect to the the ones prevailing in solid crystals (e. g. , ionic, covalent, etc.). For instance, Block CoPolymers (BCPs) and DeoxyRibonucleic Acid (DNA) provide powerful technologies for realizing regular and programmable nanostructures [8, 9, 10].

Moreover, the lithography process has been recently brought to unexperienced levels by using electrons, instead of light, to impress nano-patterns over a resist [11]. The typical electron energy used in the Electron Beam Lithography (EBL) guarantees a much smaller definition than that provided by traditional lithography, affected by the optical diffraction limit. As a matter of fact, the EBL allows for the fabrication of nano-structures with features as small as $\sim 5\ \mathrm{nm}$, and this limit is overcome year after year [12, 13].

Eventually, the discovery of novel materials has enriched the variety of basic materials from which is possible to design complex nanoscale systems. For instance, highly ordered monodimensional (C_{60} fullerene), bidimensional (graphene) and tridimensional (nanotubes) structures based on carbon, have been shown to provide unique mechanical and electromagnetic properties [14, 15, 16]. Researchers are working worldwide to find the right spot for these new elements in current technological applications [17].

In conclusion, the improvement of micro-technology and the rise of nano-technology in the very last decades has allowed unforeseen opportunities for the fabrication of metamaterials with engineered properties[18, 19]. In particular, the electromagnetic response of a traditional material can be changed if its structure is regularly patterned with features much smaller than the incident electromagnetic wavelength. These considerations imply that the major applications for metamaterials are relevant at the optical, infrared and microwave wavelengths, with engineered material structures ranging from $10\ \mathrm{nm}$ to $10\ \mathrm{cm}$. Therefore, a large variety of metamaterials have been designed with unconventional electromagnetic properties, ranging from negative refractive index to enhanced nonlinear response [3, 20].

One of the most impressive achievement of the metamaterial research field is the control of the sign of the electromagnetic permittivity and permeability, in specific spectral ranges. In 1968 V. G. Veselago was the first to envision the relevance of fabricating materials with such optical properties, and he predicted the most relevant features [21]. In particular, for a isotropic lossless medium with electrical permittivity ε and magnetic permeability μ, four circumstances can happen, in relation with the signs of ε and μ, respectively: (I) $\varepsilon, \mu > 0$, (II) $\varepsilon < 0, \mu > 0$, (III) $\varepsilon, \mu < 0$ and (IV) $\varepsilon > 0, \mu < 0$, as shown in Fig. 1.1.

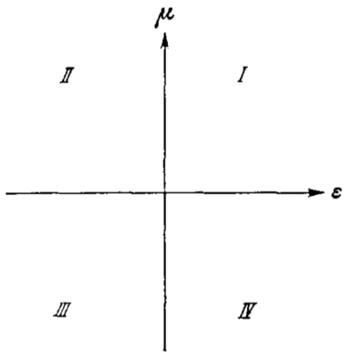

Figure 1.1: V. G. Veselago's partition of isotropic lossless media, depending on the signs of the permittivity ε and the permeability μ.

The case (I) in Fig. 1.1 is typical of almost all naturally-occurring materials. If we consider an e.m. plane wave traveling in these media, then the wavevector $\hat{\boldsymbol{k}}$, the electric field $\boldsymbol{E}$ and the magnetic field $\boldsymbol{M}$ form a right-handed triplet. For this reason, these substances are called Right Handed Materials (RHMs). Light reflection, refraction and propagation in RHMs follow the well-known rules of optics, i. e. the Snell's law, that basically agree with the common sense. On the contrary, the optical response of substances falling in the cases (II),(III) and (IV) is far from the common behavior of natural materials, and will be described in the next paragraphs.

1.1 PLASMONIC METAMATERIALS

The substances in the quadrant (II) of Fig. 1.1 display a negative electric permittivity ε and a positive magnetic permeability μ. These materials show a plasma-like response to an e.m. field . As a matter of fact, a plasma is a gas of charged particles, whose electric permittivity can be expressed, under opportune hypotheses, as $\varepsilon(\omega) = 1 - \omega_p^2/\omega^2$, where ω_p is a characteristic angular frequency called *plasma frequency*. Therefore, $\varepsilon < 0$ for $\omega < \omega_p$.

Historically, the first observation of the plasma response to an e.m. field , was the reflection of radio waves from the ionosphere of Earth. As a matter of fact, the ionosphere is a plasma constituted by atmospherical particles ionized by the sun radiation, characterized by $\omega_p \approx 5 \cdot 10^7 \mathrm{rad\,s^{-1}}$. A radio wave with lower ω than ω_p, propagating from the earth ground, experiences the total reflection from ionosphere, due to the negative permittivity at those frequencies [22].

Plasma-like systems are common also in solid state physics, and their study is called *Plasmonics*. In particular, it is well known [23, 24] that the conduction electrons in metals act as charges of a plasma. Consequently, metals display negative permittivity in a selected spectral range, mostly in the visible, conferring peculiar optical behavior. The main properties of electrons in metals will be rigorously discussed in Chapter 2.

THE MODELING AND DESIGN OF PLASMONIC METAMATERIALS WILL BE THE SUBJECT OF THE PRESENT THESIS. Their application to the linear and nonlinear optical regimes will be discussed in Parts (ii) and (iii), respectively. The basic electromagnetic properties of plasmonic metamaterials are now briefly introduced, and they will be examined in depth in the next Chapters.

Although plasmonic metamaterials can be made of a variety of materials, such as graphene [17], they are most commonly produced by manufacturing metals at nanoscale. Metal nano-structures are variously shaped objects (e. g. spheres, rods, gratings, etc.) with size as small as few tens of nm, typically made of noble metals, such as gold and silver.

Metal-dielectric interfaces can support evanescent waves (see Chapter 2), propagating along the surface [22, 25, 26]. Consequently, metal nano-structures with one dimension much larger than the incident wavelength λ, such as nano-wires, can be coupled with these evanescent fields for waveguiding applications. These wave modes, called Surface Plasmon Polariton (SPP), are characterized by an electric field strongly localized within a short distance from the surface, much smaller than the wavelength. The electromagnetic properties of metal nanostructures are strongly affected by plasmonic resonances, i. e. collective oscillation of conduction electrons, occurring in the visible spectrum. In metal nano-particles with all dimensions comparable or smaller than λ, the electron resonances couple with the the structure shape and the surface properties, as rigorously described in Chapter 3. In this case, the collective resonances of conduction electrons in metal nano-structured are called Localized Surface Plasmons (LSPs).

LSPs and SPPs have gathered enormous attention from the scientific community, due to the large variety of optical properties that they confer to the metal nanostructures sustaining them. These processes will be described more in detail in Chapter 3. In particular, plasmonic metamaterials are used to realize super-lenses operating in the optical spectrum. Several configuration of plasmonic nano-lenses have been proposed, which are able to focus an incident electromagnetic radiation far below the diffraction limit, in engineered spectral bands. Moreover the electric field magnitude in proximity of a metal nano-structure is higher than that of the incident radiation. The electromagnetic interaction of closed-spaced metal nano-structures leads to extremely high values for the electric field magnitude in the gap between them. This region is referred to as *hot spot*.

This effect, generally known as *field enhancement*, is able to boost physical, and in particular optical, phenomena such as absorption and scattering [27], Raman scattering [28], harmonic generation [29], etc. . In Part II we propose, as part of the present Thesis, novel configurations for plasmonic nanolenses with high field enhancement, while in Part III we study its effects on the second-harmonic generation from metal nanoparticles.

1.2 NEGATIVE PERMEABILITY AND REFRACTIVE INDEX

1.2.1 *Negative magnetic permeability*

In order to hold a full control over the design of metamaterials, it would be desirable to have a magnetic analogue of good electric conductors like metals. The magnetic behavior of this ideal substance would be similar to a magnetic plasma, with a magnetic permeability $\mu(\omega) = 1 - \omega_{mp}^2/\omega^2$, with ω_{mp} being the magnetic plasma frequency. Moreover, this ideal substance should be easy to introduce in the fabrication techniques of nanotechnology.

Unfortunately, it is not possible to find in nature a good magnetic conductor with these ideal properties, but in 1999 Pendry *et al.*[30] predicted that a splitted cylindrical structure made of an electrical conductor media could exhibit the following magnetic permeability:

$$\mu = 1 - \frac{f\omega^2}{\omega^2 - \omega_0^2 + i\Gamma\omega}\,, \tag{1.1}$$

where f is a geometrical parameter, Γ is related to the losses, and ω_0 is the resonance frequency. In 2000, it was demonstrated that the Split Ring Resonator (SRR) could be the basic element for these *magnetic metamaterials*, in the microwave regime [31]. In particular a SRR, displayed in Fig. 1.2(a), consists of a ring, or loop, of a conductive non-magnetic material, with an open end. A very common configuration is represented in 1.2(b), with two embraced loops.

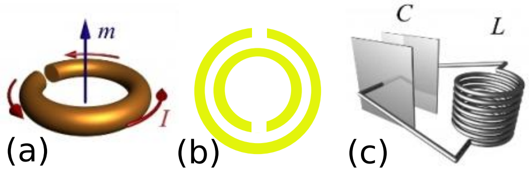

Figure 1.2: Split Ring Resonator with one (a) and two loops (b). Equivalent LC-circuit (c).

The SRR can be described as a small LC-oscillator circuit shown in Fig. 1.2(c), where the ring split is responsible for the capacitance C, while the wire is a fraction of a magnetic coil with inductance L.

In a SRR cell, the external electromagnetic field induces rotating currents in the loops, which in turn produce their own magnetic flux. Since the dimensions of the structure are small compared to the resonant wavelength, the response is well described by a magnetic dipole oriented perpendicular to the plane of the SRR. Depending on the SRR resonance properties, the induced magnetic dipole can enhance or oppose the external field.

It has been shown that this configuration results in materials with negative permeability, having place in quadrant (IV) of Fig. 1.1 [30].

1.2.2 *Negative refractive index*

For the substances in quadrant (III) of Fig. 1.1, Maxwell's equations imply that the wavevector $\hat{\boldsymbol{k}}$ and the Poynting vector $\boldsymbol{S}$ for a propagating plane-wave are anti-parallel. This uncommon effect is equivalent to the fact that the flow of energy and the phase velocity are directed one opposite to the other.

It can be easily shown that, in order to take into account for this in the definition of the refractive index $n^2 = \varepsilon\mu$, where ε and μ are the relative permittivity and permeability, it is necessary to select the negative root of n. For this reason, the substances falling in the case (III) are called Negative Index Materials (NIMs) [32, 4].

In NIMs the wavevector $\hat{\boldsymbol{k}}$, the electric field $\boldsymbol{E}$ and the magnetic field $\boldsymbol{M}$ form a left-handed set, instead of a right-handed one, occurring in natural materials, as shown in Fig. 1.3(b). For this reason, NIMs are also known as Left Handed Materials (LHMs), in opposition to RHMs, e. g. the natural ones.

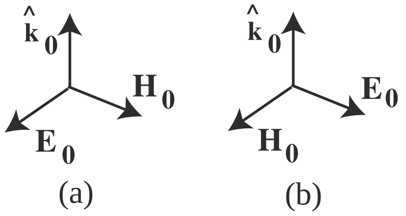

Figure 1.3: The Electric Field, Magnetic Field and Wavevector in Right Handed Materials (a) and Left Handed Materials (b).

Since NIMs have $n < 0$, the phase velocity is directed against the flow of light, resulting in anomalous optical properties. For example, unconventional reflection and refraction at an interface with a NIM occur. In particular, a ray incident on an LHM from an RHM refracts to the same side as the incident beam, with respect to the interface normal, as shown in Fig. 1.4.

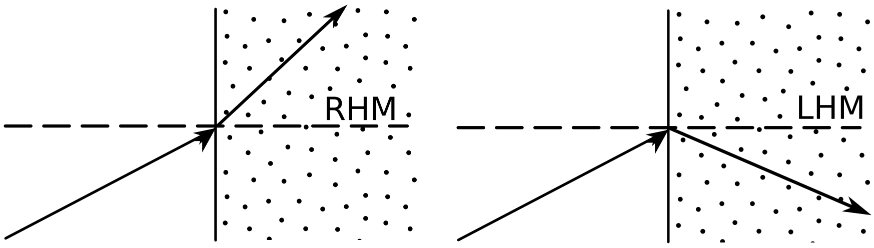

Figure 1.4: Refraction of a ray from Right Handed Materials (a) and from Left Handed Materials (b).

NIMs allow for the realization of super-lenses. As a matter of fact, the diffraction limit always affects the resolution of a classical lens, through Abbe's law $d = \lambda/2 \cdot NA^{-1}$, where λ is the ray wavelength, NA is the lens Numerical Aperture, and d is the size of the best focused spot. On the contrary, a super-lens has the power to focus far below the diffraction limit, due to the combined effects of propagating and evanescent modes.

The simplest configuration for a super-lens is a slab of a NIM. It is predicted that the rays from a point source in a RHM would be focused to a point on the opposite side of a LHM slab. In particular, if the LHM has a suitable refractive index, then it can produce a focus with subwavelength resolution.

Super-lenses can be realized in the microwave band with standard lithography, or in the visible spectrum with nanotechnology, allowing the resolution of objects only a few nanometers across [33].

In the microwave regime, the elementary artificial 'molecule' for NIMs is the SRR coupled with a conductive wire. In fact, it has been shown that a wire element behaves as a plasma in the microwave frequency range. The combination of the two elements provide the basic element for a NIM, as demonstrated in Ref. [31].

1.3 APPLICATIONS

1.3.1 *Optical integration at nanoscale*

The telecommunication industry requires ultra-compact photonic integrated circuits in order to fulfill its strict roadmap. The photonic devices are called to meet the requirements of their electronic counterparts, and in particular the possibility to create, guide, modulate, and detect deep-subwavelength optical fields.

Metamaterials have an enormous potential in integrated optics for improving the performance of a variety of devices, such as modulators, switches and sensors. An integrated circuit contains, on a single compact substrate, a variety of functional components (filters, couplers, modulators) that are connected with integrated waveguides.

Plasmonic metamaterials emerged in this context for the opportunity to combine operational speeds and ultra-compact architectures, rivaling electronics in both speed and critical feature sizes.

1.3.2 *Enhanced Nonlinear optical properties*

Metamaterials can provide optical nonlinearities far more intense then those of natural substances. This property is accomplished mainly because of two effects, the local electric field enhancement and the magnetic dipole resonance, respectively.

In particular, plasmonic metamaterials are able to strongly boost the Raman scattering (see Appendix A.7), due to the local electric field enhancement. For instance, the adsorption of a molecule onto a metal surface has been shown to enhance the Raman signal up to 14 orders of magnitude [34]. In this process, called Surface Enhanced Raman Scattering (SERS), the local field E_{loc} in proximity of the metal surface is larger than the incident field E_{inc}, by the factor Near Field Enhancement (NFE): $E_{loc} = \mathrm{NFE} \cdot E_{inc}$. Efficient SERS signals are obtained if strong NFE is excited at both the incident and Raman-scattered wavelengths. The quality of a metamaterial as substrate for SERS can be evaluated as the ratio of the SERS signal divided by the Raman signal of the bulk molecule.

Magnetic metamaterials have been shown to provide enhanced nonlinear effects such as harmonic generation. In this case, the material is engineered to provide a strong magnetic response due to magnetic dipole resonance. For instance, in a SRR the unusual magnetic dipolar mechanism becomes relevant as a result of the enhancement and the orientation of the local magnetic fields associated with the magnetic-dipole resonances of the SRR. Eventually, metamaterials can be used to fabricate nonlinear-optical mirrors, in which a nonlinear negative-index medium emits the generated frequency towards the source of the pump [35].

1.3.3 *Imaging and lithography*

In optics, the unique properties of surface plasmons can control the light transmission through sub-wavelength apertures. The size of certain SPP configurations can be smaller than the operation wavelength, thus offering a path to decrease the size of optical components beyond the diffraction limit.

1.3.4 *Biology and Medicine*

In chemistry and biology, plasmonic metamaterials are already used for their sensitivity to the embedding environment. Chemical and biochemical sensors based on surface plasmons are used to monitor, for example, molecular binding events. Moreover, it has been proposed a cancer treatment based on plasmonic effects to destroy tumors. It is possible to inject into the bloodstream nanoparticles, with the propriety to embed themselves in a tumor. If laser light is pointed at the interested area, it would induce electron resonances. The heating would kill tumor cells without damaging the surrounding healthy tissue.

1.3.5 *Solar cells*

Plasmonic nanostructures have been demonstrated to increase the efficiency of solar cells. In particular, two main basic mechanisms have been proposed to explain the photocurrent enhancement. The first is the light scattering of metal nanoparticles incorporated in the cells. The second is the local electric field enhancement, In general, plasmonic nanostructured films can be used to confine and guide incident sunlight into the absorbing layer of solar cells. The contribution of each mechanism depends mostly on the particle size, how strongly the semiconductor absorbs and the electrical design of the solar cell.

1.3.6 *Cloaking*

Metamaterials have been theorized to produce invisibility cloak. For instance, a cloaking device would be a thick shell constructed of metamaterials, bending the electromagnetic radiation around its central cavity, in which an object can be hidden. Metamaterials direct and control the propagation and transmission of specified parts of the light spectrum and demonstrate the potential to render an object seemingly invisible. Metamaterial cloaking, based on transformation optics, describes the process of shielding something from view by controlling electromagnetic radiation. Objects in the defined location are still present, but incident waves are guided around them without being affected by the object.

2

ELECTROMAGNETIC RESPONSE OF METALS

The electromagnetic force is one of the four fundamental interactions in nature. The e.m. field in vacuum is completely specified in classical electrodynamics by the electric field $\boldsymbol{e} = \boldsymbol{e}(\boldsymbol{r}, t)$ $[\mathrm{V m^{-1}}]$ and magnetic induction $\boldsymbol{b} = \boldsymbol{b}(\boldsymbol{r}, t)$ $[\mathrm{T}]$, defined by the Lorentz's law and satisfying the Maxwell's equations in empty space [22, 26]. The electromagnetic field can propagate at a constant velocity called *light speed* c $[\mathrm{m s^{-1}}]$, whose value is a universal constant. For this reason, it is common the term *electromagnetic wave*.

The Fourier analysis of a physically real e.m. field reveals that it is composed by an infinity of spectral components, with diverse intensity. Each component is characterized by the angular frequency ω $[\mathrm{rad\,s^{-1}}]$ at which $\boldsymbol{e}$ and $\boldsymbol{b}$ oscillate in time. The wavelength, defined as $\lambda = 2\pi c/\omega$ $[\mathrm{m}]$, is the spatial period of the propagating wave.

An e.m. field composed by one single spectral component is called *monochromatic wave*. An e.m. field composed by all the spectral components in a range with the same intensity is called *white light* (in that range).

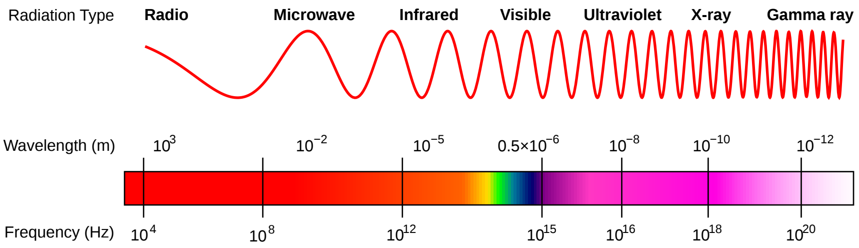

Figure 2.1: Electromagnetic spectrum from the radio-waves to the Gamma rays. The frequency and the wavelength are specified for each regime.

The electromagnetic spectrum is represented in Fig. 2.1. The spectrum of interest of the present Thesis ranges from the near Infrared to the near UV light, where metal nanostructures show a rich set of electromagnetic phenomena, as already introduced in Chapter 1.

2.1 ELECTROMAGNETISM IN THE MATTER

In the present Chapter, we will consider the electromagnetic response of metals to an e.m. field . Let us start considering the linear response in the frequency domain of a general material to an electric field $\boldsymbol{E} = \boldsymbol{E}(\boldsymbol{r}, \omega)$ and magnetic induction $\boldsymbol{B} = \boldsymbol{B}(\boldsymbol{r}, \omega)$. Then, the polarization $\boldsymbol{P} = \boldsymbol{P}(\boldsymbol{r}, \omega)$ $[\mathrm{Cm}^{-2}]$ (electric dipole per unit volume) and magnetization $\boldsymbol{M} = \boldsymbol{M}(\boldsymbol{r}, \omega)$ $[\mathrm{Am}^{-1}]$ (magnetic dipole per unit volume) are induced [22, 26, 25]. Let us define the electric induction $\boldsymbol{D} = \boldsymbol{D}(\boldsymbol{r}, \omega)$ $[\mathrm{Cm}^{-2}]$ and the magnetic field $\boldsymbol{H} = \boldsymbol{H}(\boldsymbol{r}, \omega)$ $[\mathrm{Am}^{-1}]$ as:

$$\boldsymbol{D} = \epsilon_0 \boldsymbol{E} + \boldsymbol{P} \tag{2.1}$$

$$\boldsymbol{H} = \boldsymbol{B}/\mu_0 - \boldsymbol{M} \ , \tag{2.2}$$

where ϵ_0 $[\mathrm{Fm}^{-1}]$ and μ_0 $[\mathrm{Hm}^{-1}]$ are the universal constant called permittivity and permeability of empty space, respectively. For linear achiral space-non-dispersive media:

$$\boldsymbol{P} = \boldsymbol{P}(\boldsymbol{E}) = \epsilon_0 \chi_e \boldsymbol{E} \tag{2.3}$$

$$\boldsymbol{M} = \boldsymbol{M}(\boldsymbol{H}) = \chi_m \boldsymbol{H} \ , \tag{2.4}$$

where $\chi_e = \chi_e(\omega)$ and $\chi_b = \chi_b(\omega)$ are the electric and magnetic susceptibilities. They are tensors of rank 2 and reduce to scalars for isotropic materials.

The hypothesis of non-dispersivity in space implies that $\boldsymbol{P}(\boldsymbol{r})$and $\boldsymbol{M}(\boldsymbol{r})$ depend on the values of $\boldsymbol{E}$ and $\boldsymbol{H}$ only at the point in space $\boldsymbol{r}$. This assumption is also called *local* approximation.

Consequently, we can define the following *constitutive relations*:

$$\boldsymbol{D} = \epsilon_0 \boldsymbol{E} + \boldsymbol{P} = \epsilon_0 \epsilon \boldsymbol{E} \tag{2.5}$$

$$\boldsymbol{B} = \mu_0 \boldsymbol{H} + \mu_0 \boldsymbol{M} = \mu_0 \mu \boldsymbol{H} \ , \tag{2.6}$$

where $\epsilon = \epsilon(\omega)$ and $\mu = \mu(\omega)$ are the relative permittivity and permeability of the medium, defined as $\epsilon = I + \chi_e$ and $\mu = I + \chi_m$, describing the polarization and the magnetization response (I is the identity tensor).

With this assumptions, the differential form of *Maxwell's equations* in the frequency domain is:

$$\begin{cases} \nabla \times \boldsymbol{E} & = -i\omega \boldsymbol{B} \\ \nabla \times \boldsymbol{H} & = i\omega \boldsymbol{D} + \boldsymbol{J} \\ \nabla \cdot \boldsymbol{D} & = \rho \\ \nabla \cdot \boldsymbol{B} & = 0 \end{cases} , \tag{2.7}$$

where, $\boldsymbol{J}$ $[\mathrm{Am}^{-2}]$ is the possible source current density and ρ $[\mathrm{C}^{-3}]$ is the possible source charge density. They are related by the *continuity equation*:

$$\nabla \cdot \boldsymbol{J} + i\omega\rho = 0. \tag{2.8}$$

For the subject of interest of the present thesis, we deal with material with negligible magnetization response $\boldsymbol{M} \approx 0$, resulting in $\mu = 1$ and $\boldsymbol{B} = \mu_0 \boldsymbol{H}$. Therefore, we can write $\chi_e = \chi$ for the clearness of notation.

2.1.1 *Electromagnetic nonlinearities*

The previous analysis is valid to describe the linear material response to an e.m. field in the local approximation. In real circumstances, the time-dependent polarization $\boldsymbol{p}(\boldsymbol{r}, t)$ can display significant nonlinearities if the amplitude of $\boldsymbol{e}(\boldsymbol{r}, t)$ is high, for instance in materials excited by laser beams. In these cases, the time-domain constitutive relation $\boldsymbol{p} = \boldsymbol{p}(\boldsymbol{e})$ is a nonlinear functional, and it is possible to expand it in Volterra's series [36]. In the simplifying hypothesis that the material response is instantaneous, i. e. non-dispersive in time, we can write:

$$\boldsymbol{p} = \epsilon_0(\chi^{(1)}\boldsymbol{e} + \chi^{(2)} : \boldsymbol{ee} + \chi^{(3)} : \boldsymbol{eee} + \cdots + \chi^{(l)} : \boldsymbol{e}...\boldsymbol{e}) \,, \tag{2.9}$$

where $\chi^{(l)}$ is a tensor of rank $l+1$, called l-th order susceptibility. For the cases of interest of the present thesis, we will only discuss electromagnetic nonlinearities when the electric field $\boldsymbol{e} = \boldsymbol{e}(\boldsymbol{r}, t)$ is monochromatic at frequency ω. Let us consider an electric field $\boldsymbol{e}(\boldsymbol{r}, t) = \boldsymbol{E}^{(\omega)}(\boldsymbol{r})e^{i\omega t}$ (a real-valued field can be obtained as $\mathrm{Re}\{\boldsymbol{e}(t)\}$), then we can write from Eq. 2.9:

$$\begin{aligned} \boldsymbol{p} = \epsilon_0(&\chi^{(1)}\boldsymbol{E}^{(\omega)}e^{i\omega t} \\ &+\chi^{(2)} : \boldsymbol{E}^{(\omega)}\boldsymbol{E}^{(\omega)}e^{i2\omega t} \\ &+\chi^{(3)} : \boldsymbol{E}^{(\omega)}\boldsymbol{E}^{(\omega)}\boldsymbol{E}^{(\omega)}e^{i3\omega t} + \ldots \\ &+\chi^{(l)} : \boldsymbol{E}^{(\omega)}...\boldsymbol{E}^{(\omega)}e^{il\omega t}) \end{aligned} \,, \tag{2.10}$$

It is easy to see that each term $\chi^{(l)}$ contributes to specific harmonic components of $\boldsymbol{p}$. In particular, the term $\chi^{(1)}$ is responsible for the linear response of the material. In general, the term $\chi^{(l)}$ is responsible for the response of the media at the l-th harmonic $l\omega$. These processes are indeed referred to *harmonic generation*.

It is important to remark that harmonic generation is not the only nonlinear process occurring in materials. First of all, by considering a real-valued electric field, it is possible to demonstrate that the term $\chi^{(2)}$ determines a static ($\omega = 0$) contribution to the polarization. This process is called *optical rectification*. Similarly, the term $\chi^{(3)}$ determines a contribution to the polarization at the frequency ω. This process is called *intensity-dependent refractive index*, because it modulates the medium refractive index by the intensity of the electric field $\boldsymbol{e}(\boldsymbol{r}, t)$.

Other nonlinear processes can occur in materials when the e.m. field is not monochromatic, such as the *wave-mixing*. Eventually, the electromagnetic nonlinearities can involve other physical processes, such as a vibrational mode of a molecule in the Raman scattering.

2.2 CONDUCTION AND BOUND ELECTRONS

The electromagnetic response of solid conductors is generally governed by the electrons from the UV to the Infrared spectrum. If we consider an isolated atom, the *valence electrons* are those in the outermost atomic shell, involved in the interactions with other atoms. The valence electrons in solids satisfy the Shroedinger's equation with potential energy $U(\boldsymbol{r})$ given by the interaction with the ions.

In crystals, such as ideal metals, insulator and semiconductors, the regular arrangement of the lattice ions makes $U(\boldsymbol{r})$ periodic. The Shroedinger's equation with a periodic potential energy implies that not all the electron states, characterized by energy E and momentum $\boldsymbol{k}$, are allowed. In particular, the allowed states are arranged into bands of energy separated by *energy gaps* [23, 24].

In metals, such as alkali (Li, Na) or noble metals (Cu, Ag, Au), the highest energy band partially occupied by electrons is called *conduction band*. These conduction electrons are easily moved by an external e.m. field , because in their energy band there is a high number of available states with close values of E and $\boldsymbol{k}$. For this reason, conduction electrons are often referred to as *free*.

The electrons in fully occupied energy bands are barely moved to other states. For this reason, these are often referred to as *bound* electrons. A bound electron can be excited from his ground state with energy E_m to an available state with energy $E_n > E_m$ through the interaction with a photon with energy $E_n - E_m$. Similarly, the relaxation from the level E_n to the energy level E_m occurs with the emission of a photon with the same energy $E_n - E_m$. These processes are called *interband transitions*.

This Chapter describes the conduction and the bound electron contributions to the electromagnetic response of media within a classical approach.

2.2.1 *Drude-Sommerfeld model*

Conduction electrons can be treated as a plasma of non-interacting particles freely moving in the ion lattice, as done by Drude and Sommerfeld. The case of a plasma with interactions will be rigorously discussed later in the Chapter, with a hydrodynamic approach.

Let us consider the motion of an electron with coordinate $\boldsymbol{r} = \boldsymbol{r}(t)$, characterized by the average collision frequency ν with the ion lattice. The second Newton's law gives:

$$\frac{d^2\boldsymbol{r}}{dt^2} + \nu\frac{d\boldsymbol{r}}{dt} = -\frac{e}{m}\boldsymbol{e}\,. \tag{2.11}$$

If we consider an elementary domain where n_0 is the number of free electrons per unit volume, then its net polarization is $\boldsymbol{p} = (-e)n_0\boldsymbol{r}$. In the frequency domain this leads to the following relation:

$$\boldsymbol{P} = -\frac{\omega_p^2}{\omega^2 - i\nu\omega}\epsilon_0\boldsymbol{E}\,, \tag{2.12}$$

with $\omega_p = \sqrt{n_0 e^2/m\epsilon_0}$. Therefore the free electrons permittivity is:

$$\epsilon(\omega) = 1 - \frac{{\omega_p}^2}{\omega^2 - i\nu\omega}\,. \tag{2.13}$$

The real end imaginary parts of the permittivity of gold, according to the Drude-Sommerfeld model, are plotted in Fig. 2.2(a), with interpolated values of ω_p and ν [37].

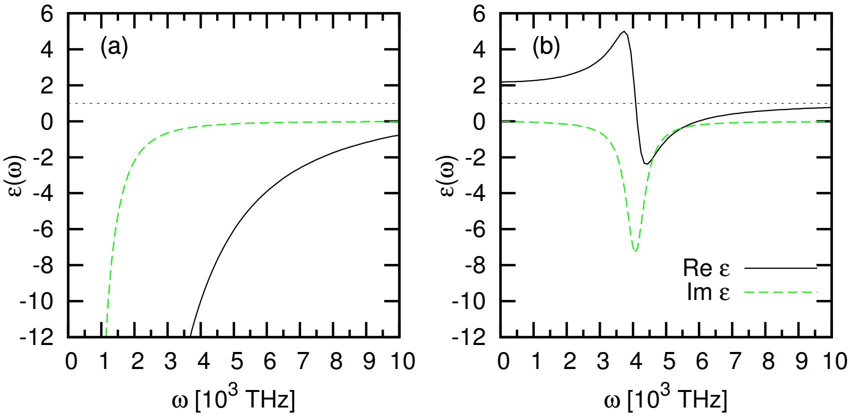

Figure 2.2: Real and imaginary parts of the permittivity $\epsilon(\omega)$ of gold, according to the Drude-Sommerfeld (a) and the Lorentz (b) models.

According to this model, at large frequencies the gold is transparent to the radiation. For low frequencies the real part of the permittivity becomes negative and losses significantly increase.

In the case where the damping effect due to the lattice is neglected, i. e. the average collision frequency is sufficiently low, then we can write $\epsilon(\omega) = 1 - \omega_p^2/\omega^2$, corresponding to a pure Drude model.

2.2.2 *Lorentz's model*

Bound electrons can be classically treated as damped harmonic oscillators around the ions, as done by Lorentz. Let us call $\boldsymbol{x} = \boldsymbol{x}(t)$ the electron displacement from the oscillator center, induced by an external electric field $\boldsymbol{e} = \boldsymbol{e}(t)$. Then, Newton's second law gives:

$$\frac{d^2\boldsymbol{x}}{dt^2} + \nu\frac{d\boldsymbol{x}}{dt} + \omega_0^2\boldsymbol{x} = -\frac{e}{m}\boldsymbol{e}\,, \tag{2.14}$$

where ν is a characteristic damping frequency, and ω_0 is an angular frequency related to the oscillator restoring force. If $\boldsymbol{e}$ is time-harmonic at angular frequency ω and n_L is the number density of oscillating electrons, then the bound electron contribution to the polarization in the frequency-domain is:

$$\boldsymbol{P} = n_L(-e)\boldsymbol{X} = \frac{\omega_L^2}{\omega_0^2 - \omega^2 + i\nu\omega}\epsilon_0\boldsymbol{E}\,, \tag{2.15}$$

with $\omega_L = \sqrt{n_L e^2/m\epsilon_0}$. Hence, the bound electron susceptibility is:

$$\chi(\omega) = \frac{{\omega_L}^2}{\omega_0^2 - \omega^2 + i\nu\omega} \tag{2.16}$$

Figure 2.2(b) plots the real and imaginary parts of the permittivity $\epsilon(\omega)$ of gold, with interpolated values of ω_L, ω_0 and ν [37]. It is shown that the range in which the real part can assume negative values is limited to $\omega_0 < \omega < \omega_L$. Moreover, it doesn't assume as large negative values as the case of free electrons.

The bound electron permittivity would diverge for $\omega = \omega_0$ if the damping were absent, i. e. if $\nu = 0$. Consequently, ω_0 can be seen as the angular frequency associated to the transition to an electron state with higher energy.

From this point of view, Eq. 2.15 is unable to fully account for the response of bound electrons, that can undergo several transition between energy levels. Consequently it is necessary to introduce one contribution of kind 2.15 for each allowed transition:

$$\chi(\omega) = \sum_i \frac{{\omega_{Li}}^2}{\omega_{0i}^2 - \omega^2 + i\nu_i\omega} \tag{2.17}$$

where the summation is over the i electron states.

2.2.3 *The Drude-Sommerfeld-Lorentz model*

The permittivity of media, including the effects of both bound and conduction electrons, can be expressed by summing the effects of both contributions. As already noticed, one Lorentzian term is unable to describe the correct behavior of bound electrons, and it is necessary to consider several contributions with the Lorentzian form, one for each transition.

Consequently, under the Lorentz's model for bound electrons and the Drude-Sommerfeld model for conducting electrons, we can write the permittivity ϵ of metals as:

$$\epsilon(\omega) = 1 - \frac{{\omega_p}^2}{\omega^2 + i\nu\omega} + \sum_i \frac{{\omega_{Li}}^2}{\omega_{0i}^2 - \omega^2 + i\nu_i\omega} \,. \tag{2.18}$$

A comparison between the Drude-Sommerfeld-Lorentz model [37] and experimental measurements by Johnson and Christy [38] for Gold is shown in Fig. 2.3.

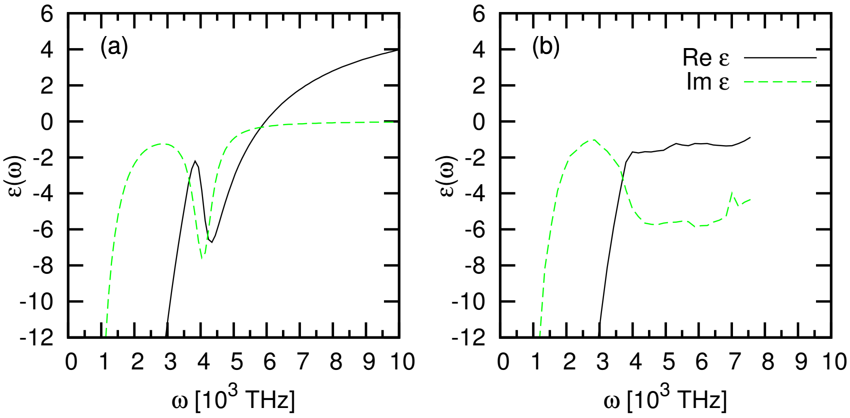

Figure 2.3: Gold permittivity calculated with the Drude-Sommerfeld-Lorentz model (a) and measured by Johnson and Christy (b)

The Drude-Sommerfeld-Lorentz model in unable to realistically predict the permittivity of media at high frequencies, approximately from the blue visible spectrum to the UV. This circumstance is due to the fact that the bound electron response to an e.m. field is not well accounted by a classical treatment. In particular, interband transition needs to be taken into account in a more realistic way than a classical oscillator.

It is necessary to extend the classical treatment by modeling the bound electrons as quantum oscillators, in order to fully account for the quantum mechanical effects of the energy levels discretization [39]. However, it is worth to stress that the free electron model is a good approximation for conductive media such as metals for low frequencies, i. e. from the red visible spectrum to the microwave.

2.3 METAL-DIELECTRIC INTERFACE

The interface between two different media can support evanescent waves propagating along the interface. They are longitudinal waves, i. e. the electric or the magnetic fields have non-zero components along the direction of propagation. Evanescent waves can be represented in the frequency-domain as $\boldsymbol{E}e^{-i\boldsymbol{k}\boldsymbol{r}}$, where at least one of $\boldsymbol{k}$ components is purely imaginary [40, 41]. For instance, let us consider the configuration represented in 2.4(a). In this case the z-component of $\boldsymbol{k}$ is purely imaginary, and the electric field $\boldsymbol{E}$ exponentially decays along the z-direction. The wave does not propagate in the z-direction, but along the interface, i. e. along the x-axis in the schematic.

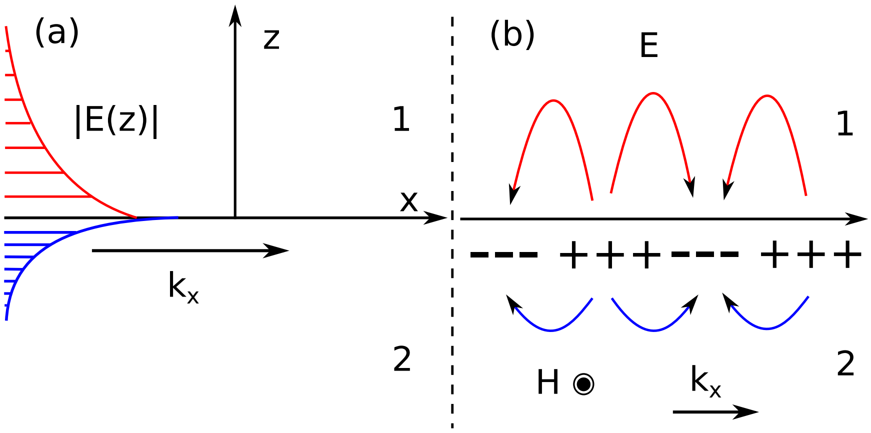

Figure 2.4: Evanescent wave at the interface between two different media (a). Surface Plasmon Polariton at a metal-dielectric interface (b).

Evanescent waves propagating along an interface can result from two main circumstances, with respect to Fig. 2.4(a):

1. Total internal reflection: the medium 1 has higher refractive index than medium 2, and a wave is impinging on the interface from medium 1 with a higher angle of incident than the critical angle [22, 25].
2. Negative refractive index: the medium 2 has a negative refractive index, and a wave incoming from medium 1 is coupled to the interface by means of specific geometries, such as Kretschmann's or Otto's configurations [40, 41].

The latter case describes the propagation of an evanescent wave along the interface between a metal and a dielectric, at frequencies below ω_p. This wave is called Surface Plasmon Polariton (SPP), and it is supported by the resonance of the conduction electrons at the metal-dielectric interface, as illustrated in Fig. 2.4(b). SPPs are are Transverse Magnetic waves, and they are strictly related to the possibility to confine the electromagnetic radiation in subwavelength dimensions.

Let us consider the geometry of Fig. 2.4. The electric field $\boldsymbol{E}_i$ in both media $i = 1, 2$ must satisfy Helmholtz's equation:

$$\nabla^2 \boldsymbol{E}_i + k_0^2 \varepsilon_i \boldsymbol{E}_i = 0 \tag{2.19}$$

where ε_i is the permittivity of the medium i and k_0 is the wavevector in empty space. A similar equation must be satisfied by the magnetic field H_i. If we assume a solution of the kind $\boldsymbol{E}_i(x, y, z) = \boldsymbol{E}_i(z) e^{-ik_x x}$ with no spatial variations along y, then Eq. 2.19 becomes:

$$\frac{\partial^2 \boldsymbol{E}_i}{\partial z^2} + (k_0^2 \varepsilon_i - k_x^2) \boldsymbol{E}_i = 0 \tag{2.20}$$

This problem presents two sets of self-consistent solutions, namely the Transverse Magnetic modes and the Transverse Electric modes. It can be shown that, in the case of SPP resonances, no Transverse Electric modes can exist [40]. For Transverse Magnetic modes, the solution of Eq. 2.20 can be written as:

$$\begin{aligned} H_y &= && A e^{-ik_x x} e^{-k_z z} \\ E_x &= \frac{-k_z i}{\omega \varepsilon_0 \varepsilon_1} && A e^{-ik_x x} e^{-k_z z} \\ E_z &= \frac{-k_x}{\omega \varepsilon_0 \varepsilon_1} && A e^{-ik_x x} e^{-k_z z} \end{aligned} \tag{2.21}$$

for $z > 0$ and

$$\begin{aligned} H_y &= && A e^{-ik_x x} e^{k_z z} \\ E_x &= \frac{k_z i}{\omega \varepsilon_0 \varepsilon_1} && A e^{-ik_x x} e^{k_z z} \\ E_z &= \frac{-k_x}{\omega \varepsilon_0 \varepsilon_1} && A e^{-ik_x x} e^{k_z z} \end{aligned} \tag{2.22}$$

for $z < 0$, where A is the magnetic field amplitude and k_z is a measure of the field confinement near the interface. The following condition is also verified:

$$k_x^2 = \frac{\varepsilon_1 \varepsilon_2}{\varepsilon_1 + \varepsilon_2} k_0^2 \tag{2.23}$$

From the dispersion relation in Eq. 2.23 it is possible to demonstrate that SPPs can be induced along metal-dielectric interfaces by means of spacial phase-matching techniques with an external excitation. For a more detailed description of the SPPs and the coupling configurations we refer to Ref. [40].

2.4 ELECTRON FLUID

The Drude-Sommerfeld model is able to predict important features about the electromagnetic response of conduction electrons in metals. However, this model is physically unreasonable at the boundary of a metal domain with an embedding medium, as pointed out by Rudnick and Stern [42].

The electrons in the conduction band are more accurately described by a hydrodynamic approach [43, 44], in which they are modeled as a fluid of interacting charged particles. Let us assume a jellium model for the background positive ion lattice, making the effective mass of the electrons m_{eff} slightly different from the nonrelativistic mass in empty space.

Let us define an elementary volume $\Delta\Omega$ of an electron fluid, comprising ΔN electrons. Consequently, the electron number density is a function of space $\boldsymbol{r}$ and time t: $n(\boldsymbol{r}, t) = \Delta N / \Delta\Omega$ Let us consider the eulerian velocity field $\boldsymbol{v}(\boldsymbol{r}, t) = \sum_{h=1} \boldsymbol{v}_h(t)/\Delta N$, where the summation is over the electrons contained in $\Delta\Omega$ at position $\boldsymbol{r}$. Therefore, we can write Euler's equation as:

$$\frac{\partial}{\partial t}(n m_{eff} \boldsymbol{v}) = -\nabla \cdot (n m_{eff} \boldsymbol{v}\boldsymbol{v}) + n\boldsymbol{f} \ , \tag{2.24}$$

where $\boldsymbol{f}$ is the force field per unit volume, composed by three contributions: $\boldsymbol{f} = \boldsymbol{f_{em}} + \boldsymbol{f_d} + \boldsymbol{f_q}$. In particular:

1. $\boldsymbol{f}_{em} = -e(\boldsymbol{e} + \boldsymbol{v} \times \boldsymbol{b})$ is the Lorentz's force, where $\boldsymbol{e} = \boldsymbol{e}(\boldsymbol{r}, t)$ and $\boldsymbol{b} = \boldsymbol{b}(\boldsymbol{r}, t)$ are the external electric field and magnetic induction, respectively.

2. $\boldsymbol{f}_d = -m_{eff} \nu \boldsymbol{v}$ is a frictional force, where ν is the average collision frequency of conduction electrons with the metal lattice ions.

3. $\boldsymbol{f}_q = -\nabla\mu$ is a short-range force of quantum origin, described by the chemical potential μ. For analogy with a classical fluid, this term is often referred to as *quantum pressure*. It comprises two contributions, one from the Thomas-Fermi theory, and one introduced by Dirac [45].

Equation 2.24 has to be solved along with the charge continuity equation and Maxwell's equations in empty space to calculate the dynamic of the electron fluid system [22, 25, 26].

2.4.1 *Steady-state solution*

First, let us consider the case of an electron fluid at equilibrium (i. e. $\boldsymbol{v} = 0$), immersed in a homogeneous medium Ω_e, as illustrated in Fig. 2.5. The electrons are kept inside Ω_i by the ion lattice, in the case of a metal domain. In these circumstances, $\boldsymbol{f} = 0$ is zero and $\boldsymbol{e} = \boldsymbol{e}_0$ is a static field, hence $\boldsymbol{e}_0 = -\nabla\phi$. The scalar potential is $\phi = 0$ in Ω_e because the net charge is null. In Ω_i, $\boldsymbol{f} = 0$ implies $-e\boldsymbol{e}_0 - \nabla\mu = 0$, therefore $\phi = \mu/e \neq 0$.

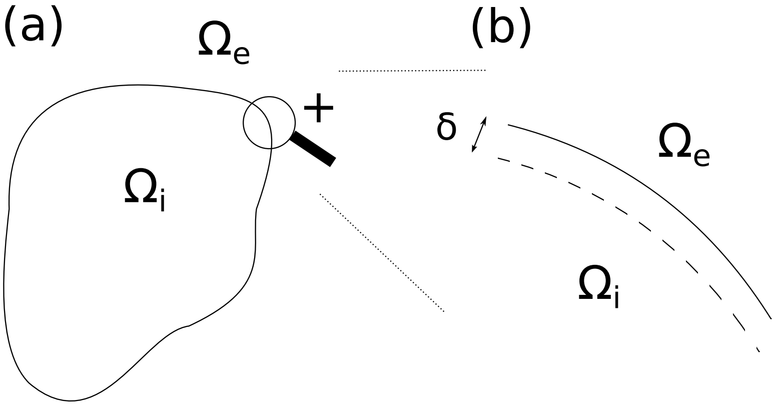

Figure 2.5: Metal domain immersed in an embedding medium (a) and selvedge-bulk regions near the metal domain boundary (b).

The discontinuity of the electric potential across the boundary Σ with the embedding medium implies the presence of a charge double layer at Σ. This double layer, extending over an infinitesimal length δ, is generated by the metal ion lattice (discontinuous at Σ), and by the number density of conduction electrons.

In the hypothesis that δ is not negligible with respect to the Fermi wavelength λ_F, he charge double layer partially extends in Ω_i. Therefore, Ω_i is divided into a domain, called *bulk*, where the net charge is zero, and a domain near the boundary, with a variable charge density. This domain in proximity of Σ, where the net charge is not zero, is called *selvedge region*.

Ultimately, the bulk is the domain where quantum interactions between the electrons are negligible. The selvedge is the domain, near the boundary, where quantum effects are significant.

The electromagnetic properties of the selvedge region are different from the bulk region. Consequently, the electromagnetic response of the electron fluid is strongly modified in proximity of the boundary with an external medium, as we shall see in the next.

2.4.2 *First- and second- order response*

In order to determine the system response to an external time-harmonic e.m. field at angular frequency ω, it is convenient to expand the involved scalar and vector fields as:

$$a(t) = a_0 + \sum_{i=1}^{\infty} a_i(t) \ , \tag{2.25}$$

where the 0-th term is the steady state solution and the generic i-th term is the harmonic contribution at frequency $i\omega$. Therefore,given an external field $\boldsymbol{e} = \boldsymbol{e}_1$, we can determine the Eq. 2.24 for each harmonic $i\omega$.

Let us consider the unknown $\boldsymbol{p} = \boldsymbol{p}(t)$ defined by $\partial\boldsymbol{p}/\partial t = -en\boldsymbol{v}$, representing the electric polarization in the electron fluid. In particular, let us derive from Eq. 2.24 the expression for the fields at frequency ω, i.e. with subscript 1 of the decomposition 2.25:

$$\frac{\partial^2 \boldsymbol{p}_1}{\partial t^2} + \nu \frac{\partial \boldsymbol{p}_1}{\partial t} + \boldsymbol{L} \cdot \boldsymbol{p}_1 = \omega_p^2 \epsilon_0 \boldsymbol{e}_1 \ , \tag{2.26}$$

where $\omega_p = \sqrt{\frac{n_0 e^2}{\epsilon_0 m_{eff}}}$ and $\boldsymbol{L}$ is a functional depending on the quantum pressure μ, as defined in Ref. [43]. Similarly, we can derive from Eq. 2.24 the expression for the fields at frequency 2ω, i.e. with subscript 2 of the decomposition 2.25. Following Sipe *et al.*[43], we can write:

$$\frac{\partial^2 \boldsymbol{p}_2}{\partial t^2} + \nu \frac{\partial \boldsymbol{p}_2}{\partial t} + \boldsymbol{L} \cdot \boldsymbol{p}_2 = \boldsymbol{S}_p + \boldsymbol{S}_f \ , \tag{2.27}$$

where $\boldsymbol{S}_p = \boldsymbol{S}_p(\mu_1)$ is the contribution related to the quantum pressure at ω, and $\boldsymbol{S}_f = \boldsymbol{S}_f(\boldsymbol{e}_1, \boldsymbol{b}_1)$ is the contribution due to the electric and magnetic fields at ω [43, 44].

Equations 2.26 and 2.27 describe the electron fluid polarization respectively at the first and at the second order in ω. They are valid both in the metal bulk and in the selvedge region.

In particular, the electron interactions due to quantum effects are negligible in the metal bulk (i.e. if $\mu = 0$). Consequently, the term $\boldsymbol{L} \cdot \boldsymbol{p}_1$ is zero and the Eq. 2.26 leads to the Drude-Sommerfeld dispersion relation of Eq. 2.13. On the contrary, in the selvedge region the quantum pressure effects are significant. However, it has be shown that the selvedge effects can be neglected when calculating the solution at the first order in ω [43].

2.5 SECOND-ORDER EFFECTS IN METALS

2.5.1 *Non-local effects: bulk nonlinearity*

The interaction of a time-harmonic e.m. field $\boldsymbol{E}_1$ at frequency ω with a metal produces a second-order polarization field $\boldsymbol{P}_2 = \boldsymbol{P}_2(\boldsymbol{E}_1)$ due to nonlinear effects. It is possible to express this dependence in multipole expansion [46, 47]:

$$\boldsymbol{P}_2 = \varepsilon_0 \left[\overleftrightarrow{\chi}_{\mathrm{d}}^{(2\omega)} : \boldsymbol{E}_1 \boldsymbol{E}_1 + \overleftrightarrow{\chi}_{\mathrm{q}}^{(2\omega)} : \boldsymbol{E}_1 \left(\nabla \boldsymbol{E}_1 \right) + \dots \right] , \tag{2.28}$$

where $\overleftrightarrow{\chi}_{\mathrm{d}}^{(2\omega)}$ is a third-rank tensor describing the dipolar response to $\boldsymbol{E}_1$, $\overleftrightarrow{\chi}_{\mathrm{q}}^{(2\omega)}$ is a fourth-rank tensor describing the quadrupolar response, and so on.

Noble metals such as gold and silver are centrosymmetric media, and therefore the dipolar response is zero, i. e. $\overleftrightarrow{\chi}_{\mathrm{d}}^{(2\omega)} = 0$ due to inversion symmetry. Consequently, they cannot produce second-order nonlinear processes in the local approximation [39, 46]. In fact, they can actually produce second-order effects because of nonlocal effects [48]. As a matter of fact, the lowest-order nonlocal contribute is the quadrupolar one:

$$\boldsymbol{P}_2 = \varepsilon_0 \overleftrightarrow{\chi}_{\mathrm{q}}^{(2\omega)} : \boldsymbol{E}_1 \left(\nabla \boldsymbol{E}_1 \right) . \tag{2.29}$$

For isotropic media, relation 2.29 can be expressed as [49]:

$$\boldsymbol{P}_2 = \varepsilon_0 \left[\beta \boldsymbol{E}_1 \nabla \cdot \boldsymbol{E}_1 + \gamma \nabla \left(\boldsymbol{E}_1 \cdot \boldsymbol{E}_1 \right) + \delta' \left(\boldsymbol{E}_1 \cdot \nabla \right) \boldsymbol{E}_1 \right] , \tag{2.30}$$

where β, γ and δ' are phenomenological parameters depending on the material. The first contribution in the second member of Eq. 2.30 is zero for homogeneous media ($\nabla \cdot \boldsymbol{E}_1 = 0$).

In the framework of the fluid model of Ref. [43], the frequency-domain solution of Eq. 2.27 in the metal bulk (where the quantum pressure effects are negligible) is:

$$\boldsymbol{P}_2(2\omega) = \gamma \nabla (\boldsymbol{E}_1 \cdot \boldsymbol{E}_1) , \tag{2.31}$$

where

$$\gamma = \frac{1}{8} \frac{\omega_p^4}{\omega^4} \frac{\epsilon_0}{n_0 e} . , \tag{2.32}$$

in agreement with the expression provided by Rudnick and Stern [42]. In conclusion, it turns out that $\delta' = 0$. However, δ' can assume non-zero values if the collision frequency ν is not negligible.

2.5.2 *Broken symmetry: surface nonlinearity*

The second-order nonlinear response of a metal has also a significant contribution from the selvedge region, where the centrosymmetry of the lattice is broken [42]. It is possible to phenomenologically express the second-harmonic surface polarization as:

$$\boldsymbol{P}_{2s} = \varepsilon_0 \overleftrightarrow{\chi}_s^{(2\omega)} : \boldsymbol{E}_1\boldsymbol{E}_1 \text{ on } \Sigma\,, \tag{2.33}$$

where $\overleftrightarrow{\chi}_s^{(2\omega)}$ is the surface second-order susceptibility. In the hypothesis that the metal surface has an isotropic symmetry with a mirror plane perpendicular to it, then the surface susceptibility tensor $\overleftrightarrow{\chi}_s^{(2\omega)}$ has only three non-vanishing and independent elements:

$$\chi_{\perp\perp\perp},\, \chi_{\perp\parallel\parallel} \text{ and } \chi_{\parallel\perp\parallel} = \chi_{\parallel\parallel\perp}\,, \tag{2.34}$$

where $\perp$ and $\parallel$ refer to the orthogonal and tangential components to the surface (see Fig. 6.1). It is generally considered that the component $\chi_{\perp\parallel\parallel}$ can be neglected [42, 50, 51, 52], therefore:

$$P_{2s\parallel} \cong \epsilon_0 \chi_{\parallel\perp\parallel} E_{1\perp} E_{1\parallel} \tag{2.35}$$
$$P_{2s\perp} \cong \epsilon_0 \chi_{\perp\perp\perp} E_{1\perp} E_{1\perp}\,, \tag{2.36}$$

where the subscripts $\parallel$ and $\perp$ denote respectively the parallel and perpendicular components of the fields. The estimation of the surface second-order susceptibility was phenomenologically conducted in the 1971 by Rudnick and Stern [42], who expressed the elements of $\chi_{\perp\perp\perp}$ and $\chi_{\parallel\perp\parallel} = \chi_{\parallel\parallel\perp}$ as:

$$\chi_{\parallel\perp\parallel} = \frac{b}{2}\frac{\epsilon_0}{en}\frac{\omega_p^4}{\omega^4}$$
$$\chi_{\perp\perp\perp} = \frac{a}{4}\frac{\epsilon_0}{en}\frac{\omega_p^4}{\omega^4}\,,$$

where a and b are phenomenological coefficients that are usually referred to as *Rudnick-Stern parameters*.

In 1980, the same analysis was extended to the electron fluid model by Sipe *et al.*[43]. In particular, in the frame of the hydrodynamic model, we can decompose the linear electric field in the selvedge region as:

$$\boldsymbol{E}_1(z) = \boldsymbol{E}_{1b} + \boldsymbol{E}_{1s}(z)\,, \tag{2.37}$$

where $\boldsymbol{E}_{1b}$ is the sum of the incident field and the linear field due to the currents in the bulk, while $\boldsymbol{E}_{1s}$ is the field due to the currents in the selvedge, depending on the distance from the metal boundary z. We can write:

$$\boldsymbol{E}_{1s}(z) = \int_0^\delta \overleftrightarrow{G}(z-z')\cdot \boldsymbol{P}_1(z')dz'\,, \tag{2.38}$$

where $\overleftrightarrow{G}(z-z')$ is the tensor Green function of the Maxwell's equations in empty space [22, 25, 26]. As long as the incident wavelength λ is much larger than the Fermi wavelength λ_F, it is a good approximation to consider the lowest term in δ/λ in the expansion in series of the operators $\boldsymbol{L}, \boldsymbol{S}_f, \boldsymbol{S}_p$ and of $\overleftrightarrow{G}(z-z')$. Moreover, it is possible to consider only the dipole moment per unit area of the second-order nonlinear polarization $\boldsymbol{P}_{2s}$ in the selvedge.

As a result of the previous approximations, $\boldsymbol{P}_{2s}$ can be written as:

$$\begin{aligned} P_{2s\parallel} &= -\frac{1}{2}\frac{\epsilon_0}{en}\frac{\omega_p^4}{\omega^4}E_{1\parallel}E_{1\perp} \\ P_{2s\perp} &= \left(-2\frac{\omega_p^2-(2\omega)^2}{\omega_0^2-(2\omega)^2}\right)\frac{1}{4}\frac{\epsilon_0}{en}\frac{\omega_p^4}{\omega^4}E_{1\perp}E_{1\perp} \end{aligned}$$

where ω_0 is an effective plasma frequency in the selvedge for the second-harmonic sources. In conclusion, following the hydrodynamic model by Sipe *et al.*, the Rudnick-Stern parameters are predicted to be:

$$\begin{aligned} b &= -1 \\ a &= -2\frac{\omega_p^2-(2\omega)^2}{\omega_0^2-(2\omega)^2}\ . \end{aligned}$$

Consequently, is it clear that Sipe *et al.*predicted a negative value for b, while $b > 0$ in the discussion conducted by Rudnick and Stern. Moreover, the model proposed by Sipe *et al.*predicts that the value of a is driven by resonance effects in proximity of the selvedge plasma frequency ω_0. It is worth noticing that the calculations of the hydrodynamic model by Sipe *et al.* were confirmed by similar calculations by Corvi and Schaich [44].

3

METAL NANOPARTICLES

Nanoparticles are three-dimensional structures with maximum size less than $\sim 1\ \mu m$. They can present several shapes, such as spherical, cylindrical, triangular, etc. If one dimension much larger than the others, they are usually called nanowires or nanorods. Nanoparticles can be made of several materials, including dielectrics and conductors. In the present Chapter we describe the response of noble metal nanoparticles (i. e. gold, silver, copper) to an external e.m. field .

The electromagnetic properties of noble metal nanoparticles are strongly affected by plasmonic resonances, i. e. collective oscillation of the conduction electrons, typically occurring in the optical range, as described in Chapter 2. In metal nano-structures, whose dimensions are comparable with the incident wavelength λ, the plasmon resonances are affected by the shape and the surface properties of the nano-object, as we will show later in this Chapter. For this reason, a collective resonance of conduction electrons in metal nano-structured is called Localized Surface Plasmon (LSP). In metal nanostructures with one dimension larger than λ, such as nano-wires, the conduction electron resonances can propagate, resulting in a different effect called Surface Plasmon Polariton (SPP), associated to evanescent waves propagating along a metal surface. The electric field is localized within a short distance from the surface, much smaller than the wavelength. LSPs and SPPs confer very special optical properties to the metal nano-structure sustaining them.

In this Chapter, we first describe the electromagnetic response of noble metal nanoparticles in the framework of the electrostatic approximation, i. e. the Rayleigh scattering, in which the incident wavelength is assumed to be much larger than the particle size ($R << \lambda$). Then, we introduce Mie's theory of light scattering by spherical particle, which takes into account the effects of particle size, i. e. the retardation effects of the e.m. field inside the particle. The resonance conditions of the field are presented, along with the main optical properties.

Eventually, the second-harmonic Rayleigh scattering of light is introduced at the end of the present Chapter. THE SECOND-ORDER NONLINEAR RESPONSE OF METAL NANOPARTICLES WILL BE DISCUSSED IN SECTION III, WHERE A COMPLETE MIE-THEORY-BASED FORMULATION OF SECOND-HARMONIC LIGHT SCATTERING IS INTRODUCED, AS FUNDAMENTAL PART OF THE PRESENT THESIS. This nonlinear optical process will be described for the first time by taking into account all the relevant sources of nonlinearity.

3.1 RAYLEIGH THEORY

Let us consider the problem of scattering of a monochromatic light from a spherical metal particle with radius R and permittivity $\varepsilon_i(\omega)$, embedded in a medium with permittivity $\varepsilon_e(\omega)$. Let the radius be small compared to the incident wavelength λ. Then, we can decompose the incident field $\boldsymbol{E}_{\text{inc}}$ in Taylor's series at the particle center $\boldsymbol{r}_0$ as:

$$\boldsymbol{E}_{\text{inc}}(\boldsymbol{r}) = \boldsymbol{E}_{\text{inc}}(\boldsymbol{r} = \boldsymbol{r}_0) + \boldsymbol{r} \cdot \nabla_{\boldsymbol{r}'} \boldsymbol{E}_{\text{inc}}|_{\boldsymbol{r}'=\boldsymbol{r}_0} + O(r^2) \; . \tag{3.1}$$

If the particle is homogeneous, then Equation 3.1 can be rewritten as:

$$\boldsymbol{E}_{\text{inc}}(\boldsymbol{r}) = \boldsymbol{E}^0_{\text{inc}} + \frac{1}{2}\boldsymbol{C}^0_{\text{inc}}\boldsymbol{r} - i\frac{1}{2}\omega\boldsymbol{B}^0_{\text{inc}} \times \boldsymbol{r} + O(r^2) \; , \tag{3.2}$$

where $\boldsymbol{C}^0_{\text{inc}} = \nabla_{\boldsymbol{r}'}\boldsymbol{E}_{\text{inc}}|_{\boldsymbol{r}'=\boldsymbol{r}_0} + (\nabla_{\boldsymbol{r}'}\boldsymbol{E}_{\text{inc}}|_{\boldsymbol{r}'=\boldsymbol{r}_0})^T - \frac{2}{3}(\nabla_{\boldsymbol{r}'} \cdot \boldsymbol{E}_{\text{inc}}|_{\boldsymbol{r}'=\boldsymbol{r}_0})\boldsymbol{I}$, $\boldsymbol{I}$ is the identity tensor, $\nabla \times \boldsymbol{E}_{\text{inc}} = -i\omega\boldsymbol{B}_{\text{inc}}$ and $\boldsymbol{E}^0_{\text{inc}} = \boldsymbol{E}_{\text{inc}}(\boldsymbol{r} = \boldsymbol{r}_0)$.

The incident field and the field inside the particle can be linked by the electric and magnetic screening factors $L_{Ei}(\omega)$ and $L_{Mi}(\omega)$:

$$\boldsymbol{E}_{\text{int}}(\boldsymbol{r}) = L_{E1}\boldsymbol{E}^0_{\text{inc}} + \frac{L_{E2}}{2}\boldsymbol{C}^0_{\text{inc}}\boldsymbol{r} - i\omega\frac{L_{M1}}{2}\boldsymbol{B}^0_{\text{inc}} \times \boldsymbol{r} + O(r^2) \; , \tag{3.3}$$

where $L_{El}(\omega) = \frac{(2l+1)\varepsilon_e(\omega)}{l\varepsilon_i(\omega)+(l+1)\varepsilon_e(\omega)}$ for $l = 1, 2$ and $L_{M1} = 1$ for a diamagnetic particle in empty space. In particular, the screening factor for metal particles in empty space can be found by using the permittivity $\varepsilon(\omega)$ derived from the Drude-Sommerfeld model:

$$L_{El}(\omega) = \frac{(2l+1)(\omega^2 - i\nu\omega)}{(2l+1)\omega^2 - l\omega_p^2 - i(2l+1)\nu\omega} \; . \tag{3.4}$$

The induced electric dipole $\boldsymbol{p}$, magnetic dipole $\boldsymbol{m}$ and the electric quadrupole $\boldsymbol{Q}$ in the particle, as defined in Appendix A.2, are then:

$$\begin{aligned}
\boldsymbol{p} &= \varepsilon_0 V\chi(\omega)L_1\boldsymbol{E}^0_{\text{inc}} \; , \\
\boldsymbol{m} &= \varepsilon_0\frac{1}{10}VR^2\chi(\omega)\omega^2\boldsymbol{B}^0_{\text{inc}} \; , \\
\boldsymbol{Q} &= \varepsilon_0\frac{1}{5}VR^2\chi(\omega)L_2\boldsymbol{C}^0_{\text{inc}} \; .
\end{aligned}$$

The scattered electric field can be expressed as:

$$\boldsymbol{E}_{\text{scat}} = k^2\frac{e^{-ikr}}{4\pi\varepsilon_0 r}[\hat{\boldsymbol{r}} \times \boldsymbol{p}_{\text{eff}}] \times \hat{\boldsymbol{r}} \; , \tag{3.5}$$

where

$$\boldsymbol{p}_{\text{eff}} = \boldsymbol{p} - \frac{1}{c}\hat{\boldsymbol{r}} \times \boldsymbol{m}^{(2\omega)} + \frac{ik}{6}\boldsymbol{Q}^{(2\omega)}\hat{\boldsymbol{r}} \; . \tag{3.6}$$

The condition $R << \lambda/2\pi$ defines the Rayleigh regime, in which the electric field $\boldsymbol{E}_{\mathrm{int}}$ can be considered as constant overall the particle volume. In this case, only the electric dipole $\boldsymbol{p}$ contributes to the scattering of an external electric field by the particle.

The scattered electric field in the Rayleigh approximation is represented in Fig. 3.1(a), for the case of an external plane-wave linearly polarized along the x-axis and propagating in the positive direction of the z-axis. The particle size is $R = 10$ nm and the wavelength is $\lambda = 800$ nm. A typical dipolar pattern is produced.

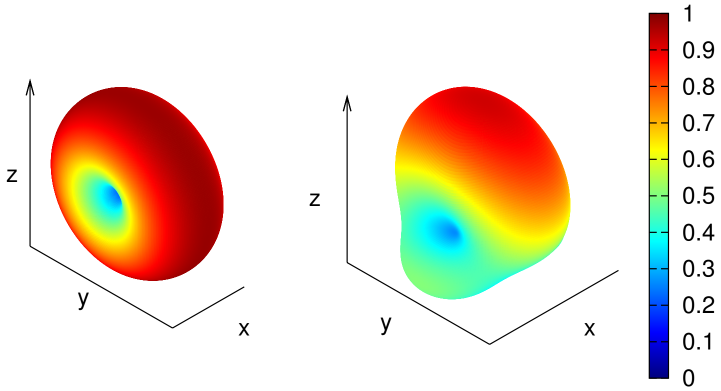

Figure 3.1: Scattered electric field, normalized to its maximum, by a metal particle with $R = 10$ nm (a) and $R = 150$ nm (b). The incident field is a plane wave propagating in the positive direction of the z-axis and linearly polarized along the x-axis. The wavelength is $\lambda = 800$ nm (a) and $\lambda = 550$ nm (b).

The scattering properties of particles with comparable size to the incident wavelength cannot be examined in the Rayleigh approximation, and higher order multipoles must be taken into account to express the internal and scattered fields. This approach will be discussed in the next Section.

3.2 MIE THEORY

The theory of interaction between spherical particles and light with comparable wavelength to the radius was studied at the beginning of the 20th century by Gustav Mie [53]. In particular, the problem of scattering was solved in 1908 by expanding the incident, internal and scattered fields in series of Spherical Vector WaveFunctions (SVWFs) (see Appendix A.6).

The electromagnetic field must satisfy the Maxwell's equations:

$$\begin{cases} \nabla \times \mathbf{E}_i^{(\omega)} = -i\omega\mu_i \mathbf{H}_i^{(\omega)} \\ \nabla \times \mathbf{H}_i^{(\omega)} = +i\omega\varepsilon_i(\omega)\, \mathbf{E}_i^{(\omega)} \end{cases} \quad \text{in } \Omega_i \,, \tag{3.7a}$$

$$\begin{cases} \mathbf{n} \times \left(\mathbf{H}_i^{(\omega)} - \mathbf{H}_{sc}^{(\omega)}\right) = \mathbf{n} \times \mathbf{H}_0^{(\omega)} \\ \mathbf{n} \times \left(\mathbf{E}_i^{(\omega)} - \mathbf{E}_{sc}^{(\omega)}\right) = \mathbf{n} \times \mathbf{E}_0^{(\omega)} \end{cases} \quad \text{on } \Sigma \,, \tag{3.7b}$$

$$\begin{cases} \nabla \times \mathbf{E}_{sc}^{(\omega)} = -i\omega\mu_e \mathbf{H}_{sc}^{(\omega)} \\ \nabla \times \mathbf{H}_{sc}^{(\omega)} = +i\omega\varepsilon_e \mathbf{E}_{sc}^{(\omega)} \end{cases} \quad \text{in } \Omega_e \,, \tag{3.7c}$$

where $\left(\mathbf{E}_i^{(\omega)}, \mathbf{H}_i^{(\omega)}\right)$ denote the fields in $\dot{\Omega}_i$ and $\left(\mathbf{E}_{sc}^{(\omega)}, \mathbf{H}_{sc}^{(\omega)}\right)$ denote the scattered fields in $\dot{\Omega}_e$, namely $\mathbf{E}_{sc}^{(\omega)} = \mathbf{E}_e^{(\omega)} - \mathbf{E}_0^{(\omega)}$ and $\mathbf{H}_{sc}^{(\omega)} = \mathbf{H}_e^{(\omega)} - \mathbf{H}_0^{(\omega)}$. Equations (3.7) have to be solved with the radiation condition at infinity for the scattered fields.

Due to the symmetry of the problem, the general solution of the source-free Maxwell equations can be expressed in each homogeneous region through the SVWFs $\mathbf{M}_{mn}^{(J)}$ and $\mathbf{N}_{mn}^{(J)}$. The incident planewave $\left(\mathbf{E}_0^{(\omega)}, \mathbf{H}_0^{(\omega)}\right)$ can be decomposed in Eq. (3.8a) through the regular SVWFs, non-singular in the center of the sphere ($J = 1$), where $E_0 = |\mathbf{E}_0|$. Also the unknown fields $\left(\mathbf{E}_i^{(\omega)}, \mathbf{H}_i^{(\omega)}\right)$ in Ω_i ($0 \leqslant r < R$), are decomposed through the regular SVWFs in Eq. (3.8b), where $\zeta_i(\omega) = \sqrt{\mu_i/\varepsilon_i(\omega)}$, $k_i(\omega) = \omega\sqrt{\varepsilon_i(\omega)\,\mu_i}$. The unknown scattered fields $\left(\mathbf{E}_{sc}^{(\omega)}, \mathbf{H}_{sc}^{(\omega)}\right)$ in $\dot{\Omega}_e$ (for $R < r$) are instead decomposed in Eq. (3.8c) through the radiative SVWFs, satisfying the radiation condition at infinity ($J = 3$).

$$\begin{aligned} \mathbf{E}_0^{(\omega)}(r,\theta,\phi) = -E_0 \sum_{n=1}^{\infty} \sum_{m=-n}^{n} \Big\{ & q_{mn}^{(\omega)} \mathbf{M}_{mn}^{(1)}\left[k_e(\omega)\, r, \theta, \phi\right] \\ & + p_{mn}^{(\omega)} \mathbf{N}_{mn}^{(1)}\left[k_e(\omega)\, r, \theta, \phi\right] \Big\} \\ \mathbf{H}_0^{(\omega)}(r,\theta,\phi) = \frac{E_0}{i\zeta_e} \sum_{n=1}^{\infty} \sum_{m=-n}^{n} \Big\{ & p_{mn}^{(\omega)} \mathbf{M}_{mn}^{(1)}\left[k_e(\omega)\, r, \theta, \phi\right] \\ & + q_{mn}^{(\omega)} \mathbf{N}_{mn}^{(1)}\left[k_e(\omega)\, r, \theta, \phi\right] \Big\} \,, \end{aligned} \tag{3.8a}$$

$$\begin{aligned}
\mathbf{E}_i^{(\omega)}(r,\theta,\phi) &= -E_0 \sum_{n=1}^{\infty} \sum_{m=-n}^{n} \Big\{ c_{mn}^{(\omega)} \mathbf{M}_{mn}^{(1)} \left[k_i(\omega) r,\theta,\phi\right] \\
&\qquad + d_{mn}^{(\omega)} \mathbf{N}_{mn}^{(1)} \left[k_i(\omega) r,\theta,\phi\right] \Big\} \\
\mathbf{H}_i^{(\omega)}(r,\theta,\phi) &= \frac{E_0}{i\zeta_i(\omega)} \sum_{n=1}^{\infty} \sum_{m=-n}^{n} \Big\{ d_{mn}^{(\omega)} \mathbf{M}_{mn}^{(1)} \left[k_i(\omega) r,\theta,\phi\right] \\
&\qquad + c_{mn}^{(\omega)} \mathbf{N}_{mn}^{(1)} \left[k_i(\omega) r,\theta,\phi\right] \Big\},
\end{aligned} \tag{3.8b}$$

$$\begin{aligned}
\mathbf{E}_{sc}^{(\omega)}(r,\theta,\phi) &= E_0 \sum_{n=1}^{\infty} \sum_{m=-n}^{n} \Big\{ b_{mn}^{(\omega)} \mathbf{M}_{mn}^{(3)} \left[k_e(\omega) r,\theta,\phi\right] \\
&\qquad + a_{mn}^{(\omega)} \mathbf{N}_{mn}^{(3)} \left[k_e(\omega) r,\theta,\phi\right] \Big\} \\
\mathbf{H}_{sc}^{(\omega)}(r,\theta,\phi) &= -\frac{E_0}{i\zeta_e} \sum_{n=1}^{\infty} \sum_{m=-n}^{n} \Big\{ a_{mn}^{(\omega)} \mathbf{M}_{mn}^{(1)} \left[k_e(\omega) r,\theta,\phi\right] \\
&\qquad + b_{mn}^{(\omega)} \mathbf{N}_{mn}^{(1)} \left[k_e(\omega) r,\theta,\phi\right] \Big\}.
\end{aligned} \tag{3.8c}$$

The decomposition (3.8c) of $\left(\mathbf{E}_{sc}^{(\omega)}, \mathbf{H}_{sc}^{(\omega)}\right)$ satisfy Eq. (3.7c), and the decomposition (3.8b) of $\left(\mathbf{E}_i^{(\omega)}, \mathbf{H}_i^{(\omega)}\right)$ satisfy Eq. (3.7a). The unknown coefficients $\left\{a_{mn}^{(\omega)}, b_{mn}^{(\omega)}\right\}$ and $\left\{c_{mn}^{(\omega)}, d_{mn}^{(\omega)}\right\}$ are determined by requiring that the decompositions (3.8b,3.8c) also satisfy the boundary conditions (3.7b). The analytical expressions of $\left\{a_{mn}^{(\omega)}, b_{mn}^{(\omega)}\right\}$ and $\left\{c_{mn}^{(\omega)}, d_{mn}^{(\omega)}\right\}$ as functions of $\{p_{mn}, q_{mn}\}$ are:

$$\begin{aligned}
\frac{a_{mn}^{(\omega)}}{p_{mn}^{(\omega)}} &= \frac{\frac{\zeta_e}{\zeta_i(\omega)}\, \psi_n(x_i^{(\omega)})\, \dot{\psi}_n(x_e^{(\omega)}) - \psi_n(x_e^{(\omega)})\, \dot{\psi}_n(x_i^{(\omega)})}{\frac{\zeta_e}{\zeta_i(\omega)}\, \psi_n(x_i^{(\omega)})\, \dot{\xi}_n(x_e^{(\omega)}) - \xi_n(x_e^{(\omega)})\, \dot{\psi}_n(x_i^{(\omega)})} \\
\frac{b_{mn}^{(\omega)}}{q_{mn}^{(\omega)}} &= \frac{\psi_n(x_i^{(\omega)})\, \dot{\psi}_n(x_e^{(\omega)}) - \frac{\zeta_e}{\zeta_i(\omega)}\, \psi_n(x_e^{(\omega)})\, \dot{\psi}_n(x_i^{(\omega)})}{\psi_n(x_i^{(\omega)})\, \dot{\xi}_n(x_e^{(\omega)}) - \frac{\zeta_e}{\zeta_i(\omega)}\, \xi_n(x_e^{(\omega)})\, \dot{\psi}_n(x_i^{(\omega)})} \\
\frac{c_{mn}^{(\omega)}}{q_{mn}^{(\omega)}} &= \frac{i\frac{k_i(\omega)}{k_e(\omega)}}{\psi_n(x_i^{(\omega)})\, \dot{\xi}_n(x_e^{(\omega)}) - \frac{\zeta_e}{\zeta_i(\omega)}\, \xi_n(x_e^{(\omega)})\, \dot{\psi}_n(x_i^{(\omega)})} \\
\frac{d_{mn}^{(\omega)}}{p_{mn}^{(\omega)}} &= \frac{i\frac{k_i(\omega)}{k_e(\omega)}}{\frac{\zeta_e}{\zeta_i(\omega)}\, \psi_n(x_i^{(\omega)})\, \dot{\xi}_n(x_e^{(\omega)}) - \xi_n(x_e^{(\omega)})\, \dot{\psi}_n(x_i^{(\omega)})}
\end{aligned} \tag{3.9}$$

where $x_e^{(\omega)} = k_e^{(\omega)} R,\ \ x_i^{(\omega)} = k_i^{(\omega)}$ and $\psi_n = \psi_n(\rho)$, $\xi_n = \xi_n(\rho)$ are the Riccati-Bessel functions defined as $\psi_n(\rho) = \rho\, j_n(\rho)$, $\xi_n = \rho\, h_n^{(1)}(\rho)$. $\dot{\zeta}$ denotes the first derivative of $\zeta = \zeta(\rho)$ with respect to ρ.

The expansion coefficients in Eq. (3.8a), for a linearly polarized plane-wave propagating along the $z-$axis with the electric field parallel to the $x-$axis (Fig. 6.1a), are:

$$\begin{aligned} &p_{mn}^{(\omega)} = q_{mn}^{(\omega)} = 0, \text{ for } |m| \neq 1 \\ &p_{1n}^{(\omega)} = q_{1n}^{(\omega)} = -p_{-1n}^{(\omega)} = q_{-1n}^{(\omega)} = \frac{1}{2}(-i)^n\sqrt{4\pi(2n+1)} \end{aligned}$$

In the Mie theory, all the SVWF multipoles are involved in the calculation of the internal and scattered fields. In a numerical implementation, the multipoles are considered up to an arbitrary order $n = N_{max}$ The scattered intensity is represented in Fig. 3.1 for the case of an external plane-wave linearly polarized along the x-axis and propagating along the positive direction of the z-axis. The particle size is $R = 150$ nm and the wavelength is $\lambda = 550$ nm. The pattern is mostly produced by the interference of the dipolar and quadrupolar SVWFs, i. e. $n = 1$ and $n = 2$.

3.2.1 *Multiparticle Mie theory*

Mie's analytical approach was extended about 100 years later [54], in order to account for the scattering from a set of interacting spheres, i. e. for the multiparticle scattering. The semi-analytical approach to the multiparticle-particle light scattering will be briefly introduced here, as it is of interest for the present Thesis. In particular, in Chapters 4 and 5, the design of innovative nanolens systems will be performed by means of a rigorous electromagnetic solver based on the multiparticle Mie theory.

Given a set of N spherical particles, we can consider N reference systems having origin in each particle center. The field scattered by the $j-th$ particle can be expressed as in Eq. 3.8c, in the reference system of the $j-th$ particle itself (r^j, θ^j, ϕ^j) :

$$\begin{aligned} \mathbf{E}_{sc}^{jj(\omega)}\left(r^j,\theta^j,\phi^j\right) = E_0 \sum_{n=1}^{\infty}\sum_{m=-n}^{n} \Big\{ & b_{mn}^{jj(\omega)}\mathbf{M}_{mn}^{(3)}\left[k_e(\omega)\, r^j,\theta^j,\phi^j\right] \\ & + a_{mn}^{jj(\omega)}\mathbf{N}_{mn}^{(3)}\left[k_e(\omega)\, r^j,\theta^j,\phi^j\right]\Big\} \\ \mathbf{H}_{sc}^{jj(\omega)}\left(r^j,\theta^j,\phi^j\right) = -\frac{E_0}{i\zeta_e} \sum_{n=1}^{\infty}\sum_{m=-n}^{n} \Big\{ & a_{mn}^{jj(\omega)}\mathbf{M}_{mn}^{(1)}\left[k_e(\omega)\, r^j,\theta^j,\phi^j\right] \\ & + b_{mn}^{jj(\omega)}\mathbf{N}_{mn}^{(1)}\left[k_e(\omega)\, r^j,\theta^j,\phi^j\right]\Big\}. \end{aligned}$$

The same field can be expanded with respect of the $i-th$ particle reference system (r^i, θ^i, ϕ^i):

$$\begin{aligned}\mathbf{E}_{sc}^{ji(\omega)}\left(r^i,\theta^i,\phi^i\right) &= E_0 \sum_{n=1}^{\infty}\sum_{m=-n}^{n}\left\{b_{mn}^{ji(\omega)}\mathbf{M}_{mn}^{(3)}\left[k_e(\omega)\,r^i,\theta^i,\phi^i\right]\right.\\ &\left.+a_{mn}^{ji(\omega)}\mathbf{N}_{mn}^{(3)}\left[k_e(\omega)\,r^i,\theta^i,\phi^i\right]\right\}\\ \mathbf{H}_{sc}^{ji(\omega)}\left(r^i,\theta^i,\phi^i\right) &= -\frac{E_0}{i\zeta_e}\sum_{n=1}^{\infty}\sum_{m=-n}^{n}\left\{a_{mn}^{ji(\omega)}\mathbf{M}_{mn}^{(1)}\left[k_e(\omega)\,r^i,\theta^i,\phi^i\right]\right.\\ &\left.+b_{mn}^{ji(\omega)}\mathbf{N}_{mn}^{(1)}\left[k_e(\omega)\,r^i,\theta^i,\phi^i\right]\right\}.\end{aligned}$$

where the coefficients $\left\{a_{mn}^{ji(\omega)}, b_{mn}^{ji(\omega)}\right\}$ are linearly related to the coefficients $\left\{a_{mn}^{jj(\omega)}, b_{mn}^{jj(\omega)}\right\}$, through the translation addition theorem [54].

In the multiparticle scattering problem, the total field incident upon the $i-th$ particle is the sum of the incident wave $\boldsymbol{E}_0^{(\omega)}$ and the field scattered by all the other particle in the system:

$$\boldsymbol{E}_{inc}^{i(\omega)} = \boldsymbol{E}_0^{i(\omega)} + \sum_{j\neq i}\boldsymbol{E}_{sc}^{ji(\omega)} \tag{3.10}$$

By using the single particle Mie solution and the translation addition theorem, it is possible to determine the unknown coefficients $\left\{a_{mn}^{ii(\omega)}, b_{mn}^{ii(\omega)}\right\}$, by means of an iterative method:

1. At the beginning, the incident field on the $i-th$ particle is assumed to be solely due to $\boldsymbol{E}_0^{(\omega)}$.
2. The field scattered on the $i-th$ particle by all the others $j \neq i$ is calculated
3. The total incident field on the $j-th$ particle is calculated as the sum in Eq. 3.10
4. The scattered field by the $i-th$ particle is calculated

The last three steps are iterated until the unknown fields converge with a given criterion.

3.3 SURFACE PLASMON RESONANCES

The interaction of light with metal nanoparticles is of extreme interest due to the combination of the metal microscopic response, described by the permittivity $\varepsilon(\omega)$ (see Chapter 2), and the size effects, accounted for by the Rayleigh theory or by the Mie theory, in the case of spherical shape. Metal nanoparticles show special electromagnetic properties, as demonstrated by analyzing optical parameters, such as the light absorption, scattering and the field amplitude near the surface.

For instance, let us consider the *scattering cross-section* of the particle, which represents the area of a scatter of an equal power under the hypothesis of ray-propagation [27], defined as:

$$C_{sca} = \lim_{\rho \to \infty} \frac{\int_{\Sigma_\rho} |\mathbf{E}_{sc}|^2 \cdot \hat{\mathbf{n}}\, d\Sigma}{{E_0}^2}, \tag{3.11}$$

Figure 3.2 represents C_{sca} as a function of the incident wavelength, for gold particles of different sizes. For small sizes, i. e. in the Rayleigh regime, C_{sca} is mostly due to the dipolar SVWF. It decreases with the wavelength and presents a peak in the wavelength range $500\ \mathrm{nm} - 600\ \mathrm{nm}$. This peak corresponds to a dipolar resonance of the metal conduction electrons with the particle shape(Fig.3.2a). In the frame of the Rayleigh theory, the dipolar resonance is obtained if the denominator of Eq. 3.4 tends to zero. If the collision frequency ν is neglected, this condition is verified at $\omega \approx \omega_p/\sqrt{3}$.

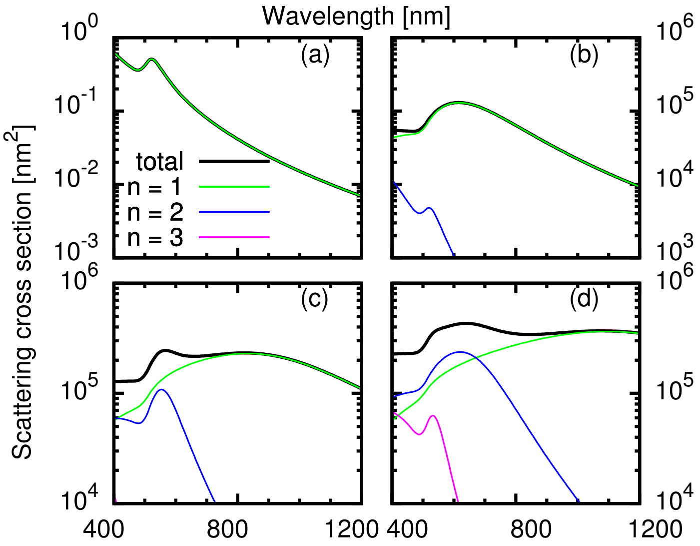

Figure 3.2: Scattering cross-section of gold nano-spheres as function of the incident wavelength λ, for $R = 10\ \mathrm{nm}$ (a), $R = 100\ \mathrm{nm}$ (b), $R = 150\ \mathrm{nm}$ (c), $R = 200\ \mathrm{nm}$ (d).

The dipolar resonance red-shifts when the particle size increases, and a broadening can be observed (Fig.3.2b). For very large particles

(Fig.3.2c and d), higher order resonances of the conduction electrons take place and govern the electromagnetic response of the particle. In the frame of the Mie theory, the resonance condition for the general multipole of order n is obtained if the denominator of the coefficients in Eq. 3.9 tends to zero.

Figure 3.3 represents C_{sca} as function of the metal particle radius, for three incident wavelength λ. For small sizes, the Mie theory confirms the Rayleigh theory prediction of the scaling $C_{sca} \propto r^4$. As the particle increases in size, small modulations of C_{sca} occur until a saturation value is reached.

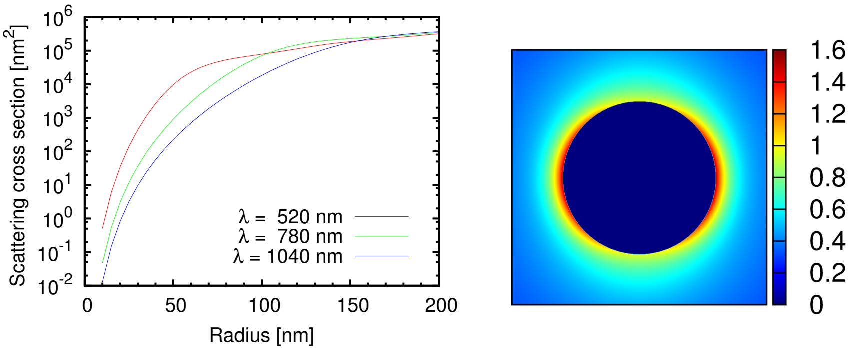

Figure 3.3: (Left) Scattering cross-section of metal nano-spheres as function of the radius R, for $\lambda = 520$ nm, $\lambda = 780$ nm, $\lambda = 1040$ nm. (Right) Electric field amplitude in proximity of a gold nanosphere with $R = 150$ nm, normalized to the amplitude of the incident plane-wave with $\lambda = 550$ nm.

The multipolar resonances in metal nanoparticles are due to the collective oscillation of the conduction electrons, and they are generally known as Localized Surface Plasmon (LSP) resonances, for the property of being strictly related to the particle geometry. The scattering cross-section can reach very high values compared to the surface extension of the particle itself, due to the LSP resonances. This characteristic enhancement involves also other properties of the particle electromagnetic response, like the absorption of light and the local field near the particle surface. In particular, the Near Field Enhancement (NFE) of a metal nanoparticles gathers enormous attention in the scientific community, due to the possibility to increase the cross-sections of optical processes occurring in proximity of the particle, such as the SERS. Figure 3.3 clearly shows the near-field enhancement in proximity of a Au nano-sphere exponentially decaying from the particle surface. The enhancement distribution over the particle surface depends on the multipolar order of the excited resonance. The near-field enhancement can be more strongly boosted in clusters and arrays of nanoparticles, that will be investigated in Part ii of the present Thesis.

3.4 SECOND-HARMONIC RAYLEIGH THEORY

The optical nonlinear properties of metal particles have been widely investigated in the last decades [55, 56, 57, 58, 59, 60]. As already pointed out in the Section 2.4, both the bulk and selvedge significantly contribute to the second-order nonlinear response of a metal domain.

From a phenomenological point of view [48], the second-order bulk and surface polarizations can be respectively expressed as:

$$\begin{aligned} \boldsymbol{P}_{\mathrm{b}}^{(2\omega)} &= \varepsilon_0 \gamma \nabla (\boldsymbol{E}^{(\omega)} \cdot \boldsymbol{E}^{(\omega)}) + \varepsilon_0 \delta' (\boldsymbol{E}^{(\omega)} \cdot \nabla) \boldsymbol{E}^{(\omega)} \qquad & [\mathrm{Cm}^{-2}] \\ \boldsymbol{P}_{\mathrm{s}}^{(2\omega)} &= \varepsilon_0 \overleftrightarrow{\chi}_{\mathrm{s}}^{(2)} : \boldsymbol{E}^{(\omega)} \boldsymbol{E}^{(\omega)} & [\mathrm{Cm}^{-1}] \,, \end{aligned}$$

where γ, δ' and the elements of $\overleftrightarrow{\chi}_{\mathrm{s}}^{(2)}$ are in units of $[\mathrm{m}^2\mathrm{V}^{-1}]$, and quantify the contribution of each nonlinear source to the second-order polarization. In the hypothesis that the surface is isotropic and it has a mirror plane perpendicular to it, the only allowed elements of $\overleftrightarrow{\chi}_{\mathrm{s}}^{(2)}$ are $\chi_{\perp\perp\perp}$, $\chi_{\parallel\parallel\perp} = \chi_{\parallel\perp\parallel}$ and $\chi_{\perp\parallel\parallel}$.

Let us examine the second-order nonlinear scattering from a spherical metal particle in the Rayleigh regime, following the analysis conducted by Dadap *et al.*[61]. We consider the external field expansion in 3.2, then the electric dipole $\boldsymbol{p}^{(2\omega)}$ and quadrupole $\boldsymbol{Q}^{(2\omega)}$ at angular frequency 2ω are:

$$\begin{aligned} \boldsymbol{p}^{(2\omega)} &= \gamma_{\mathrm{ed}} \boldsymbol{C}_{\mathrm{inc}}^{0} \boldsymbol{E}_{\mathrm{inc}}^{0} + i\omega \gamma_{\mathrm{md}} \boldsymbol{E}_{\mathrm{inc}}^{0} \times \boldsymbol{B}_{\mathrm{inc}}^{0} \\ \boldsymbol{Q}^{(2\omega)} &= \gamma_{\mathrm{q}} [\boldsymbol{E}_{\mathrm{inc}}^{0} \boldsymbol{E}_{\mathrm{inc}}^{0} - \frac{1}{3} (\boldsymbol{E}_{\mathrm{inc}}^{0} \cdot \boldsymbol{E}_{\mathrm{inc}}^{0})^{\mathrm{T}} \boldsymbol{I}] \,, \end{aligned}$$

and the magnetic dipole $\boldsymbol{m}^{(2\omega)}$ is zero because of the axial symmetry of the problem. The coefficients γ_{ed}, γ_{md} and γ_{q} are the weight coefficients for the electric dipole, electric quadrupole and magnetic dipole, and their expression is provided in [61]. They depend on the screening factors and the permittivity at frequencies ω and 2ω.

It is important to remark that the second-order bulk and surface sources contribute only to specific electric and magnetic multipoles, due to the *selection rules* governing the process [62]. In particular, in the frame of the second-harmonic Rayleigh scattering theory:

- all the sources contribute to the electric dipole
- only the surface sources contribute to the electric quadrupole
- all the sources but $\chi_{\perp\perp\perp}$ contribute to the magnetic dipole

An analysis of the second-harmonic Rayleigh scattering will be conducted in Part iii, where it will be compared to the more complete *second-harmonic Mie scattering*, which has been developed as significant part of the present Thesis.

Part II

PLASMONIC NANOLENSES

4

PLASMONIC HETERODIMERS

An increasing interest has recently raised on nanostructures composed by different metals, known as *plasmonic heterostructures*, for the design of photonic devices [63, 64, 65, 66]. The specific case of two nanoparticles, called *heterodimer*, features a strong coupling between the LSPs in the two elements, allowing for the tunability of their optical properties. Let us begin considering the dipolar resonance modes ψ_1 and ψ_2 of the two compounding elements. Their coupling is usually studied in the framework of molecular hybridization [67, 68, 69].

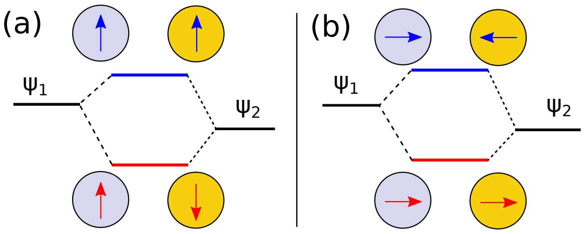

Figure 4.1: Hybridization model for two different interacting nanoparticles, in the case of transverse (a) and longitudinal (b) polarization, with respect to the dimer axis. The dipolar modes ψ_1 and ψ_2 give rise to bounding (red) and antibonding (blue) modes.

The interaction between the heterodimer and an incident light gives rise to two hybrid modes at different energy. If the light polarization is transverse to the dimer axis, as shown in Fig. 4.1(a), then the 'bounding' mode (red), is characterized by parallel dipolar moments in phase opposition, while the 'antibonding' mode (blue) is characterized by in-phase parallel dipolar moments. The case of incident light polarized parallel to the dimer axis is shown in Fig. 4.1(b). The bounding mode (red) is characterized by in-phase dipole moments, while the anti-bounding mode (blue) is characterized by dipole moments in phase opposition. In both cases, the bounding mode resonates at lower frequencies than the 'anti-bounding' mode. Consequently, the LSP exhibits a red-shift in case of the bounding mode, and a blue-shift for the antibonding one, with respect to the case of isolated particles.

This hybridization model can be extended to consider higher order multipolar interactions between the two metal nanoparticles. However, this approach is not numerically efficient to study the optical properties of metal nanoparticles with arbitrary size and with nontrivial dispersion relations.

In this Chapter, we perform a numerical analysis of the optical properties of plasmonic heterodimers composed by spherical particles made of silver (Ag) and gold (Au), by means of the multiparticle Mie theory, introduced in Chapter 3. The optical response of these heterostructures is investigated in the wavelength range 300 nm − 900 nm in terms of the scattering efficiency and of the NFE, calculated on the particle surfaces and outside it. Johnson and Christie's dispersion relations are adopted for the two considered metals.

First, we investigate heterodimers composed by particles with the same size, i. e. symmetric heterodimers, and then we study the effects of the size asymmetry. Eventually, we consider the response of arrays of plasmonic heterodimers, both in the symmetric and asymmetric cases.

4.1 SYMMETRIC HETERODIMERS

In this Section, we investigate the optical response of plasmonic heterodimers composed by particles of equal radii, for the two cases $R = 25$ nm and $R = 50$ nm. The scattering efficiency spectra are represented in Fig. 4.2(a) for heterodimers with radii $R = 25$ nm, excited by a transverse polarized plane wave, with an edge-to-edge distance varying in the range 5 nm − 25 nm.

Two distinct resonance peaks appear at the typical wavelengths of isolated Ag (≈ 370 nm) and Au (≈ 520 nm) particles, for any values of the inter-particle distance. The peak amplitude corresponding to the Ag particle is much higher then the one corresponding to the Au particle, because of lower losses in the first metal. A weak near-field coupling between the two particles composing the heterodimer can be detected: the peak amplitude associated to the Ag decreases for small interparticle distances. As a matter of fact, the shorter is the heterodimer gap, the more electromagnetic power scattered by the Ag particle is dissipated in the Au particle.

The scattering efficiency is represented in Fig. 4.2(b) in the case of incident light with longitudinal polarization. In this situation, stronger effects of near-field coupling can be detected than the case of transverse polarized light. As a matter of fact, the scattering efficiency associated to the Au particle is higher than the previous case, and it further increases as the interparticle distance decreases. Moreover, a substantial red-shift can be observed in both peaks for decreasing interparticle distances.

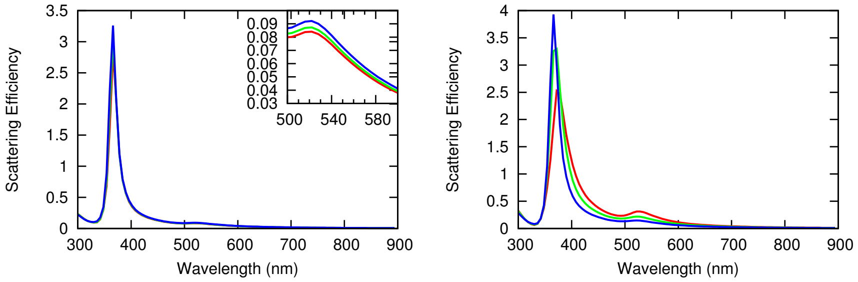

Figure 4.2: Scattering efficiency for symmetric heterodimers with $R = 25$ nm, in case of incident light with transverse (left) and longitudinal (right) polarizations. The interparticle edge-to-edge distance is $D = 5$ nm (red), $D = 10$ nm (green), $D = 25$ nm (blue).

The spectral shifts of the resonance peaks corresponding to Ag and Au are summarized in Fig. 4.3, for both transverse and longitudinal polarizations. A red-shift is observed for both peaks if the interparticle distances decrease, in the case of longitudinal polarization. This trend is interrupted only for the Ag peak for distances lower then 2 nm, where a blue shift takes place.

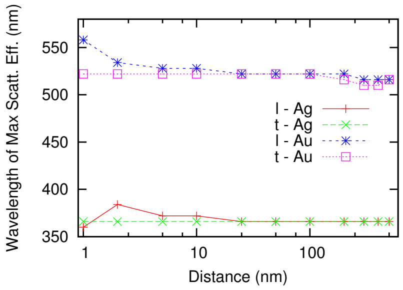

Figure 4.3: Spectral position of the Ag and Au scattering peaks, in case of transverse (t) and longitudinal (l) polarization of the incident light, for a symmetric heterodimer with $R = 25$ nm.

The maximum NFE probed on the particle surface is represented in Fig. 4.4(a) in the spectral range 300 nm – 900 nm, in the case of incident light with longitudinal polarization. High values of NFE can be observed at typical resonance wavelengths for Ag and Au, as well as at intermediate wavelengths, because of the effects of electromagnetic coupling. For longitudinal polarization of the incident light, the NFE peaks undergo a red-shift if the interparticle distance is decreased, as shown in Fig. 4.4(b). This result confirms the trend previously observed for the scattering efficiency.

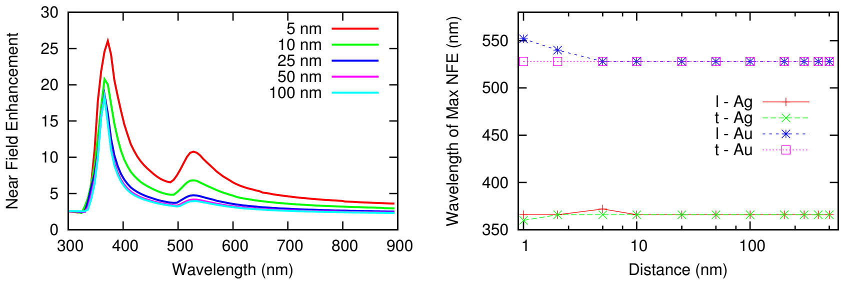

Figure 4.4: (Left) NFE of a symmetric heterodimer with $R = 25$ nm as function of the interparticle edge-to-edge distance, in case of incident light with longitudinal polarization. (Right) NFE peak spectral positions, for both transverse (t) and longitudinal (l) polarizations.

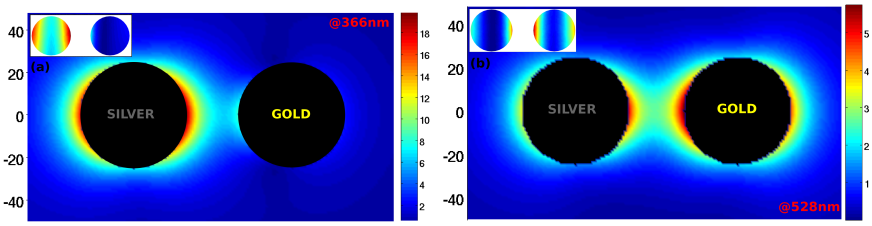

Figure 4.5: NFE pattern in proximity of a symmetric heterodimer with $R = 25$ nm, and on its surfaces (insets). The incident light has longitudinal polarization and wavelength $\lambda = 366$ nm (left) and $\lambda = 528$ nm (right).

These results on the strong near-field coupling in case of incident light with longitudinal polarization are supported by NFE calculations over the particle surfaces and in their proximity, as shown in Fig. 4.5. In particular the panel (a) represents the NFE pattern at the incident wavelength $\lambda = 366$ nm. In this case the Ag particle resonates as if it were isolated. Panel (b) represents the NFE pattern at the incident wavelength $\lambda = 528$ nm, typical of the Au LSPs. In this case the resonance involves also the Ag particle. This circumstance explains the higher NFE with respect to the isolated Au particle.

A similar analysis is conducted for an heterodimer composed by two particles with equal radius $R = 50$ nm. The same remarks of the previous case are valid now, in terms of peak amplitude and position, as plotted in Fig. 4.6(a) and 4.7(a), respectively for the scattering efficiency and NFE with longitudinally polarized incoming field. The spectral positions of the resonance peaks, shown in Fig. 4.6(b) and 4.7(b) for the scattering efficiency and NFE respectively, reveal a modulation for distances comparable with the incident wavelength. This effect is due to the far-field radiative coupling between the two particles compounding the heterodimer.

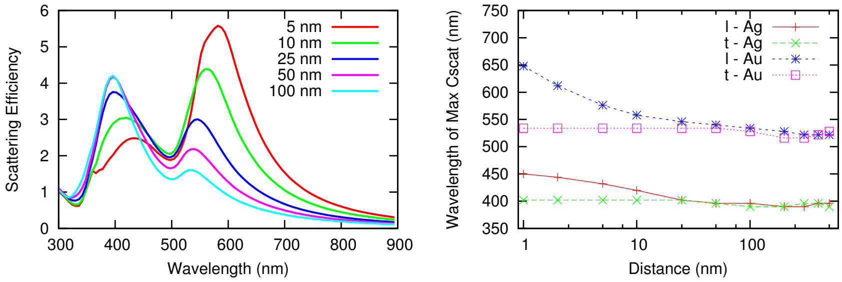

Figure 4.6: (Left) Scattering efficiency of a symmetric heterodimer with $R = 50$ nm as function of the interparticle edge-to-edge distance, in the case of longitudinal polarization. (Right) Spectral position of the scattering peaks, for both transverse (t) and longitudinal (l) polarization.

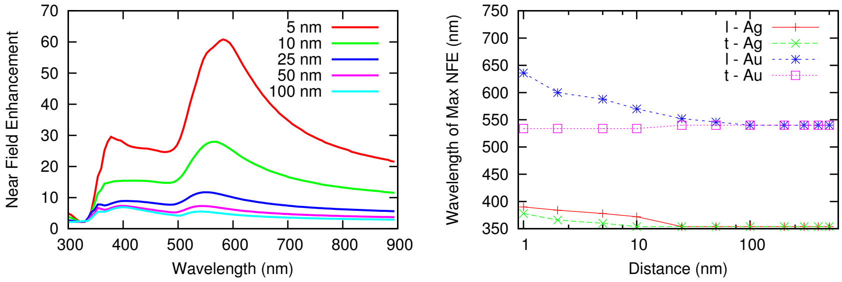

Figure 4.7: (Left) NFE for a symmetric heterodimer with $R = 50$ nm as function of the interparticle edge-to-edge distance, in the case of longitudinal polarization. (Right) Spectral position of the NFE peaks, for both transverse (t) and longitudinal (l) polarization.

As conclusion of this Section, we now illustrate the results of the quasistatic point-dipole approximation to the symmetric heterodimer. From the system of two linear algebraic equations governing the dipole moments, by imposing the Drude model for both metals, we obtain that the eigenfrequencies ω of the heterodimer modes are the roots of the following equation:

$$9\omega^4 - 9i(\nu_{Ag} + \nu_{Au})\omega^3 - [9\nu_{Ag}\nu_{Au} + 3(\omega^2_{p,Ag} + \omega^2_{p,Au})]\omega^2 + \\ 3i(\omega^2_{p,Ag} + \omega^2_{p,Au})\omega + (1-\beta)\omega^2_{p,Ag}\omega^2_{p,Au} = 0$$

where $\beta = \left(\frac{R}{d}\right)^6$ and $\beta = 4\left(\frac{R}{d}\right)^6$ respectively for transverse and longitudinal polarization.

Two roots of the former equation are purely imaginary, while the other two are real and their analytical value is:

$$\omega = \sqrt{\frac{\nu_{Ag}\nu_{Au}}{2} + \frac{\omega^2_{p,Ag} + \omega^2_{p,Au}}{6}}\sqrt{1 \pm \sqrt{1 - \frac{1-\beta}{9}\frac{\omega^2_{p,Ag}\omega^2_{p,Au}}{\left[\frac{\omega^2_{p,Ag}+\omega^2_{p,Au}}{6}\right]^2}}}$$

The eigenfrequencies values as function of the interparticle distance d are plotted in Fig. 4.8, for the two cases of transverse and longitudinal polarization. The point-dipole approximation predicts a red-shift for both transverse and longitudinal modes of the Au particle, and a blue-shift for both transverse and longitudinal modes of the Ag particle.

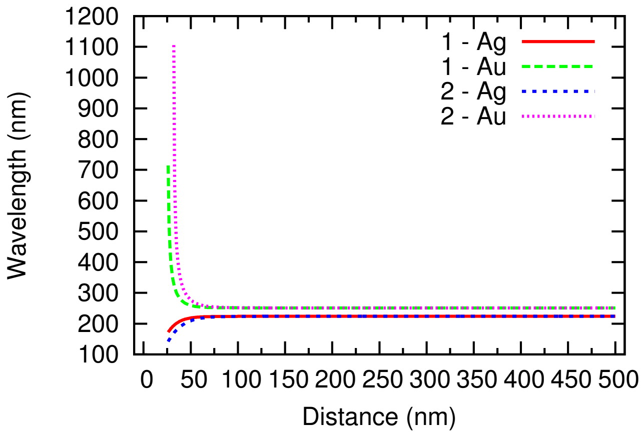

Figure 4.8: Eigenfrequencies of symmetric heterodimers in the quasistatic approximation, as function of the interparticle edge-to-edge distance, for longitudinal and transverse polarization of the incoming field.

4.2 ASYMMETRIC HETERODIMERS

We also investigate the optical response of heterodimers composed by particles with different radii. We fix the radius of the Ag particle at 25 nm, because for this size we observed the higher Ag resonances. For the same reason, we fix the radius of the Au particle to 50 nm, in order to achieve higher scattering and field-enhancement peaks associated also to this particle.

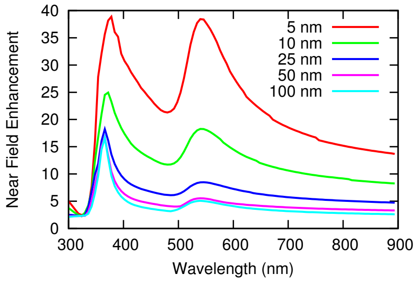

Figure 4.9: NFE for an asymmetric heterodimer composed by particles with radius $R = 25$ nm for Ag and $R = 50$ nm for Au, in case of incoming field with longitudinal polarization, for varying interparticle edge-to-edge distance in the range 5 nm $-$ 100 nm.

The NFE for the asymmetric heterodimer is shown in Fig. 4.9, which differs from the symmetric case in the lower values of enhancement. This is mainly due to higher losses in the Au particle of larger size. The NFE pattern is represented in Fig. 4.10(a) at incident wavelength $\lambda = 366$ nm. The Ag particle still resonates as if it were isolated, and the NFE is only slightly reduced. The NFE pattern for $\lambda = 528$ nm is represented in Fig. 4.10(b). Also in the asymmetric case, the Au particle resonates involving the Ag particle, which in turns boost the LSP by increasing the enhancement value.

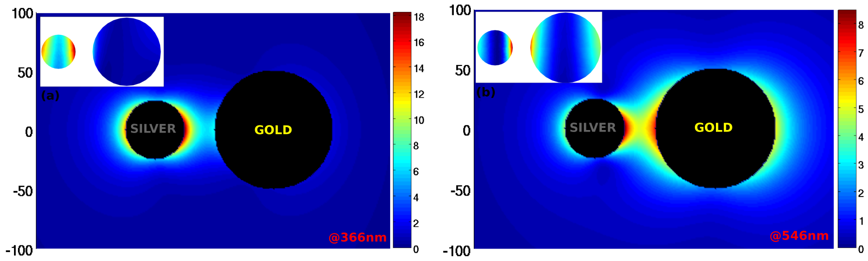

Figure 4.10: NFE pattern for an asymmetric heterodimer composed by particles with radius $R = 25$ nm for Ag and $R = 50$ nm for Au , outside the particles and on their surfaces (insets), in the cases of incoming field with longitudinal polarization, at wavelength $\lambda = 366$ nm (left) and $\lambda = 528$ nm (right).

4.3 ARRAYS OF HETERODIMERS

We conclude this analysis by investigating the optical response of plasmonic heterodimer arrays. The NFE of rectangular arrays of 3x3 heterodimers is shown in Fig. 4.11 in the case of incident light with longitudinal polarization. Panels (a) and (b) are relative to symmetric and asymmetric heterodimers, respectively. The NFE spectra are represented for arrays of different period a, which is defined as the distance between two adjacent particles of the same metal. The distance d between the two particles composing the dimer is fixed to 25 nm, a reasonable length for EBL fabrication technique.

For particles with the same radius $R = 50$ nm, a varies in the range 250 nm − 600 nm. The case $a = 250$ nm (red line) consists of equispaced particles composing linear chains of total length 725 nm. As a result, we observe the rise of a third NFE peak centered at that wavelength, which is due to a photonic resonance along the chain. The case $a = 275$ nm provides the maximum amplitude for the peak corresponding to the Ag particle. As a matter of fact, the radiative coupling between the Ag particles is in resonance for this array period. The maximum in the second peak amplitude occurs for a period $a = 400$ nm, corresponding to a resonances between the Au particles.

For asymmetric dimers (25 nm for Ag and 50 nm for Au), a is varies in the range 200 nm − 500 nm, as shown in 4.11. The case $a = 200$ nm (red line) consists of equispaced particles composing linear chains of total length 575 nm, providing a peak centered at a wavelength of equal value. As before, the peak maxima for Ag and Au peaks can be observed at special array periods, respectively $a = 250$ nm and $a = 400$ nm, due to far-field coupling between particles of the same metal.

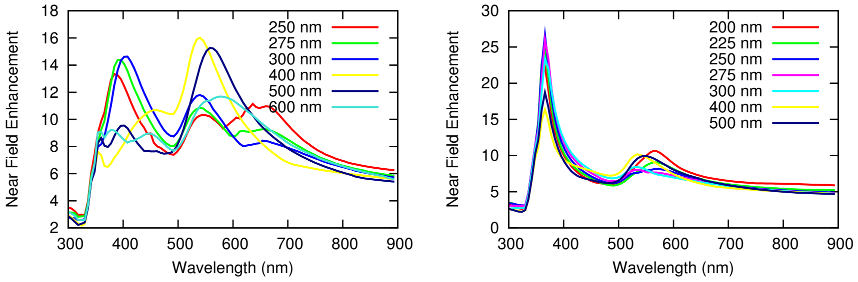

Figure 4.11: NFE for a 3x3 array, in case of incoming field with longitudinal polarization. (Left) Particles with radius $R = 50$ nm for Ag and $R = 50$ nm for Au, for varying array period in the range 250 nm − 600 nm. (Right) Particles with radius $R = 25$ nm for Ag and $R = 50$ nm for Au, for varying array period in the range 200 nm − 500 nm.

These NFE spectral features do not change passing from 3x3 to 7x7 arrays, as it can be observed in Fig. 4.11 and 4.12. In Fig. 4.13 the NFE pattern on particle surfaces is plotted for a 7x7 array composed by particles with the same radius $R = 25$ nm, in the cases of incoming field with longitudinal polarization, at wavelength $\lambda = 366$ nm (a) and $\lambda = 528$ nm (b).

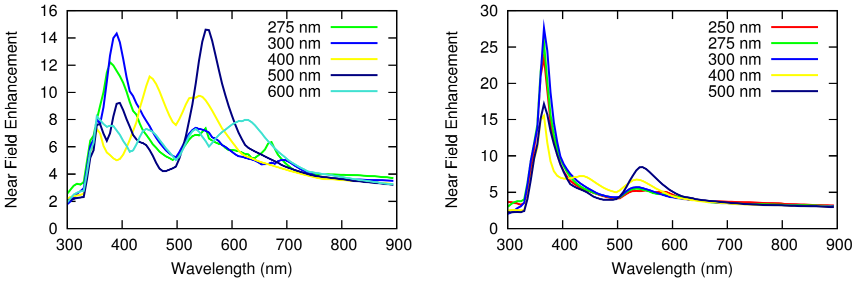

Figure 4.12: NFE for a 7x7 array, in case of incoming field with longitudinal polarization. (Left) Particles with radius $R = 50$ nm for Ag and $R = 50$ nm for Au, for varying array period in the range 250 nm − 600 nm. (Right) Particles with radius $R = 25$ nm for Ag and $R = 50$ nm for Au, for varying array period in the range 200 nm − 500 nm.

4.4 CONCLUSION

In conclusion, in the present Chapter we investigated the optical response of plasmonic heterostructures composed by gold and silver nanoparticles. We demonstrated that the elementary heterodimer block can support hybrid LSPs at two specific spectral positions. This property can be tuned by changing the interparticle separation and the particle size. Moreover, we demonstrated that asymmetric heterodimers can be employed to obtain NFE peaks with equal intensity, both for the gold and the silver wavelengths. Eventually, we demonstrated that these heterostructures can be organized in planar arrays for realizing a plasmonic substrates. The array period is a further parameter to tune the optical response of the investigated heterostructures.

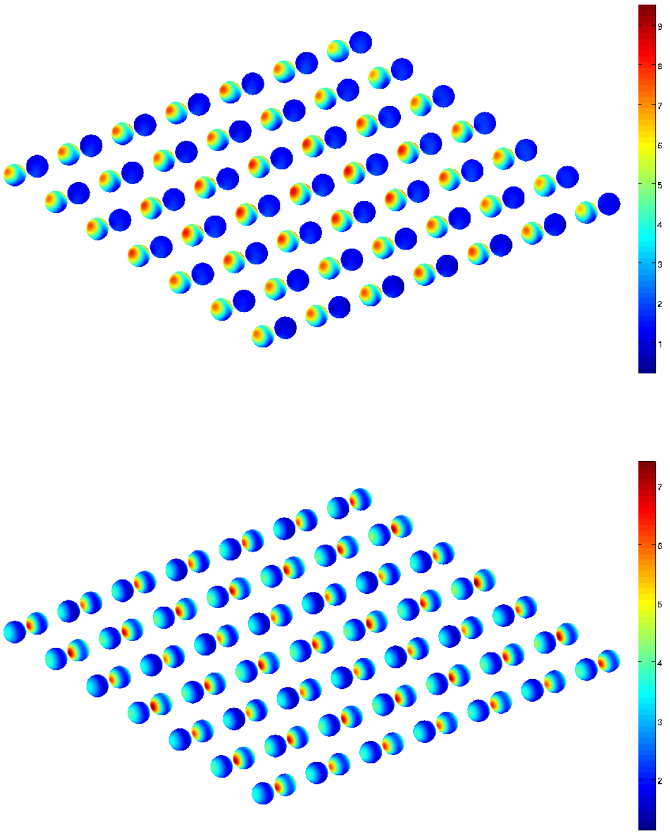

Figure 4.13: NFE pattern for a 7x7 array composed by particles with the same radius r =25 for Ag and Au, in the cases of incoming field with longitudinal polarization, at wavelength $\lambda = 366$ nm (upper panel) and $\lambda = 528$ nm (lower panel).

5

OPTIMIZED NANOLENSES

Nanolenses are nanostructured devices able to efficiently collect an incident radiation and concentrate its power in small regions in their proximity. These novel devices are in some cases able to overcome the diffraction limits of geometrical Optics, concentrating light in spatial regions with smaller size than the incident wavelength, commonly referred to as hot-spots [40, 41]. For this reason, they are called *super-lenses*. Nanolenses are often made of metal nanostructures, for their ability to support SPPs and LSPs. These plasmonic effects allow for the concentration of light in subwavelength regions, as already discussed in Chapter 2.

Plasmonic concentrators of light are playing a key role for the improvement of several devices, such as solar cells [70] , photodetectors [71], optical manipulators [72], modulators [73] thermal emitters [74], SERS substrates [75] , near-field scanning optical microscopes [76] , magnetic recorders [77], and they are also ideal to enhance nonlinear optical effects [78]. Consequently, it is of fundamental importance to design efficient and reproducible plasmonic nanolenses, providing high electric field at defined spatial locations and frequencies.

Several metal nanoparticle configurations have been studied in the last decades for these purposes, and their performance is commonly quantified in term of NFE, defined as:

$$\mathrm{NFE} = \frac{\boldsymbol{E}_{\mathrm{max}}}{\boldsymbol{E}_{\mathrm{inc}}} \tag{5.1}$$

where $\boldsymbol{E}_{\mathrm{inc}}$ is the electric field amplitude of the incident light, and $\boldsymbol{E}_{\mathrm{max}}$ is the maximum electric field amplitude, measured in the hot-spot. A very interesting nanolens has been proposed, consisting of a chain of metal nano-particles with s self-similar geometrical configuration, given by the ratios between the particle sizes and their distance [79]. After that, accurate studies including fully retarded electromagnetic interactions demonstrated large electric field enhancement in silver spheres [80]. More recently, Zou and Schatz [81] highlighted the importance of long-range diffractive coupling in nanoparticle arrays for the enhancement of the electric field in the subwavelength hot-spot of a plasmonic dimer.

However, the use of multi-parametric optimization for the design of nanoplasmonic structures has been very limited so far. In particular, recent studies have focused on the optimization of nanoparticle shapes and geometrical arrangements for the control of plasmonic resonances [82] and broadband field enhancement [83], respectively.

In the present Chapter, we optimize plasmonic nanolenses with high NFE. In particular, we propose a general procedure for the design of plasmonic nanolenses, that combines an optimization method and an electromagnetic solver based on the analytical multiparticle Mie theory, that has been described in Chapter 3. This approach selects the optimal particle arrangements for light concentration, and it also unveils the most general criteria for the engineering of plasmonic nanolenses. As a result, we obtain some general design criteria for plasmonic nanolenses. In particular, we unveil important properties of the interplay between the near-field and the far-field coupling occurring in the interaction of several metal nano-particles [1] .

Eventually, we validate the optimized nanolens configurations by performing SERS experiments, for probing the NFE. These novel nanolens configurations lead to order of ten improvement of Raman enhancement over nanoparticle dimer antennas, and order of one hundred improvement over optimal nanoparticle gratings. A rigorous design of nanoparticle arrays with optimal field enhancement is essential to the engineering of numerous nanoscale optical devices such as plasmon-enhanced biosensors, photodetectors, light sources and more efficient nonlinear optical elements for on chip integration.

---

[1] The figures in the present Section have been adapted with permission from Ref. [85]. Copyright (2012) American Chemical Society.

5.1 GENETIC OPTIMIZATION

In the present Section, we propose a general method for the design of plasmonic nanolenses, based on the combination of an optimization algorithm and an electromagnetic solver. The following nanoparticle properties can be engineered for the efficient design of nanolenses:

1. Shape; it can be the same for each nanoparticle, or different.
2. Size; it can be the same for each nanoparticle, or different.
3. Position; it includes monodimensional (chain), bidimensional (planar arrays) or three-dimensional spatial configurations.
4. Material; it determines the particle electromagnetic dispersion properties.

In general, all the above properties can be considered as degrees of freedom in the optimization process. However, the range in which they can vary is strictly imposed by technological limits. In the proposed optimization approach, several constraints are enforced to guarantee the physical realizability of the targeted nanostructures within the limitations of the available fabrication techniques, such as requiring minimum and maximum particle size or minimum interparticle separation. Several objective functions can be chosen, for instance the most important for plasmonic applications are:

1. NFE at a specific probing point;
2. Average NFE over a spatial region of interest;
3. Scattered power within a prescribed angular cone.

Moreover, the spectral properties of the nanolens are of primary importance, and consequently the selected objective function can be maximized for a single frequency (i. e. narrow band optimization) or for multiple frequencies (i. e. broad band optimization).

In the study presented in this Chapter, our aim is to maximize the NFE at a specific wavelength, by considering a single probing point. This choice responds to the technology requirement of concentrating the incident light power in a subwavelength hot spot. The NFE is evaluated through a full-wave electromagnetic solver based on the multiparticle Mie theory. As a matter of fact, the electromagnetic response of aggregates of spherical particles with different radii can be rigorously treated with the semi-analytical method described in Chapter 3, and based on a multipolar expansion of the scattered field in terms of SVWFs.

In particular, we aim at finding both the radii $\{R_1, \dots, R_N\}$ and the spatial arrangement $\{\boldsymbol{r}_1, \dots, \boldsymbol{r}_N\}$ of an optimized aggregate of N nano-spheres. The nanoparticles can be placed within predetermined boundaries (either one- or two-dimensional) with constraints on the edge-to-edge distance δ between any pair of particles, the minimum R_{min} and maximum R_{max} particle radius, as well as constraints preventing particles from overlapping with the probing point r_0 (even if they can be in contact with it). Both gold and silver nanoparticles have been investigated using experimentally derived dispersion data [38]. The objective function is the NFE at the probing point r_0.

In our study, we impose $\delta = 3$ nm, $R_{min} = 5$ nm as lower size bounds of our search algorithm. Moreover, $R_{max} = 150$ nm has been set as an upper size bound. The particle arrays are illuminated by a linearly polarized plane wave at the plasmonic resonance wavelength, i. e. $\lambda_{Ag} = 370$ nm for silver and $\lambda_{Au} = 535$ nm for gold, propagating orthogonally to the plane of the array. The corresponding refractive index, namely $n_{Ag}(\lambda_{Ag}) = 0.068 - i\ 1.68$ and $n_{Au}(\lambda_{Au}) = 0.52 - i\ 2.28$, has been obtained from experimental data [38]. Eventually, we design a plasmonic array for SERS sensing compatible with practical fabrication constraints, as a proof of concept device to experimentally validate the optimization approach.

The objective function is maximized through a Genetic Algorithm (GA) (or evolutionary algorithm), which is inspired by biological concepts such as natural selection and survival of the fittest. Evolutionary algorithms are among the most efficient methods for treating problems with a large number of unknowns. They also have the valuable property of avoiding local maxima, which is the main disadvantage of deterministic algorithms [84]. In particular, the GA [85] is very well established in radio-frequency antenna engineering [86, 87] and it has found some application in the field of nano-optics [82, 83].

In the framework of the GA, a solution of the optimization problem, usually referred to as an individual, is represented by a binary string, namely a chromosome. Each chromosome is divided into N genes; the j-th gene represents, through an appropriate coding, the j-th degree of freedom of the problem. We choose a Gray coding because it guarantees that two consecutive values of a degree of freedom are represented by genes differing only in one digit. A fitness value is determined for each individual, by means of the electromagnetic solver in our case. We implemented a GA consisting of the following steps:

1. The population, which consists of W individuals, is randomly initialized.

2. The fitness of each individual is evaluated and the selection of the mating pool among the population is performed. The implemented selection criterion is the roulette wheel selection: each wheel's slot is proportional to the individual fitness. Indeed, a fit individual has a better probability of being selected for mating.

3. Once the mating has been performed, the crossover process between two chromosomes takes place. The two mating chromosomes are cut at the same randomly selected point and the resulting strings are swapped between them.

4. In order to prevent the GA from becoming trapped in local mini ma and to preserve the genetic diversity of the population, the chromosomes are subject to mutation. The implemented mutation consists of inverting the value of one bit along the chromosome, with a given probability.

5. Eventually the old generation is removed and replaced by the new individuals, providing that the best individual in the old population is maintained (*elitism*).

The iterative process restarts from step 2. Once the iteration number reaches the maximum value N_{iter}, the GA stops. We have assumed in the present optimization a population $W = 48$ individuals, a number of iterations $N_{iter} = 10000$, and a probability of mutation of $P_m = 0.1$.

5.2 NANOPARTICLE CHAINS

In this Section, we optimize plasmonic nanolenses composed by metal nanoparticles aligned in one direction, i. e. nanoparticle chains. Specifically, we engineer the radii and the positions of particles with their centers constrained to be on the the polarization direction of the incident plane wave, i. e. the x-axis. Our approach consists of optimizing one single particle's size and position, and successively of adding a second particle and optimize it. We iterate this method up to $N = 6$ particles. The optimized particle positions and radii and the corresponding values of NFE are given in Table 5.1. Here we describe the most significant results.

N	$x_{Ag}[nm]$	$R_{Ag}[nm]$	NFE_{Ag}	$x_{Au}[nm]$	$R_{Au}[nm]$	NFE_{Au}
1	36	33	16.2	64	61	4.9
2	-6.5	6.5	248	-29	29	63
3	470	150	301	-491	103	70
4	-431	150	333	511	107	76
5	-215	46	341	1070	99	78
6	250	49	364	-138	45	80

Table 5.1: Particle coordinates, radii, and NFE for silver and gold linear nanolenses

$N = 1$. For the single isolated particle, we find the optimized solution consisting of the particle in direct contact with the probing point r_0, i. e. the maximum of NFE is on the particle surface. The optimized radius turns out to be $R_{Au} = 57\ nm$ for the gold and $R_{Ag} = 26.6\ nm$ for the silver. With these sizes, the coupling of the incoming radiation into the particle dipolar mode is maximized. It is worth to notice that this goal is achieved by balancing two different needs. First, high-order modes and total losses have to be minimized, hence the particle has to be small. Second, the particle's dipole moment has to be maximized. It is proportional to the particle volume, and therefore the size has to be large enough. We also notice that the ratio between the optimized radius and the wavelength turns out to be of the same order of magnitude for both materials, this being a clear fingerprint of the quasi-static character of the electromagnetic interaction.

$N = 2$. The optimum solution for both silver and gold is an asymmetric dimer, i. e. the particles have two different radii, with an edge-to-edge spacing as small as allowed by the constraint $\delta = 3\ nm$. An hot-spot is located in the dimer gap, as shown in Fig. 5.1(a) and (b). Since the dimer features high ratio between the radii of the two particles, that is $R_1/R_2 = 2.1$ for gold and $R_1/R_2 = 5.1$ for silver, the local field around the larger particle is only weakly modified by the smaller one, and the resulting NFE is approximately the product of the enhancement factors of the two isolated particles, in agreement with the results of Ref. [79].

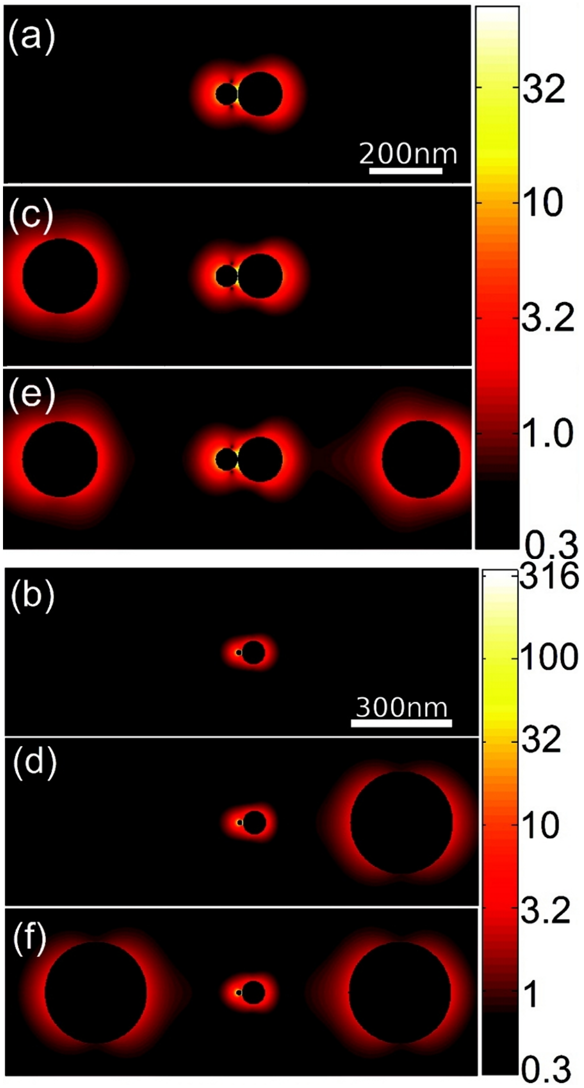

Figure 5.1: Electric field magnitude on the equatorial plane of the optimized linear nanolenses composed of (a,b) N = 2, (c,d) N = 3, and (e,f) N = 4 spheres for Au and Ag, respectively. The obtained values of field enhancement at the probing point are (a) 63, (b) 248, (c) 70, (d) 301, 76 (e), and (f) 333. The color maps are in log scale.

$N = 3$. The GA places the center of the third particle such that the in-phase coupling with the dimer is maximized at the probing point. The distance between the third particle and the central dimer produces an in-phase radiative coupling with the external excitation in each particle of the dimer, as well-depicted in Fig. 5.2. This Figure plots the phase difference between the incident electric field (polarized along the x-axis) and the x-component of the electric field scattered by the third particle as if it were isolated, on the $z = 0$ plane, for gold (a) and silver (b). For both Au and Ag particles, we notice that the third particle radiates an electric field whose x-component is in-phase with the external field in the proximity of particles 1 and 2. Therefore, the central dimer experiences a total incident field that is the in-phase superposition of the external field and the field radiated by the third particle. Furthermore, we observe in Figure 5.1(c) and (d) that the third particle in the linear array assumes the maximum allowed radius in order to maximize the radiative coupling within the limits of inherent material losses.

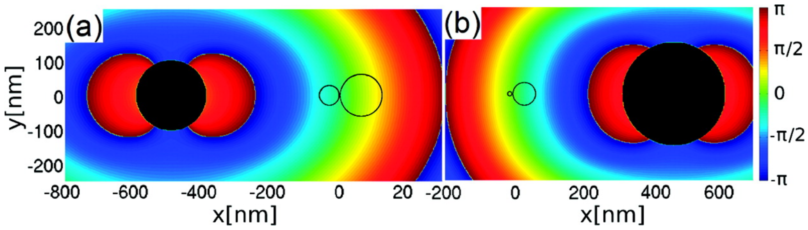

Figure 5.2: Phase difference between the incident electric field (oriented along the x-axis) and the x-component of the electric field scattered by the 3rd particle in the absence of the first two particles on the $z = 0$ plane, for gold (a) and silver (b) particles. The contours of the 1st and 2nd particles have been also plotted for convenience. The phase is shown in radiant.

$N = 4$ The GA places the fourth particle on the opposite side, symmetrically with respect to the third in order to further boost radiative coupling, as is shown in Fig. 5.1, for both gold and silver. However, adding further particles to the linear chain causes a saturation of the field intensity value and additional particles only contribute with a negligible increase to the NFE, as can be seen in Table 5.1.

5.3 PLANAR NANOLENSES

In the present Section, we apply the GA to the design of planar arrays of gold and silver nanoparticles, excited by a linearly polarized plane wave propagating orthogonally to the array plane. In this case, the design is carried out by keeping all the particle radii fixed to $R_0 = 50$ nm, and only their positions are optimized. In particular, the particles can be placed within a square of length $L = 2$ µm. The resulting coordinates are listed in Table 5.2. In the following, we will describe the most significant cases.

N	x_{Ag}[nm]	y_{Ag}[nm]	NFE_{Ag}	x_{Au}[nm]	y_{Au}[nm]	NFE_{Au}
1	-50	0	-	-50	0	-
2	53	0	120	53	0	62
3	124	-215	-	-55	-359	-
4	-134	-205	-	58	-359	-
5	123	215	-	-52	370	-
6	-133	205	234	61	370	87
7	326	0	-	200	394	-
8	-332	0	276	-191	393	-
9	-180	-550	-	183	-392	-
10	123	-550	-	-180	-390	98
11	-160	540	-	56	-870	-
12	144	540	306	-56	-870	-
13	-	-	-	56	870	-
14	-	-	-	-56	870	107

Table 5.2: Particle coordinates and NFE for silver and gold planar nanolenses with fixed radius.

In agreement with the previous Section, the optimized configuration is a dimer aligned along the polarization direction of the incident light, with shortest edge-to-edge separation, as shown in Fig. 5.3(a) and 5.3(e), for gold and silver respectively.

The case of $N = 6$ for gold is shown in Fig. 5.3(b). It turns out that the particles assemble to form dimers, placed symmetrically with respect to the probing point along the vertical direction. In such a configuration, the particles provide a radiative contribution in-phase with the external excitation, in correspondence of the central dimer. For the case of silver, shown in Fig. 5.3(f), the radiative contribution is equally significant. However, in this case individual particles are placed in a circumference of radius $R_C = 250$ nm centered at r_0. In order to understand this optimized configuration, it is convenient to remind that two electric dipoles lying on a circle, radiate electromag-

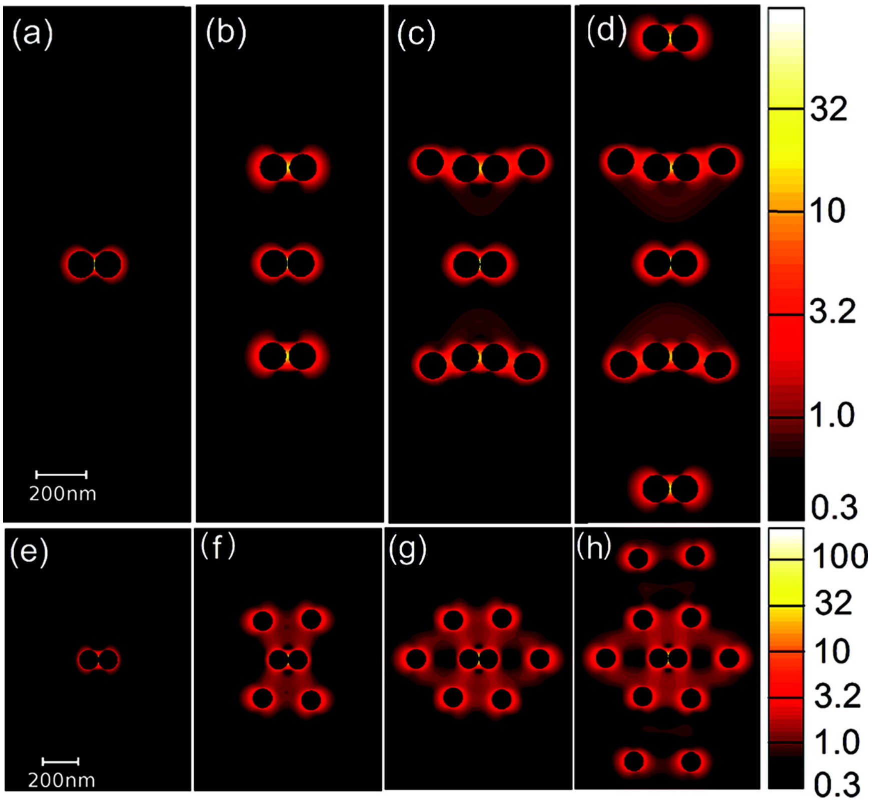

Figure 5.3: Electric field magnitude on the equatorial plane of planar nanolenses composed of (a) $N = 2$, (b) $N = 6$, (c) $N = 10$, and (d) $N = 14$ Au particles and by (e) $N = 2$, (f) $N = 6$, (g) $N = 8$, and (h) $N = 12$ Ag particles. The color maps are in log scale.

netic fields with the same phase at the circle center if they are excited by the same time-harmonic field. Also the radius R_C is optimized to achieve an in-phase coupling between the fields radiated by these particles and the external excitation at the central dimer. Furthermore, the particles are not randomly placed along this circle; the distance between two neighbors is approximately equal to the radius R_C of the circle. As a result, the optimization has also maximized the in phase coupling among the external particles.

Similar results occur in the case $N = 10$ for gold, as shown in Fig. 5.3(c) and in the case $N = 8$ for silver, as shown in Fig. 5.3(g).

In conclusion, this analysis demonstrated that, in order to maximize the radiative contribution in metal particle nanolenses, the fundamental units are the isolated particle in the case of silver and the dimer for gold. This difference is due to the fact that the radiative contribution to the localized near field of an isolated silver particle is much greater than an equivalent size gold particle. Therefore two particles are needed for gold. However, in both cases the distance between the radiative units and the probing point r_0 matches the external field phase at the central dimer's position for the optimization wavelength.

5.4 EXPERIMENTAL VALIDATION

In this Section, we experimentally validate the results of the optimization method previously described. In particular, we design a SERS substrate to increase the Raman scattering signals (see Appendix A.7), as a proof of concept to demonstrate the effectiveness of the optimized nanolenses. Typical SERS substrates are random aggregates of particles [88], periodic gratings [89], dimers [90, 91, 92, 93], bowties [94, 95], deterministic aperiodic arrays [96, 97], or nanoparticle clusters [98, 99], to name just a few possible geometries. Raman enhancements have been shown to scale to the fourth power of local electromagnetic fields [90]:

$$I_{SERS} \propto |E(\lambda_{ex})|^2 |E(\lambda_s)|^2 , \tag{5.2}$$

where λ_{ex} and λ_s are the pump and the Stokes-shifted wavelengths, respectively. Consequently, SERS represents a valid experimental method to determine the NFE of plasmonic substrates.

5.4.1 *Multi-objective optimization*

In order to design a SERS substrate, we performed a multi-objective optimization, i. e. the NFE at the probing point has been simultaneously maximized at the two wavelengths $\lambda_{ex} = 785$ nm and $\lambda_S = 858$ nm, corresponding to the laser pump and the Stokes peak of a pMA molecule, as described with more details in the next. In this optimization process, the gold nanoparticles can be placed within a square of $L = 2$ µm edge, and the minimum allowed edge-to-edge distance between them is $\delta = 25$ nm. The radius is optimized in the interval $[50 \text{ nm}, 150 \text{ nm}]$, as convenient for the EBL fabrication constraints.

N	x[nm]	y[nm]	R	N	x[nm]	y[nm]	R
1	-97	0	72	9	-260	-1000	125
2	75	0	75	10	250	-1000	125
3	-230	460	125	11	0	380	70
4	206	460	125	12	0	175	70
5	-230	-460	125	13	0	-380	70
6	206	-460	125	14	0	-175	70
7	-260	1000	125	15	631	0	125
8	250	1000	125	16	-650	0	125

Table 5.3: Particle coordinates and radii of the planar substrate optimized for SERS.

However, a SERS device with arbitrarily shaped particles over a substrate cannot be modeled by means of the multiparticle Mie theory. Consequently, we use the GA approach to obtain an initial solution, and then it is refined by using a Finite Difference Time Domain (FDTD) solver. In this refinement step, all the nanoparticles are assumed to be cylinders with a height of 30 nm, that it has been found optimal for near-infrared sensing [96, 97], and they are on top of a glass substrate of refractive index $n = 1.45$. The resulting particle coordinates are listed in Table 5.3, for a number of particles N up to 8.

The calculated values of the field enhancement intensity NFE^2 are shown in Fig. 5.4(a) for $\lambda_{ex} = 785$ nm, as function of N. As more particles are added to the substrate, the intensity boosting begins to saturate for $N = 14$. The optimal configuration for $N = 16$ is schematically represented in the inset. This analysis confirms that the field intensity increases dramatically with N, due to the radiative contribution introduced by the additional particles.

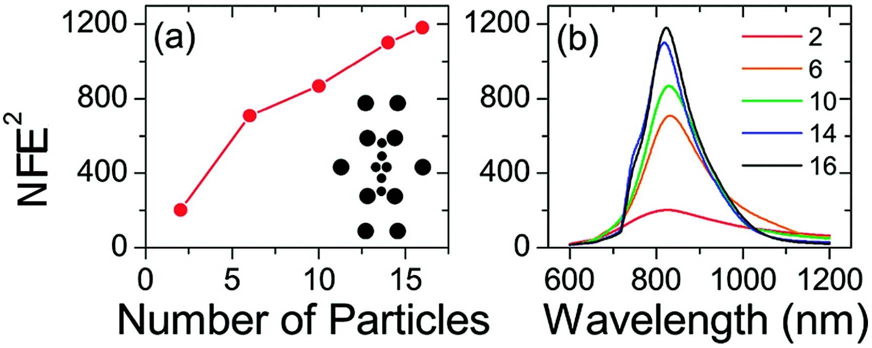

Figure 5.4: (a) Field enhancement intensity of the optimized SERS substrate at $\lambda_{ex} = 785$ nm as function of the number of particles. The optimal configuration is represented in the inset. (b) Field enhancement intensity spectra, parametrized for the number of particles.

The NFE spectra are represented in panel Fig. 5.4(b), showing that the enhancement peak is preserved at the center of the prescribed values of the optimization (the pump and Stokes-shifted wavelengths of pMA), for any value of N. These spectra confirm that, by optimizing the focusing of the radiative contribution of large Au nanoparticles into the central dimer, we are able to increase the values of near-field enhancement by a factor of 6 with respect to the isolated optimized dimer.

5.4.2 *Sample fabrication and SEM characterization*

We fabricated the optimized array with $N = 16$ and repeated it in a periodic tiling on the chip. The periodic tiling was accomplished by stepping-and-repeating the genetic pattern as a base, overlapping the six outer particles. We also fabricated reference arrays of dimers and periodic gratings with optimized particle spacing as a reference. All these structures exhibit strong plasmonic resonance in an overlapping spectral region. All of the patterns were fabricated with the EBL process described in Appendix A.8, using a Zeiss SUPRA 40VP SEM equipped with a Raith beam blanker.

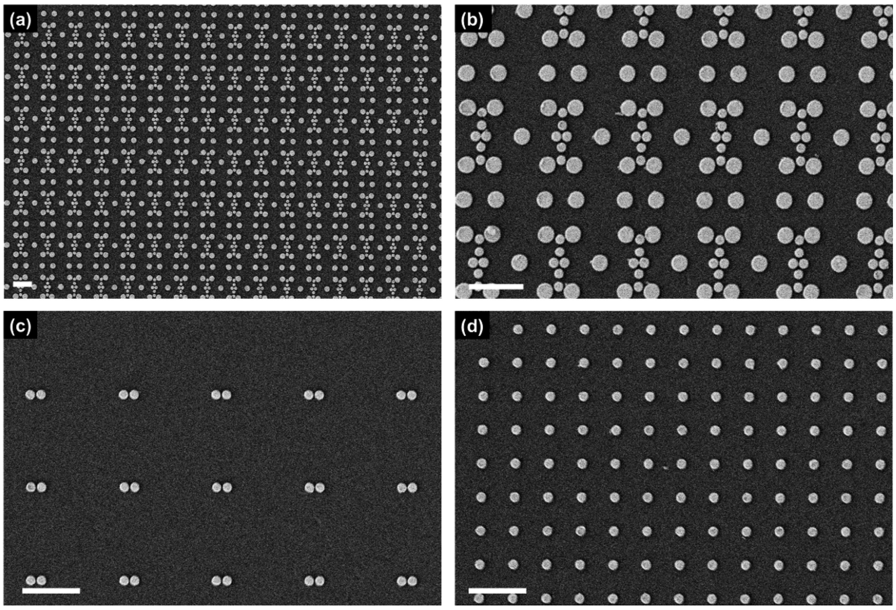

Figure 5.5: SEM micrographs of SERS substrates. Genetically optimized array (a) and its close-up (b). Dimers (c) (left particle diameter 72.5 nm, right particle diameter 74 nm) spaced 1.5μm apart. Monomers (d) with 150 nm diameter in a 540 nm lattice. All scale bars correspond to 1 μm.

The representative Scanning Electron Microscopy (SEM) images of the fabricated arrays are shown in Fig. 5.5. We show the optimized nanoarray in panel (a), and a close-up in panel (b), confirming the central dimer separation of 25 nm. We show in panel (c) dimers with the same diameters as the central dimer of the optimized array, spaced 1.5 μm apart to avoid diffractive coupling. In panel (d) we show a periodic array designed to enhance near-fields at 785 nm, with a particle diameter of 150 nm and lattice constant of 540 nm. The scale bars all correspond to 1 μm. These SEM micrographs show almost ideal agreement with our design parameters over a large pattern area. Each pattern was spaced by 100 μm to avoid undesired electromagnetic coupling.

5.4.3 *SERS characterization*

In this Section, a rigorous analysis of the near-field properties of genetically optimized, dimer and periodic plasmonic arrays is performed. The calculated near-field intensity supported by each pattern is shown in Fig. 5.6(a) as function of the wavelength. The incident light is a plane wave polarized along the dimer axis. It is clearly shown that the maximum near-field spectra of the optimized array is greatly enhanced over isolated dimers and the periodic arrays. The optimized array supports the strongest fields due to the optimal interplay between the near-field coupling at the gap of the central dimer and the radiative contribution of the surrounding particles.

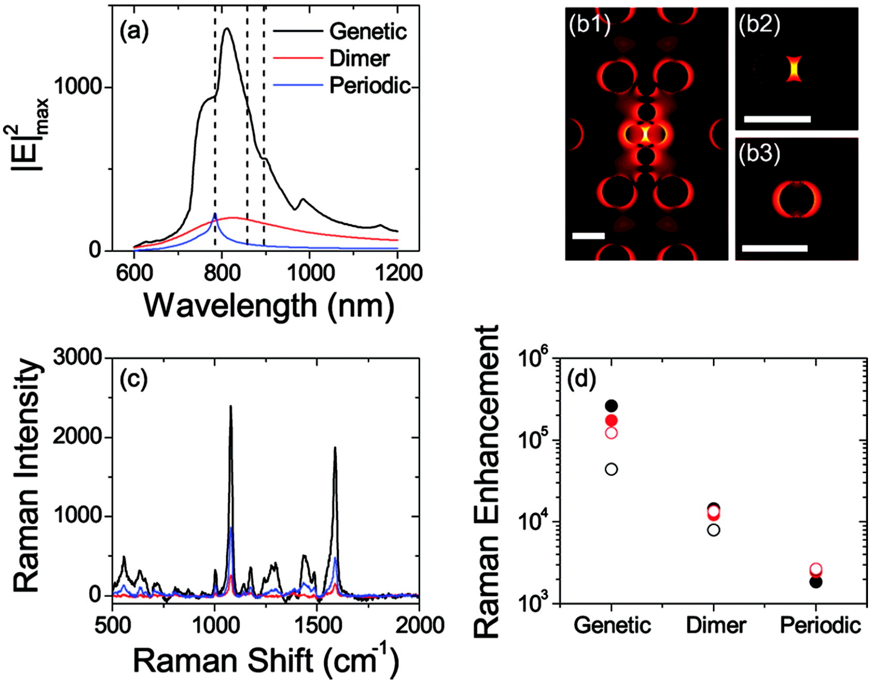

Figure 5.6: Experimental and theoretical analysis of the near-field properties: (a) Maximum near-field intensity spectra of the optimized array, dimers, and a periodic array. Dashed vertical lines indicate the pump wavelength $\lambda_{ex} = 785$ nm, and the wavelengths of the two Stokes modes 1077 cm^{-1} and 1590 cm^{-1}. Near-field intensity distribution in logarithmic scale on the equatorial plane at λ_{ex} of the (b1) optimized array, (b2) dimer, and (b3) periodic grating. The scale bars correspond to 300 nm. (c) Measured Raman spectra of the optimized, dimer and periodic arrays. (d) Raman enhancements for the 1077 cm^{-1} (red) and 1590 cm^{-1} (black) modes of pMA, as measured (open circles) and calculated (solid circles).

The spatial distributions of the calculated near-field intensity are shown (in logarithmic scale) in Fig. 5.6(b1) for the optimized array, 5.6(b2) for the individual dimer, and 5.6(b3) for the periodic array at 785 nm, normalized to their maximum field values, with the scale bars corresponding to 300 nm. The genetic patterns exhibit the strongest near-fields in the gap between the two dimer particles, while rather weak near-fields are present around the other particles.

In order to experimentally validate our design procedure, we measured the SERS signal as described in Appendix A.7. The intensity of the raw Raman signals is shown for comparison in Fig. 5.6(c) for the optimized array, dimers, and periodic array. The genetic pattern shows the strongest Raman signals, while the periodic array has a larger intensity at all Raman modes than the dimers. It is important to notice that there is also more gold in the periodic structure, which will be corrected for below. We only consider the two dominant Stokes modes, i. e. the Raman shifts 1077 cm^{-1} and 1590 cm^{-1}.

It is worth to notice that a normalization to the active area of the specific SERS pattern is required to obtain a correct estimation of the NFE. In order to take into account the different amount of Au which contribute to the Raman signal in the different arrays, we calculate Raman enhancement values for each pattern, as previously described in the literature [88, 100]. Unlike periodic and dimer structures, where the field enhancement is uniformly distributed around all the particles within the array, in the case of the genetically optimized pattern only the central dimer contributes to the SERS signal. All other particles in the pattern support very weak electromagnetic fields and would lead to an underestimation of our Raman enhancement. Therefore we have considered only the Au surface area of the central dimer in our calculations of the number of excited pMA molecules for the optimized array.

By performing the Raman enhancement calculations on the 1077 cm^{-1} (black circles) and 1590 cm^{-1} (red circles) modes on each sample type, we show in Fig. 5.6(d) the corresponding measured Raman enhancement factors for each geometry (open circles) and a comparison with our FDTD calculations (solid circles). Since unpolarized light was used to experimentally excite the Raman spectrum, in our FDTD calculations of Raman enhancement we considered the enhancement averaged over two orthogonal polarization states. The FDTD calculations predict a logarithmic scaling of enhancement factors for each geometry, which is followed by the experimental data. The optimized array exhibits a calculated Raman enhancement of 10^5, followed by the dimers with 10^4 and the periodic grating with 10^3 enhancement. Experimentally, the periodic structure exhibits an enhancement factor in the low 10^3 range for both modes, which very closely follows our theoretical prediction. The 1077 cm^{-1} and 1590 cm^{-1} modes of the dimers were measured to have a Raman enhancement of $7.9\mathrm{x}10^3$ and $1.3\mathrm{x}10^4$. The measured enhancement factors of the optimized array are $4.4\mathrm{x}10^4$ and $1.2\mathrm{x}10^5$ for the two Raman modes. All these values are in reasonably good agreement with the FDTD calculations.

The data shown in Fig. 5.6 demonstrate the effectiveness of the GA optimization approach and demonstrate the essential role played by the radiative coupling to enhance near-field strength in the central dimer region of the genetically optimized structures with a large improvement of Raman signals over patterns optimized using conventional dimer or periodic grating geometries.

5.5 CONCLUSION

In this Chapter, we have shown that we can achieve order of ten improvement over dimers and order of one hundred improvement over periodic gratings in Raman enhancement by genetically optimizing a nanoparticle array. This is essentially accomplished by an optimum interplay between the plasmonic near-field interaction in a dimer and the far-field radiative contributions of the surrounding particles placed at genetically optimized locations.

We have shown that the design of metallic nanoparticles clusters for obtaining a very large field enhancement can be performed using the basic paradigm of engineering, namely the optimization of a well-defined objective function. The investigated scenarios demonstrate that two different mechanisms are at the origin of high field enhancement and need to be simultaneously optimized: the near-field coupling between closely spaced particles and the far-field radiative coupling of the surrounding particles. We have unveiled general rules behind the maximization of the radiative coupling. In particular, the building blocks for best electric field enhancement should be isolated particles and dimers for Ag and Au aggregates respectively, and the distances between these building blocks should be optimized to obtain constructive interference with the external field excitation at the probing point. Our optimization approach is validated by SERS measurements performed on fabricated devices using pMA monolayers, demonstrating that genetically optimized arrays lead to order of ten improvement over dimers, and order of one hundred improvement over periodic gratings in Raman enhancement. A careful design of nanoparticle light concentrators can have a large impact in numerous nano-optics applications including solar cells, optical manipulators, plasmon enhanced photodetectors, modulators, and nonlinear optical devices.

Part III

HARMONIC GENERATION IN METALS AT NANOSCALE

Nonlinear phenomena in metal nanostructures are gathering much attention due to their potential application in novel components for integrated optics [101, 102, 103, 104, 105]. Metal nanoparticles have been employed for decades to enhance the efficiency of optical processes, including Raman scattering, fluorescence, and multiphoton absorption because they support LSPs. When LSPs are resonantly excited, the local electromagnetic field is significantly enhanced in the particle, enabling the generation of nonlinear optical effects, such as harmonic generation, at relatively low excitation powers. This enables strong nonlinear optical effects at relatively low excitation powers, such as harmonic generation and the Kerr effect. In particular, the Second Harmonic (SH) generation is a nonlinear optical process in which a medium excited by two photons at a fundamental frequency ω_0 emits one photon at twice that frequency $2\omega_0$. SH generation from metal nanostructures provides a powerful tool for probing physical and chemical properties of material surfaces [106, 107].

As already discussed in Chapter 2, the SH radiation from metal nanostructures originates from two contributions, the bulk and the surface. In noble metal, the local-bulk source is absent because of the material centrosymmetry, and only the nonlocal-bulk contribution needs to be considered [108]. On the contrary, the local-surface contribution to SH radiation is allowed due to the symmetry breaking at the interface with the embedding medium [109, 110]. The magnitudes of the nonlocal-bulk and surface SH contributions depend on the shape of the nanoparticle and on the optical properties of the metal at the fundamental and second-harmonic frequencies [55, 56, 57, 58, 59, 60, 111, 112].

Several theoretical approaches have been proposed in the last two decades, for modeling second-order nonlinear effects from metal nanostructures. In 1999, Dadap *et al.* studied the SH radiation generated from the surface of a sphere in the Rayleigh regime, i. e. if the particle radius R is much smaller than the wavelength of the incident light λ [110], as already discussed in Chapter 3. It is shown that the leading-order contributions to SH radiation arise from the electric-dipole $\mathbf{p}^{(2\omega)}$ and the electric-quadrupole $\overleftrightarrow{\mathbf{Q}}^{(2\omega)}$ moments, and the main selection rules for the SH scattering from a sphere are outlined. In Refs. [113] and [61], the Rayleigh limit is analyzed by taking into account both the bulk and the surfaces polarization sources, showing that the SH field is radiated by an effective electric dipole moment $\mathbf{p}_{\mathrm{eff}}^{(2\omega)}(\hat{\mathbf{r}}) \cong \mathbf{p}^{(2\omega)} + i k_0 \overleftrightarrow{\mathbf{Q}}^{(2\omega)} \hat{\mathbf{r}}/3$ (the SH magnetic dipole emission is forbidden because of the axial symmetry of the system). In the Rayleigh limit, both the nonlocal-bulk and the surface SH sources contribute to the induced electric dipole moment, while only the local surface sources contribute to the induced electric quadrupole moment. The presence of distinct SH sources with their own radiation patterns causes the SH Rayleigh scattering process to differ significantly from the linear Rayleigh scattering. In particular, the theory predicts the absence of the SH signal in the forward direction and the $(k_0R)^6$ scaling of the SH scattering cross-section.

The SH Rayleigh scattering model is inaccurate if the particle size is comparable with the wavelength, because the contributions of SH multipolar orders higher than 2 are not negligible. A full-wave analysis of the SH scattering from spherical particles of arbitrary size is developed in Ref. [114], but only the surface SH source was taken into account. Moreover, the enforced boundary conditions are incorrect, [108] resulting in zero SH radiation from the radial component of the source. Recently, a full wave theory of the SH radiation generated by a chain of parallel infinitely long cylinders, including both the bulk and surface nonlinear sources, has been developed in Ref. [104]. A full-wave theory of the SH radiation generated in three-dimensional structures consisting of metal spheres made of centrosymmetric materials has been proposed in Ref. [115], but here again the treatment is limited to the surface source. A full-wave analysis of the SH scattering from particle of arbitrary shape can be numerically performed by using numerical integral methods. In particular, the Surface Integral Equation (SIE) and Volume Integral Equation (VIE) approaches have been developed and used to calculate the SH response of metal nanoantennas [116, 55].

THE ANALYTICAL SOLUTION TO THE PROBLEM OF SH SCATTERING FROM A SPHERICAL PARTICLE MADE OF NOBLE METAL WILL BE PRESENTED IN THE NEXT CHAPTER, AS FUNDAMENTAL PART OF THE PRESENT THESIS. FOR THE FIRST TIME, WE CONSIDER ALL THE RELEVANT SOURCES TO THE SH GENERATION PROCESS, NAMELY THE NONLOCAL BULK AND THE LOCAL SURFACE.

6

SECOND-HARMONIC MIE SCATTERING

In this Chapter, we present a full-wave analytical solution for the problem of second-harmonic generation from spherical particles made of lossy centrosymmetric materials. Both the bulk and surface SH sources contribute significantly to the SH scattering response of a spherical nanoparticle, as already demonstrated in approximated analytical models developed to describe the SH generation from noble metal nanostructures with simple geometries, such as spheres and cylinders. Therefore, both the local-surface and nonlocal-bulk nonlinear sources are included in the generation process by means of an effective nonlinear polarization, under the undepleted-pump approximation.

The solution is derived in the framework of the Mie theory by expanding the pump field, the non-linear sources and the second-harmonic fields in series of SVWFs. We use a spherical coordinate system (O, r, θ, ϕ) with the origin O in the center of the sphere, as in Fig. 6.1(a); we denote with $(\hat{\boldsymbol{r}}, \hat{\boldsymbol{\theta}}, \hat{\boldsymbol{\phi}})$ the unit vectors of the spherical coordinate system. The domain of the electromagnetic field is the entire space $\mathbb{R}^3$, divided into the interior part of the metal domain $\dot{\Omega}_i$, the embedding medium $\dot{\Omega}_e$ and the metal surface Σ. The surface Σ is oriented in such a way that its normal $\hat{\mathbf{n}}$ points outward, $\hat{\mathbf{n}} = \hat{\mathbf{r}}|_\Sigma$.

We apply this solution to study the second-harmonic generation properties of noble metal nano-spheres as function of the polarization, the pump wavelength and the particle size.

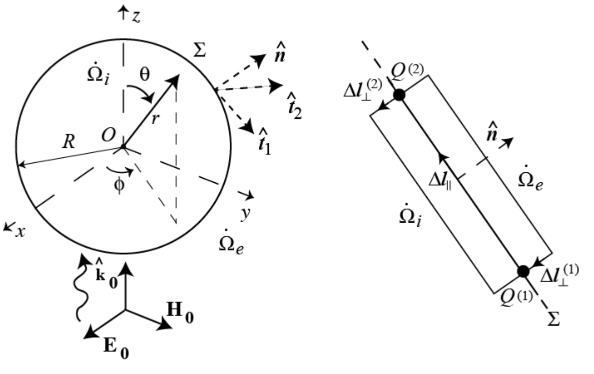

(a) (b)

Figure 6.1: (a) Scheme of the spherical particle and coordinate system (O, r, θ, ϕ). (b) Elementary closed curve Δl across the *selvedge region* at the particle boundary.

6.1 SOURCES OF SECOND-HARMONIC RADIATION IN METALS

The SH sources in metal nanoparticles can be represented by an effective nonlinear polarization induced by the electromagnetic field at the fundamental frequency ω. As already introduced in Chapter 2, the bulk contribution $\mathbf{P}_b^{(2\omega)}$ to the nonlinear polarization is of the form [48]:

$$\begin{aligned}\mathbf{P}_b^{(2\omega)} =& \varepsilon_0\, \beta \mathbf{E}^{(\omega)} \nabla \cdot \mathbf{E}^{(\omega)} + \varepsilon_0\, \gamma \nabla \left(\mathbf{E}^{(\omega)} \cdot \mathbf{E}^{(\omega)}\right) + \\ & \varepsilon_0\, \delta' \left(\mathbf{E}^{(\omega)} \cdot \nabla\right) \mathbf{E}^{(\omega)} \qquad \text{in } \Omega_i\,,\end{aligned} \tag{6.1}$$

where β, γ and δ' are material parameters, ε_0 is the vacuum permittivity, $\boldsymbol{E}^{(\omega)}$ is the electric field at the fundamental frequency and Ω_i denotes the region occupied by the particle. Due to the homogeneity of the material we also have $\nabla \cdot \boldsymbol{E}^{(\omega)} = 0$ in Ω_i, therefore the first term on the right hand side of Eq. (6.1) vanishes and the expression of $\mathbf{P}_b^{(2\omega)}$ reduces to:

$$\mathbf{P}_b^{(2\omega)} = \varepsilon_0\, \gamma \nabla \left(\mathbf{E}^{(\omega)} \cdot \mathbf{E}^{(\omega)}\right) + \varepsilon_0\, \delta' \left(\mathbf{E}^{(\omega)} \cdot \nabla\right) \mathbf{E}^{(\omega)}. \tag{6.2}$$

The surface contribution $\mathbf{P}_s^{(2\omega)}$ can be expressed in the form [108]:

$$\mathbf{P}_s^{(2\omega)} = \varepsilon_0\, \overset{\leftrightarrow}{\chi}_s^{(2\omega)} : \mathbf{E}^{(\omega)} \mathbf{E}^{(\omega)} \Big|_{\Sigma_i} \quad \text{on } \Sigma\,, \tag{6.3}$$

where $\overset{\leftrightarrow}{\chi}_s^{(2\omega)}$ is the second-order surface nonlinear susceptibility tensor of the metal, and Σ denotes the particle boundary. The normal component of $\boldsymbol{E}^{(\omega)}$ is evaluated on the internal page of Σ, which we have indicated with Σ_i; there is no ambiguity relevant to the tangential components of $\boldsymbol{E}^{(\omega)}$ because they are continuous across Σ. Since the nanoparticle surface possesses isotropic symmetry with a mirror plane perpendicular to it, the tensor $\overset{\leftrightarrow}{\chi}_s^{(2\omega)}$ has only three nonvanishing and independent elements, $\chi_{\perp\perp\perp}$, $\chi_{\perp\parallel\parallel}$ and $\chi_{\parallel\perp\parallel} = \chi_{\parallel\parallel\perp}$, where $\perp$ and $\parallel$ refer to the orthogonal and tangential components to the particle surface.[108] Therefore Eq. (6.3) reduces to:

$$\begin{aligned}\mathbf{P}_s^{(2\omega)} \cong \varepsilon_0\, [&\chi_{\perp\perp\perp} \hat{\mathbf{n}}\hat{\mathbf{n}}\hat{\mathbf{n}} + \chi_{\perp\parallel\parallel} \left(\hat{\mathbf{n}}\hat{\mathbf{t}}_1\hat{\mathbf{t}}_1 + \hat{\mathbf{n}}\hat{\mathbf{t}}_2\hat{\mathbf{t}}_2\right) + \\ & \chi_{\parallel\perp\parallel} \left(\hat{\mathbf{t}}_1\hat{\mathbf{n}}\hat{\mathbf{t}}_1 + \hat{\mathbf{t}}_2\hat{\mathbf{n}}\hat{\mathbf{t}}_2\right)] : \mathbf{E}^{(\omega)} \mathbf{E}^{(\omega)}\,,\end{aligned} \tag{6.4}$$

where $\hat{\mathbf{n}}$ is the normal to the particle surface pointing outward and $\hat{\mathbf{t}}_1$,$\hat{\mathbf{t}}_2$ are two orthonormal vectors defining the plane tangent to the particle surface, such that $(\hat{\mathbf{n}}, \hat{\mathbf{t}}_1, \hat{\mathbf{t}}_2)$ is a counterclockwise triplet.

It is interesting to note that, although the the relation between $\mathbf{P}_s^{(2\omega)}$ and $\mathbf{E}^{(\omega)}$ is of local character, the contribution of the normal component $(\mathbf{P}_s^{(2\omega)} \cdot \hat{\mathbf{n}})$ to the SH radiation depends on the surface gradient $\nabla_S (\mathbf{P}_s^{(2\omega)} \cdot \hat{\mathbf{n}})$. In fact in the selvedge region (Fig. 6.1b) at the metal-vacuum interface, there is a volumetric current density:

$$\mathbf{J}_{s\perp}^{(2\omega)} = i 2\omega \left(\mathbf{P}_s^{(2\omega)} \cdot \hat{\boldsymbol{n}} / \delta\right) \hat{\boldsymbol{n}},$$

which is exactly compensated by the normal component of the displacement current density:

$$\boldsymbol{J}_{s\perp}^{(2\omega)} + i2\omega \boldsymbol{D}_{\perp}^{(2\omega)} = 0,$$

otherwise there would be an unbounded magnetic field. Therefore, in the selvedge region:

$$\boldsymbol{D}_{\perp}^{(2\omega)} = -\left(\boldsymbol{P}_{s}^{(2\omega)} \cdot \hat{\boldsymbol{n}}/\delta\right) \hat{\boldsymbol{n}}.$$

From the Faraday-Neumann's law, applied to the elementary curve Δl shown in Fig. 6.1(b), we have:

$$\left(\mathbf{E}_i^{(2\omega)} - \mathbf{E}_e^{(2\omega)}\right)|_\Sigma \cdot \Delta l_{\|} = u_2 - u_1,$$

where $u_{(\alpha)} = \int_{\Delta l_{\perp}^{(\alpha)}} \mathbf{E}^{(2\omega)} \cdot d\boldsymbol{l} = (\mathbf{P}_s^{(2\omega)} \cdot \hat{\mathbf{n}})\Big|_{Q^{(\alpha)}}$ and $\alpha = 1, 2$. By combining these relations we obtain:

$$\hat{\mathbf{n}} \times \left(\mathbf{E}_i^{(2\omega)} - \mathbf{E}_e^{(2\omega)}\right)\Big|_\Sigma = \hat{\mathbf{n}} \times \nabla_S \left(\mathbf{P}_s^{(2\omega)} \cdot \hat{\mathbf{n}}\right)/\varepsilon'.$$

The theoretical and experimental determination of the parameters γ, δ', $\chi_{\perp\perp\perp}$, $\chi_{\perp\|\|}$ and $\chi_{\perp\|\perp}$ has been a long-standing problem in Nonlinear Optics, and it is still an open issue [43, 50, 51, 52].

The source of the nonlinearity in metals results from the response of both bound and free electrons. In particular, for the visible/near-IR part of the light spectrum, the nonlinear response of thick metal particles may be attributed mostly to the free electrons [48, 43, 57, 56]. They behave as an isotropic electron gas with effective mass m_{eff}, relaxation time τ (due to the collisions with the ion lattice) and a quantum pressure. The electron gas dynamics are governed by the Euler's equation. This is the so-called *hydrodynamic model*. Within it, the bulk contribution to the nonlinear polarization arises from both the convective term and the Lorentz's force term, while the surface contributions are strictly related to the response of the electrons within the Thomas-Fermi screening length ($\lambda_{TF} \approx 1$Å for gold) from the surface [43, 117]. Since in our case $\omega\tau >> 1$, the hydrodynamic model gives the following expressions for the bulk parameters γ and δ' [118, 51]:

$$\gamma = -\frac{1}{8}\chi_b(\omega)\frac{\omega_p^2}{\omega^2}\frac{\varepsilon_0}{en_0} \tag{6.5a}$$

$$\delta' \cong i\frac{2\gamma}{\omega\tau} \tag{6.5b}$$

where $\chi_b(\omega) = \varepsilon_i(\omega)/\varepsilon_0 - 1$ is the linear bulk permittivity of the metal, n_0 is the equilibrium number density of the free electrons, $\omega_p = \sqrt{n_0 e^2/m_{eff}\varepsilon_0}$ is the free electron plasma frequency and $-e$ is the electron charge.

In the same limit $\omega\tau >> 1$, the hydrodynamic model also gives the following estimation for the surface parameters $\chi_{\perp\perp\perp}$ and $\chi_{\parallel\perp\parallel}$, that has been already introduced in Chapter 2 [43, 50]:

$$\chi_{\perp\perp\perp} = -\frac{1}{4}\chi_b\left(\omega\right)\frac{\omega_p^2}{\omega^2}\frac{\varepsilon_0}{en_0}, \tag{6.6a}$$

$$\chi_{\parallel\perp\parallel} = \frac{1}{2}\chi_b\left(\omega\right)\frac{\omega_p^2}{\omega^2}\frac{\varepsilon_0}{en_0}, \tag{6.6b}$$

Furthermore, the contribution of the term $\chi_{\perp\parallel\parallel}$ is generally considered negligible [42, 43, 51, 52].

Alternatively, the parameters of the SH sources may be identified experimentally. This would allow to account for phenomena that are disregarded in the hydrodynamic model, as the interband transitions. Nevertheless, an identification of the parameters γ, δ', $\chi_{\perp\perp\perp}$, $\chi_{\perp\parallel\parallel}$ and $\chi_{\parallel\perp\parallel}$ through measurements of the SH radiation has an intrinsic limit. In fact, the parameter γ cannot be separated from the surface terms $\chi_{\perp\perp\perp}$ and $\chi_{\perp\parallel\parallel}$, through measurements of the SH field outside the metal. An equivalent surface nonlinear polarization with surface susceptibility:

$$\chi_{surf,eff} = \chi_{eff}\left[\hat{\boldsymbol{n}}\hat{\boldsymbol{n}}\hat{\boldsymbol{n}} + \hat{\boldsymbol{n}}(\hat{\boldsymbol{t}}_1\hat{\boldsymbol{t}}_1 + \hat{\boldsymbol{t}}_2\hat{\boldsymbol{t}}_2)\right], \tag{6.7}$$

where $\chi_{eff} = \gamma(\omega)\varepsilon_0/\varepsilon_i(2\omega)$, generates outside the metal the same electromagnetic field generated by the γ term. For this reason the contribution of the γ term is called *surface-like* bulk term [51].

This is an ancient problem in Nonlinear Optics. Sipe *et al.* pointed out this ambiguity for the first time by analyzing the SH radiation generated by a planar slab [50]. Moreover, they inferred that this property holds true for any material and shape. In this Chapter we also provide a very simple demonstration of this general property, following Ref. [108].

On the contrary, Wang *et al.* unambiguously determined the δ' bulk term in the SH radiation generated from a gold film, by using a two-beam SH generation measurement technique [51]. However, the Authors conclude "...that the surface-like contributions dominate and that the pure bulk component makes only a minor contribution" to the SH radiation generated from a planar slab. Since the contribution of the δ' term depends on the spatial derivatives of $\mathbf{E}^{(\omega)}$, its magnitude may be significant when $\mathbf{E}^{(\omega)}$ is rapidly varying in the bulk of the metal [51]. The importance of the δ' contribution to the SH radiation from non-planar geometries is still an open problem.

6.2 SECOND-HARMONIC SCATTERING FROM SPHERES

Let us consider the electromagnetic field at frequency 2ω generated from a metal sphere of radius R, when illuminated by a time-harmonic electromagnetic plane-wave at frequency ω incoming from infinity. We use the convention $\mathbf{a}(\mathbf{r},t) = \mathrm{Re}\left\{\mathbf{A}^{(\Omega)}(\mathbf{r})\exp(i\Omega t)\right\}$ for representing a time harmonic electromagnetic field at angular frequency Ω, where $\mathbf{r} = r\hat{\mathbf{r}}$.

The SH generation problem involves two electromagnetic fields oscillating at different frequencies: the electromagnetic field $\left(\mathbf{E}^{(\omega)},\mathbf{H}^{(\omega)}\right)$ at fundamental frequency ω and the *second-harmonic* electromagnetic field $\left(\mathbf{E}^{(2\omega)},\mathbf{H}^{(2\omega)}\right)$ at frequency 2ω. We denote with $\left(\mathbf{E}_0^{(\omega)},\mathbf{H}_0^{(\omega)}\right)$ the *incident (pump)* electromagnetic field:

$$
\begin{aligned}
\mathbf{E}_0^{(\omega)} &= E_0\hat{\varepsilon}_0 e^{-i\mathbf{k}_0^{(\omega)}\cdot\mathbf{r}} \\
\mathbf{H}_0^{(\omega)} &= \frac{E_0}{\zeta_e}\left(\hat{\mathbf{k}}_0 \times \hat{\varepsilon}_0\right) e^{-i\mathbf{k}_0^{(\omega)}\cdot\mathbf{r}} ,
\end{aligned}
\tag{6.8}
$$

where E_0 is the electric field amplitude of the linearly-polarized pump beam, $\hat{\varepsilon_0}$ is its polarization direction, $\hat{\mathbf{k}}_0$ is its propagation direction, $\mathbf{k}_0^{(\omega)} = \hat{\mathbf{k}}_0 k_e(\omega)$, $k_e(\omega) = \omega\sqrt{\mu_e\varepsilon_e}$ and $\zeta_e = \sqrt{\mu_e/\varepsilon_e}$. The parameters ε_e and μ_e are the permittivity and the permeability of the embedding medium.

Since the intensities of the SH fields generated by noble metals are always orders of magnitude weaker than the intensities of the pump fields, the SH fields do not significantly couple back to the fundamental fields (*undepleted-pump approximation*). As a result, the electromagnetic scattering problems at the fundamental frequency and at the SH frequency are both linear. The linear electromagnetic response of the metal is characterized by the permittivity ε_i, which depends on the frequency, and by the permeability μ_i, that we assume independent of the frequency.

In order to calculate the SH radiation generated by the metal sphere, we have to evaluate:

1. the electric field $\mathbf{E}^{(\omega)}$ in $\dot{\Omega}_i$ and on the inner page of Σ (that we have denoted with Σ_i), induced by the pump electromagnetic field $\left(\mathbf{E}_0^{(\omega)},\mathbf{H}_0^{(\omega)}\right)$;
2. the SH nonlinear polarization sources generated by $\mathbf{E}^{(\omega)}$;
3. the electromagnetic fields $\left(\mathbf{E}^{(2\omega)},\mathbf{H}^{(2\omega)}\right)$ radiated by the SH nonlinear polarization fields.

Both problems 1) and 3) are solved by expressing the unknown fields in terms of SVWFs.

The electromagnetic fields at the pump frequency are solved by means of the well-known Mie theory, which has been already described in Chapter 3. The SH electromagnetic field satisfies the Maxwell's equations:

$$\begin{cases} \nabla \times \mathbf{E}_i^{(2\omega)} = -2i\omega\mu_i \mathbf{H}_i^{(2\omega)} \\ \nabla \times \mathbf{H}_i^{(2\omega)} = 2i\omega\varepsilon_i\left(2\omega\right)\mathbf{E}_i^{(2\omega)} + \mathbf{J}_b^{(2\omega)} \end{cases} \quad \text{in } \hat{\Omega}_i, \tag{6.9a}$$

$$\begin{cases} \hat{\mathbf{n}} \times \left(\mathbf{H}_i^{(2\omega)} - \mathbf{H}_e^{(2\omega)}\right) = -\mathbf{j}_{elet}^{(2\omega)} \\ \hat{\mathbf{n}} \times \left(\mathbf{E}_i^{(2\omega)} - \mathbf{E}_e^{(2\omega)}\right) = \mathbf{j}_{mag}^{(2\omega)} \end{cases} \quad \text{on } \Sigma\,, \tag{6.9b}$$

$$\begin{cases} \nabla \times \mathbf{E}_e^{(2\omega)} = -2i\omega\mu_e \mathbf{H}_e^{(2\omega)} \\ \nabla \times \mathbf{H}_e^{(2\omega)} = 2i\omega\varepsilon_e \mathbf{E}_e^{(2\omega)} \end{cases} \quad \text{in } \hat{\Omega}_e\,, \tag{6.9c}$$

where

$$\mathbf{J}_b^{(2\omega)} = 2i\omega\mathbf{P}_b^{(2\omega)}, \tag{6.10a}$$

$$\mathbf{j}_{elet}^{(2\omega)} = -2i\omega\hat{\mathbf{n}} \times \left(\hat{\mathbf{n}} \times \mathbf{P}_s^{(2\omega)}\right), \tag{6.10b}$$

$$\mathbf{j}_{mag}^{(2\omega)} = \frac{1}{\varepsilon'}\hat{\mathbf{n}} \times \nabla_s \left(\hat{\mathbf{n}} \cdot \mathbf{P}_s^{(2\omega)}\right), \tag{6.10c}$$

the operator ∇_s denotes the surface gradient, $\left(\mathbf{E}_i^{(2\omega)}, \mathbf{H}_i^{(2\omega)}\right)$ denote the SH fields in $\dot{\Omega}_i$, $\left(\mathbf{E}_e^{(2\omega)}, \mathbf{H}_e^{(2\omega)}\right)$ denote the SH fields in $\dot{\Omega}_e$ and ε' is the *selvedge region* permittivity [43], which we assumed equal to ε_0.

The sources of the SH radiation, therefore, are of three types. The volume current density field $\mathbf{J}_b^{(2\omega)}$ given by Eq. (6.10a), takes into account the contribution of the SH bulk nonlinear polarization. The surface electric current density $\mathbf{j}_{elet}^{(2\omega)}$ given by Eq. (6.10b), takes into account the contribution of the SH tangent surface nonlinear polarization. The surface magnetic current density $\mathbf{j}_{mag}^{(2\omega)}$ given by (6.10c), takes into account the contribution of the SH normal surface nonlinear polarization. The systems of Eq. (6.9a) have to be solved with the radiation condition at infinity for $\left(\mathbf{E}_e^{(2\omega)}, \mathbf{H}_e^{(2\omega)}\right)$.

The SH field equations are formally the same of the fundamental field equations except for the bulk source term $\mathbf{J}_b^{(2\omega)}$ in the Maxwell-Ampere equation and the substitutions $\omega \to 2\omega$. Consequently, the problem is reduced to that already solved for the fundamental fields, by expressing the electromagnetic field inside the nanoparticle (Ω_i) as:

$$\begin{cases} \mathbf{E}_i^{(2\omega)} = \mathbf{E}_{hom}^{(2\omega)} + \mathbf{E}_{par}^{(2\omega)} \\ \mathbf{H}_i^{(2\omega)} = \mathbf{H}_{hom}^{(2\omega)} + \mathbf{H}_{par}^{(2\omega)} \end{cases}, \tag{6.11}$$

where $\left(\mathbf{E}_{\mathrm{hom}}^{(2\omega)}, \mathbf{H}_{\mathrm{hom}}^{(2\omega)}\right)$ is the general solution of Eq. (6.9a) in absence of the source term, and $\left(\mathbf{E}_{\mathrm{par}}^{(2\omega)}, \mathbf{H}_{\mathrm{par}}^{(2\omega)}\right)$ is a particular solution of the complete system of Eq. (6.9a). The contribution $\left(\mathbf{E}_{\mathrm{hom}}^{(2\omega)}, \mathbf{H}_{\mathrm{hom}}^{(2\omega)}\right)$ will be represented as the electromagnetic field at the fundamental frequency. The particular solution $\left(\mathbf{E}_{\mathrm{par}}^{(2\omega)}, \mathbf{H}_{\mathrm{par}}^{(2\omega)}\right)$ contains two contributions, one takes into account the γ term $\left(\mathbf{E}_{\gamma}^{(2\omega)}, \mathbf{H}_{\gamma}^{(2\omega)}\right)$ and the other takes into account the δ' term $\left(\mathbf{E}_{\delta'}^{(2\omega)}, \mathbf{H}_{\delta'}^{(2\omega)}\right)$. The term $\left(\mathbf{E}_{\gamma}^{(2\omega)}, \mathbf{H}_{\gamma}^{(2\omega)}\right)$ is given by the simple expression [61]:

$$\begin{cases} \mathbf{E}_{\gamma}^{(2\omega)} = -\frac{\varepsilon_0}{\varepsilon_i(2\omega)}\gamma\nabla\left(\mathbf{E}^{(\omega)}\cdot\mathbf{E}^{(\omega)}\right) \\ \mathbf{H}_{\gamma}^{(2\omega)} = 0 \end{cases} \tag{6.12}$$

Instead, the term $\left(\mathbf{E}_{\delta'}^{(2\omega)}, \mathbf{H}_{\delta'}^{(2\omega)}\right)$ can be evaluated by using the expansion in SVWFs or the Green's function for a medium with electric permittivity ε_i and magnetic permeability μ_i.

Therefore, the fields $\left(\mathbf{E}_{\mathrm{hom}}^{(2\omega)}, \mathbf{H}_{\mathrm{hom}}^{(2\omega)}\right)$ and $\left(\mathbf{E}_{e}^{(2\omega)}, \mathbf{H}_{e}^{(2\omega)}\right)$ are solutions of the homogeneous Maxwell's equations at frequency 2ω and have to satisfy on Σ the boundary equations:

$$\begin{cases} \hat{\mathbf{r}}\times\left(\mathbf{H}_{\mathrm{hom}}^{(2\omega)} - \mathbf{H}_{e}^{(2\omega)}\right) = -\mathbf{j}_{\mathrm{elet}}^{(2\omega)} - \hat{\mathbf{r}}\times\mathbf{H}_{\delta'}^{(2\omega)} \\ \hat{\mathbf{r}}\times\left(\mathbf{E}_{\mathrm{hom}}^{(2\omega)} - \mathbf{E}_{e}^{(2\omega)}\right) = \left(\mathbf{j}_{\mathrm{mag}}^{(2\omega)} - \hat{\mathbf{r}}\times\mathbf{E}_{\gamma}^{(2\omega)}\right) - \hat{\mathbf{r}}\times\mathbf{E}_{\delta'}^{(2\omega)} \end{cases} \tag{6.13}$$

By combining Equations (6.10c), (6.12) and (6.13), it results that the contribution of the term γ to the SH electromagnetic field at the external of the particle may be described by the equivalent surface sources of Eq. 6.7.

The unknown fields $\left(\mathbf{E}_{\mathrm{hom}}^{(2\omega)}, \mathbf{H}_{\mathrm{hom}}^{(2\omega)}\right)$ and $\left(\mathbf{E}_{e}^{(2\omega)}, \mathbf{H}_{e}^{(2\omega)}\right)$ are represented as:

$$\begin{aligned} \mathbf{E}_{\mathrm{hom}}^{(2\omega)}(r,\theta,\phi) = -E_c^{(2\omega)} \sum_{n=1}^{\infty}\sum_{m=-n}^{n} & c_{mn}^{(2\omega)}\mathbf{M}_{mn}^{(1)}\left[k_i(2\omega)r,\theta,\phi\right] \\ & + d_{mn}^{(2\omega)}\mathbf{N}_{mn}^{(1)}\left[k_i(2\omega)r,\theta,\phi\right] \\ \mathbf{H}_{\mathrm{hom}}^{(2\omega)}(r,\theta,\phi) = \frac{E_c^{(2\omega)}}{i\zeta_i(2\omega)} \sum_{n=1}^{\infty}\sum_{m=-n}^{n} & d_{mn}^{(2\omega)}\mathbf{M}_{mn}^{(1)}\left[k_i(2\omega)r,\theta,\phi\right] \\ & + c_{mn}^{(2\omega)}\mathbf{N}_{mn}^{(1)}\left[k_i(2\omega)r,\theta,\phi\right] \end{aligned} \tag{6.14a}$$

for $r < R$, and

$$\begin{aligned}\mathbf{E}_e^{(2\omega)}(r,\theta,\phi) = E_c^{(2\omega)} \sum_{n=1}^{\infty}\sum_{m=-n}^{n} & b_{mn}^{(2\omega)}\mathbf{M}_{mn}^{(3)}\left[k_e(2\omega)r,\theta,\phi\right] \\ & + a_{mn}^{(2\omega)}\mathbf{N}_{mn}^{(3)}\left[k_e(2\omega)r,\theta,\phi\right] \\ \mathbf{H}_e^{(2\omega)}(r,\theta,\phi) = -\frac{E_c^{(2\omega)}}{i\zeta_e} \sum_{n=1}^{\infty}\sum_{m=-n}^{n} & a_{mn}^{(2\omega)}\mathbf{M}_{mn}^{(1)}\left[k_e(2\omega)r,\theta,\phi\right] \\ & + b_{mn}^{(2\omega)}\mathbf{N}_{mn}^{(1)}\left[k_e(2\omega)r,\theta,\phi\right]\end{aligned} \tag{6.14b}$$

for $r > R$, where $E_c^{(2\omega)} = {E_0}^2/E_b$ is a characteristic electric field expressing the order of magnitude of the SH electric field in the nanoparticle, and $E_b = \omega c_0 m_{eff}/(\chi_b(\omega)e)$.

Both the expressions of $\left(\mathbf{E}_{hom}^{(2\omega)}, \mathbf{H}_{hom}^{(2\omega)}\right)$ and $\left(\mathbf{E}_e^{(2\omega)}, \mathbf{H}_e^{(2\omega)}\right)$ satisfy the homogeneous Maxwell's equations at frequency 2ω. The unknown coefficients $\left\{a_{mn}^{(2\omega)}, b_{mn}^{(2\omega)}\right\}$ and $\left\{c_{mn}^{(2\omega)}, d_{mn}^{(2\omega)}\right\}$ are evaluated by imposing the boundary equations (6.13).

When the contribution of the δ' term is negligible, the right-hand sides of Eq. (6.13) are given, in terms of SVWFs, by:

$$\begin{aligned}& -\mathbf{j}_{elet}^{(2\omega)}(\theta,\phi) = \\ & \qquad \frac{E_c^{(2\omega)}}{i\zeta_e}\sum_{n=1}^{\infty}\sum_{m=-n}^{n}\left[{v'}_{mn}^{(2\omega)}\mathbf{X}_{mn}(\theta,\phi) + {u'}_{mn}^{(2\omega)}\hat{\mathbf{r}}\times\mathbf{X}_{mn}(\theta,\phi)\right], \\ & \mathbf{j}_{mag}^{(2\omega)}(\theta,\phi) - \hat{\mathbf{r}}\times\mathbf{E}_{part}^{(2\omega)}(r=R,\theta,\phi) = \\ & \qquad\qquad - E_c^{(2\omega)}\sum_{n=1}^{\infty}\sum_{m=-n}^{n}\left[{u''}_{mn}^{(2\omega)}\hat{\mathbf{r}}\times\left[\hat{\mathbf{r}}\times\mathbf{X}_{mn}(\theta,\phi)\right]\right].\end{aligned} \tag{6.15}$$

The coefficients $\left\{{u'}_{mn}^{(2\omega)}, {v'}_{mn}^{(2\omega)}\right\}$ for the surface tangential source can be expressed as:

$$\begin{aligned}{u'}_{mn}^{(2\omega)} = i2\left(-\frac{b}{2}\right)\frac{\zeta_e}{\zeta_0}\sum_{n_1}^{\infty}\sum_{m_1=-n_1}^{n_1}\sum_{n_2}^{\infty}\sum_{m_2=-n_2}^{n_2} & A_{m_1n_1}^{(1)}A_{m_2n_2}^{(-1)}C_{n_1m_1n_2m_2nm}^{(1,0,-1)} \\ & + A_{m_1n_1}^{(0)}A_{m_2n_2}^{(-1)}C_{n_1m_1n_2m_2nm}^{(1,1,-1)} \\ {v'}_{mn}^{(2\omega)} = -2\left(-\frac{b}{2}\right)\frac{\zeta_e}{\zeta_0}\sum_{n_1}^{\infty}\sum_{m_1=-n_1}^{n_1}\sum_{n_2}^{\infty}\sum_{m_2=-n_2}^{n_2} & A_{m_1n_1}^{(1)}A_{m_2n_2}^{(-1)}C_{n_1m_1n_2m_2nm}^{(0,0,-1)} \\ & + A_{m_1n_1}^{(0)}A_{m_2n_2}^{(-1)}C_{n_1m_1n_2m_2nm}^{(0,1,-1)}\end{aligned}$$

where the coefficients $C^{(p,q,r)}_{J_1M_1J_2M_2JM}$ are defined in Appendix A.5. The coefficients $\left\{u''^{(2\omega)}_{mn}, v''^{(2\omega)}_{mn}\right\}$ for both the γ bulk and the surface normal polarization source can be expressed as:

$$\begin{aligned}
u''^{(2\omega)}_{mn} =& \left(-\frac{a}{4}\right) i\sqrt{n(n+1)}\frac{g_{mn}(k_i(\omega)R)}{k_0(\omega)R} \\
&+\left(-\frac{d}{8}\right)\frac{\varepsilon_0}{\varepsilon_i(2\omega)} i\sqrt{n(n+1)}\frac{f_{mn}(k_i(\omega)R)+g_{mn}(k_i(\omega)R)}{k_0(\omega)R} \\
v''^{(2\omega)}_{mn} =& 0
\end{aligned}$$

where

$$g_{mn}(k_i(\omega)R) = \sum_{n_1m_1}\sum_{n_2m_2}\left\{A^{(-1)}_{m_1n_1}A^{(-1)}_{m_2n_2}W^{(-1,-1)}_{n_1m_1n_2m_2nm}\right\}$$

$$\begin{aligned}
f_{mn}(k_i(\omega)R) = \sum_{n_1m_1}\sum_{n_2m_2} & \left\{A^{(0)}_{m_1n_1}A^{(0)}_{m_2n_2}W^{(0,0)}_{n_1m_1n_2m_2nm}\right\} \\
&+\left\{A^{(0)}_{m_1n_1}A^{(1)}_{m_2n_2}W^{(0,1)}_{n_1m_1n_2m_2nm}\right\} \\
&+\left\{A^{(1)}_{m_1n_1}A^{(0)}_{m_2n_2}W^{(1,0)}_{n_1m_1n_2m_2nm}\right\} \\
&+\left\{A^{(1)}_{m_1n_1}A^{(1)}_{m_2n_2}W^{(1,1)}_{n_1m_1n_2m_2nm}\right\}
\end{aligned}$$

and the coefficients $W^{(p,q)}_{J_1M_1J_2M_2JM}$ are defined in Appendix A.4. The formulas of the unknown coefficients $\left\{a^{(2\omega)}_{mn}, b^{(2\omega)}_{mn}\right\}$ and $\left\{c^{(2\omega)}_{mn}, d^{(2\omega)}_{mn}\right\}$ are then:

$$\begin{aligned}
a^{(2\omega)}_{mn} &= a'^{(2\omega)}_{mn} + a''^{(2\omega)}_{mn}, \quad & b^{(2\omega)}_{mn} &= b'^{(2\omega)}_{mn} + b''^{(2\omega)}_{mn}, \\
c^{(2\omega)}_{mn} &= c'^{(2\omega)}_{mn} + c''^{(2\omega)}_{mn}, \quad & d^{(2\omega)}_{mn} &= d'^{(2\omega)}_{mn} + d''^{(2\omega)}_{mn},
\end{aligned}$$

where with one apex we denote the contribution due to the tangential surface SH sources and with two apices we denote the contributions of both the normal surface SH sources and the γ bulk SH sources. For the contribution of the tangential surface SH sources we have:

$$\begin{aligned}
\frac{a'^{(2\omega)}_{mn}}{u'^{(2\omega)}_{mn}} &= \frac{x_e^{(2\omega)}\dot{\psi}_n(x_i^{(2\omega)})}{\xi_n(x_e^{(2\omega)})\dot{\psi}_n(x_i^{(2\omega)}) - \frac{\zeta_e}{\zeta_i(2\omega)}\psi_n(x_i^{(2\omega)})\dot{\xi}_n(x_e^{(2\omega)})} \\
\frac{b'^{(2\omega)}_{mn}}{v'^{(2\omega)}_{mn}} &= \frac{x_e^{(2\omega)}\psi_n(x_i^{(2\omega)})}{\frac{\zeta_e}{\zeta_i(2\omega)}\xi_n(x_e^{(2\omega)})\dot{\psi}_n(x_i^{(2\omega)}) - \psi_n(x_i^{(2\omega)})\dot{\xi}_n(x_e^{(2\omega)})} \\
\frac{c'^{(2\omega)}_{mn}}{v'^{(2\omega)}_{mn}} &= \frac{x_i^{(2\omega)}\xi_n(x_e^{(2\omega)})}{\psi_n(x_i^{(2\omega)})\dot{\xi}_n(x_e^{(2\omega)}) - \frac{\zeta_e}{\zeta_i(2\omega)}\xi_n(x_e^{(2\omega)})\dot{\psi}_n(x_i^{(2\omega)})} \\
\frac{d'^{(2\omega)}_{mn}}{u'^{(2\omega)}_{mn}} &= \frac{x_i^{(2\omega)}\dot{\xi}_n(x_e^{(2\omega)})}{\frac{\zeta_e}{\zeta_i(2\omega)}\psi_n(x_i^{(2\omega)})\dot{\xi}_n(x_e^{(2\omega)}) - \xi_n(x_e^{(2\omega)})\dot{\psi}_n(x_i^{(2\omega)})}
\end{aligned}$$

where $x_e^{(2\omega)} = k_e^{(2\omega)}R,\;\; x_i^{(2\omega)} = k_i^{(2\omega)}R$, $\psi_n = \psi_n(\rho)$, $\xi_n = \xi_n(\rho)$ are the Riccati-Bessel functions. For the contribution of both the normal surface SH sources and the γ bulk SH sources we have:

$$\frac{a''^{(2\omega)}_{mn}}{u''^{(2\omega)}_{mn}} = \frac{\frac{\zeta_e}{\zeta_i(2\omega)} x_e^{(2\omega)} \psi_n(x_i^{(2\omega)})}{\frac{\zeta_e}{\zeta_i(2\omega)} \psi_n(x_i^{(2\omega)}) \dot{\xi}_n(x_e^{(2\omega)}) - \xi_n(x_e^{(2\omega)}) \dot{\psi}_n(x_i^{(2\omega)})}$$

$$b''^{(2\omega)}_{mn} = 0$$

$$c''^{(2\omega)}_{mn} = 0$$

$$\frac{d''^{(2\omega)}_{mn}}{u''^{(2\omega)}_{mn}} = \frac{x_i^{(2\omega)} \xi_n(x_e^{(2\omega)})}{\xi_n(x_e^{(2\omega)}) \dot{\psi}_n(x_i^{(2\omega)}) - \frac{\zeta_e}{\zeta_i(2\omega)} \psi_n(x_i^{(2\omega)}) \dot{\xi}_n(x_e^{(2\omega)})}$$

6.3 GOLD NANOSPHERES

In the present Section, by using the analytical solution derived in the previous one, we analyze the SH generation from an isolated gold nanosphere in vacuum, as the radius, the pump wavelength and polarization vary. Specifically, we study the SH radiation generated at pump wavelengths of $\lambda = 780\ \mathrm{nm}$ (Ti:sapphire laser) and $\lambda = 520\ \mathrm{nm}$ (gold plasmon resonance). Particular care has been devoted to the comparison with the existing theories in the Rayleigh regime. In order to model the bulk linear susceptibility of gold, we interpolated Johnson and Christy's experimental data [38].

In order to adequately represent the electromagnetic fields at the fundamental and the second-harmonic frequencies, it has been sufficient to consider the degree n up to 10, for the cases of our interest. Only the first 3 and the first 6 multipoles have significant amplitude at the fundamental and the second-harmonic frequencies, respectively.

Following Ref. [52], we express $\chi_{\perp\perp\perp}$, $\chi_{\parallel\perp\parallel}$ and γ in terms of the *Rudnick-Stern (R-S) parameters* (a, b, d) [42, 43]:

$$\chi_{\perp\perp\perp} = -\frac{a}{4}\chi_b(\omega)\frac{\omega_p^2}{\omega^2}\frac{\varepsilon_0}{en_0}, \tag{6.16a}$$

$$\chi_{\parallel\perp\parallel} = -\frac{b}{2}\chi_b(\omega)\frac{\omega_p^2}{\omega^2}\frac{\varepsilon_0}{en_0}, \tag{6.16b}$$

$$\gamma = -\frac{d}{8}\chi_b(\omega)\frac{\omega_p^2}{\omega^2}\frac{\varepsilon_0}{en_0}, \tag{6.16c}$$

where χ_b is the bulk linear susceptibility of the metal. By choosing $(a = 1,\ b = -1,\ d = 1)$, we obtain the Sipe's hydrodynamic model.[43] By measuring the SH generated by gold spherical nanoparticles with $R = 150\ \mathrm{nm}$ at $\lambda = 800\ \mathrm{nm}$, Bachelier et al. have found that an optimal choice for the phenomenological parameters a, b and d should be $(a = 0.5 - i0.25,\ b = 0.1,\ d = 1)$ [52]. We discuss the solutions obtained by using both sets of values.

The pump electromagnetic field is a plane-wave propagating along the positive direction of the $z-$axis, and linearly polarized in the xy plane, with a polarization direction $\hat{\varepsilon}_0$. We indicate with α the angle between the unit vector $\hat{\varepsilon}_0$ and $x-$axis (the reference versus is counterclockwise, seen from the half-space $z > 0$), as shown in Fig. 6.2.

In order to characterize the SH radiation, we consider both the SH power per unit solid angle and the SH scattering cross-section. The SH power per unit solid angle $dP_{\hat{\varepsilon}^*}^{(2\omega)}(\hat{\boldsymbol{K}})/d\Omega$, radiated in the farfield along the direction $\hat{\mathbf{K}}$ and collected by an analyzer with polarization state $\hat{\varepsilon}^*$ is defined as:

$$\frac{dP_{\hat{\varepsilon}^*}^{(2\omega)}(\hat{\mathbf{K}})}{d\Omega} = \lim_{r\to\infty}\left[\frac{r^2}{2\zeta_e}\left|\hat{\varepsilon}^*\cdot\mathbf{E}_e^{(2\omega)}(\hat{\mathbf{K}})\right|^2\right]. \tag{6.17}$$

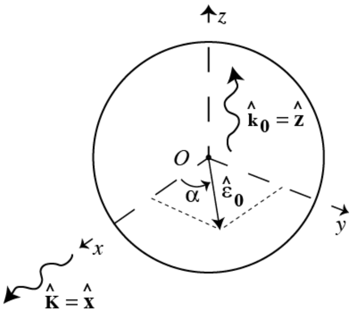

Figure 6.2: SH scattering geometry. The pump electromagnetic field propagates along the positive direction of the $z-$axis and is linearly polarized along $\hat{\varepsilon}_0$. The SH scattered field is observed along the direction $\hat{\mathbf{K}} = \hat{\mathbf{x}}$ (the scattering plane is xOz). The $z-$ and $y-$ components of the SH field are considered, respectively parallel ($\|$) and orthogonal ($\perp$) with respect to the scattering plane.

The SH scattering cross-section $C_{sca}^{(2\omega)}$ is given by:

$$C_{sca}^{(2\omega)} = \lim_{\rho \to \infty} \frac{\int_{\Sigma_\rho} \left| \mathbf{E}_e^{(2\omega)} \right|^2 \cdot \hat{\mathbf{n}} \, d\Sigma}{\left| \mathbf{E}_0^{(\omega)} \right|^2}, \tag{6.18}$$

where Σ_ρ is a spherical surface with radius ρ, centered at the origin of the coordinate system. $dP_{\hat{\varepsilon}^*}^{(2\omega)}(\hat{\mathbf{K}})/d\Omega$ depends on the collection direction $\hat{\mathbf{K}}$ of the scattered SH light. $C_{sca}^{(2\omega)}$ has the physical dimensions of an area, and it is proportional to the SH generation efficiency.

In order to analyze the SH radiation polarization state, the analyzer can be polarized either parallel ($\|$) or perpendicular ($\perp$) to the SH scattering plane, defined by the propagation direction $\hat{k}_0$ of the pump wave, and the collection direction $\hat{\mathbf{K}}$. We denote with $dP_{\|}^{(2\omega)}/d\Omega$ and $dP_{\perp}^{(2\omega)}/d\Omega$ the radiated powers per unit solid angle associated to the $\|$ and $\perp$ components. The analysis of the polarization state of SH radiation collected at right angle from the pump beam, *i.e.* $\hat{\boldsymbol{K}} = \hat{\boldsymbol{x}}$, is very important because it allows to discriminate the radiation generated by even and odd SH multipole sources. Indeed, only the SH $\mathbf{N}_{mn}^{(3)}$ multipoles with odd n contribute to the $\|$ component and only the SH $\mathbf{N}_{mn}^{(3)}$ multipoles with even n contribute to the $\perp$ component. These behaviors are reversed for the SH $\mathbf{M}_{mn}^{(3)}$ multipoles.

6.3.1 *SH source currents: Rayleigh and Mie regimes*

Here we analyze the SH radiation generated from the single nonlinear sources, acting as if they were radiating independently. Fig. 6.3 shows the magnitude of each SH source current density, namely $\mathbf{J}_b^{(2\omega)}$, $\mathbf{j}_{elet}^{(2\omega)}$, $\mathbf{j}_{mag}^{(2\omega)}$, normalized to their own maxima, and computed for the two pump wavelengths $\lambda = 520\ nm$ and $\lambda = 780\ nm$, corresponding to resonance and off-resonance conditions, respectively. Two nanoparticle radii have been considered, namely a particle with small size ($R = 10\ nm$) and a particle comparable in size to the pump wavelength ($R = 150\ nm$). The pump field is linearly polarized along the x−axis ($\alpha = 0$). In particular, the first column (panels a-d) shows the magnitude of the electric current density $\mathbf{J}_b^{(2\omega)}$ in the xOz plane, while the second and third columns (panels e-h,i-l), show the magnitude of the surface electric $\mathbf{j}_{elet}^{(2\omega)}$ and magnetic $\mathbf{j}_{mag}^{(2\omega)}$ current densities, respectively.

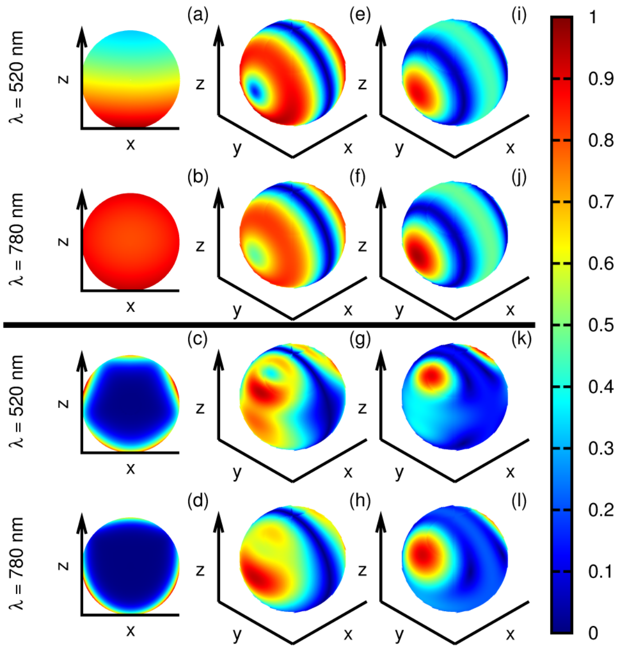

Figure 6.3: SH source current distribution excited by a pump field linearly polarized along x. The nanosphere size is $R = 10\ nm$ (first and second row)and $R = 150\ nm$ (third and fourth row), the pump wavelength is $\lambda = 520\ nm$ (first and third rows) and $\lambda = 780\ nm$ (second and fourth rows). Panels (a,b,c,d) are relative to the bulk current density cut in the xOz plane, panels (e,f,g,h) are relative to the surface electric current density and panels (i,j,k,l) are relative to the surface magnetic current density. Each panel shows the current magnitude normalized to its own maximum.

For small particles, $\mathbf{J}_b^{(2\omega)}$ is significant across the entire particle volume (panel a, b). In particular, while for $\lambda = 520\ nm$ (panel a) $\mathbf{J}_b^{(2\omega)}$ decreases along the direction of forward scattering, for $\lambda =$

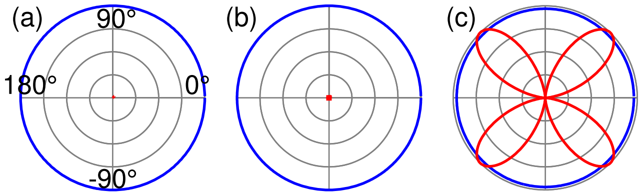

Figure 6.4: SH power per unit solid angle collected at right angle from the pump beam (Fig. 6.2) as function of the pump polarization angle α, for a nanosphere with $R = 10\ nm$. The pump wavelength is $780\ nm$. The blue line corresponds to the $\parallel$ component and the red line to the $\perp$ component with respect to the scattering plane. All the graphs are normalized to the maximum of the most intense component. Panel (a) is relative to the bulk current, panel (b) to the surface electric current, panel (c) to the the surface magnetic current, as if they acted separately.

$780\ nm$ it is almost uniform. For particles with larger size (panels c,d), the skin effect appears, *i.e.* the current $\mathbf{J}_b^{(2\omega)}$ is strongly confined near the particle surface. The intensity distribution of both $\mathbf{j}_{elet}^{(2\omega)}$ and $\mathbf{j}_{mag}^{(2\omega)}$ (e,f,i,j) is symmetric around the polarization direction of the pump field for small particles. As the radius increases, this holds no longer true due to the onset of higher order multipoles (panels g,h,k,l). It is worth noting that the surface electric current density $\mathbf{j}_{elet}^{(2\omega)}$ vanishes on a circle lying in the yOz plane, for any particle size and pump wavelength, as shown in panels (e-h), due to the rotational symmetry of the particle. Similarly, the surface magnetic current density $\mathbf{j}_{mag}^{(2\omega)}$ displays a circle with a constant magnitude for every particle size, as shown in panels (i-l).

In Fig. 6.4 the SH power per unit solid angle collected at right angle from the pump direction is shown for a nanosphere with $R = 10\ nm$. Panels (a), (b) and (c) are relevant to the SH radiation generated by the bulk, surface electric and surface magnetic SH source currents, respectively, as if they acted separately. The blue and red lines correspond respectively to $dP_{\parallel}^{(2\omega)}/d\Omega$ and $dP_{\perp}^{(2\omega)}/d\Omega$, and for each panel both the components are normalized to the maximum of the most intense.

These results agree with those obtained analyzing the SH radiation from a metal nanosphere in the Rayleigh limit. [110, 61] In this regime, the SH radiation coincides with the electromagnetic field radiated by a fictitious electric dipole with effective moment $\mathbf{p}_{eff}^{(2\omega)}(\hat{\mathbf{r}}) \cong \mathbf{p}^{(2\omega)} + i\, k_0 \overleftrightarrow{\mathbf{Q}}^{(2\omega)}\hat{\mathbf{r}}/3$, where $\mathbf{p}^{(2\omega)}$ is the induced SH electric dipole moment ($n = 1$) and $\overleftrightarrow{\mathbf{Q}}^{(2\omega)}$ is the induced SH electric quadrupole moment ($n = 2$). Depending on the component of the SH intensity, two different shapes of the polarization diagrams arise. For each SH source, $dP_{\parallel}^{(2\omega)}/d\Omega$ is due to a SH dipolar electric mode aligned along the propagation direction of the pump, [110, 61] therefore its value is independent of the polarization angle of the pump. On the other hand, the four lobe pattern observed for $dP_{\perp}^{(2\omega)}/d\Omega$ is due to a SH quadrupolar mode. Furthermore, $dP_{\perp}^{(2\omega)}/d\Omega$ is negligible for both $\mathbf{J}_{b}^{(2\omega)}$ and $\mathbf{j}_{elet}^{(2\omega)}$, while it is comparable with $dP_{\parallel}^{(2\omega)}/d\Omega$ for $\mathbf{j}_{mag}^{(2\omega)}$. For larger particles, higher order SH multipoles arise due to larger retardation effects, significantly modifying the SH radiation characteristics, as we shall see in the next Section.

6.3.2 *SH scattering cross-section*

In this Section, we study the SH scattering cross-section $C_{sca}^{(2\omega)}$ for a gold nanosphere, using as *R-S* parameters the values $(a = 1, b = -1, d = 1)$. All the results are relative to the case of a pump plane-wave with electric field of unitary magnitude, *i.e.* $|E_0| = 1\ \mathrm{Vm}^{-1}$. Figure 6.5 shows $C_{sca}^{(2\omega)}$ as function of the pump wavelength (black lines), for four particle sizes. For all the investigated sizes, $C_{sca}^{(2\omega)}$ shows a maximum at $\lambda \approx 520\ \mathrm{nm}$, when the pump wavelength matches the plasmonic resonance of the particle. Another local maximum is also observed at $\lambda \approx 1040\ \mathrm{nm}$. At this wavelength the SH fields resonate in the gold nanosphere. The relative intensity of $C_{sca}^{(2\omega)}$ at $\lambda \approx 1040\ \mathrm{nm}$ increases as the particle size increases. A third local maximum can be observed at $\lambda \approx 700\ \mathrm{nm}$, for certain particle sizes (*e.g.* $R = 100\ \mathrm{nm}$ and $R = 200\ \mathrm{nm}$). Similar trends, not shown here, have been found with the set of values $(a = 0.5 - i0.25, b = 0.1, d = 1)$ for the *R-S* parameters.

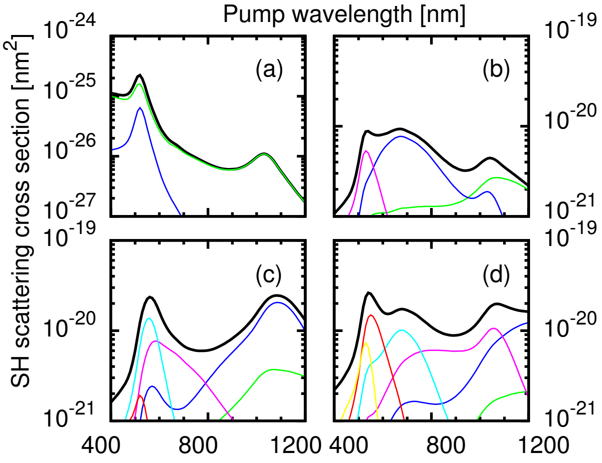

Figure 6.5: SH scattering cross-section (black line) as function of the pump wavelength for nanospheres with $R = 10\ \mathrm{nm}$ (a), $R = 100\ \mathrm{nm}$ (b), $R = 150\ \mathrm{nm}$ (c), $R = 200\ \mathrm{nm}$ (d), with $(a = 1, b = -1, d = 1)$. The contribution of each multipolar order to the total radiation cross-section is shown up to the 6th: $n = 1$ (green), $n = 2$ (blue), $n = 3$ (violet), $n = 4$ (cyan), $n = 5$ (red), $n = 6$ (yellow).

In order to unveil the multipolar origin of the SH radiation in the Rudnick-Stern model, the contributions of each multipole are shown, up to the 6th order. For $R = 10\ \mathrm{nm}$ (panel a), $C_{sca}^{(2\omega)}$ is mostly due to the SH dipolar source, and only for short wavelengths the SH quadrupolar source begins to be significant. As we increase the radius R to $100\ \mathrm{nm}$ (panel b), we can identify three different regimes: for short wavelengths $\lambda < 550\ \mathrm{nm}$, $C_{sca}^{(2\omega)}$ is dominated by the octupolar source, the quadrupolar one prevails in the range $550\ \mathrm{nm} < \lambda < 950\ \mathrm{nm}$, while the dipolar source is the most intense for large wavelengths.

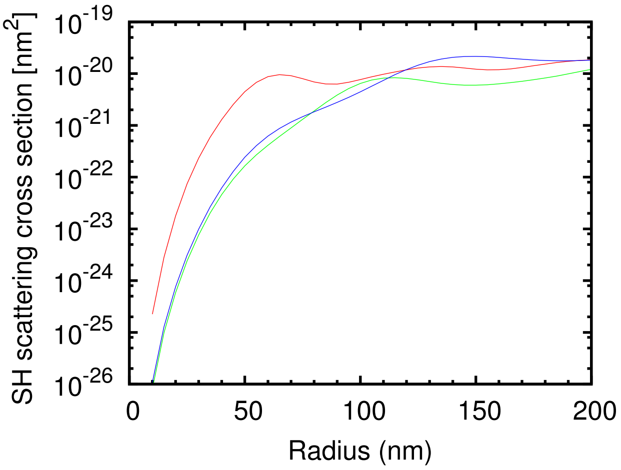

Figure 6.6: SH scattering cross-section as function of the nanosphere radius R at pump wavelengths $\lambda = 520$ nm (red), $\lambda = 780$ nm (green), $\lambda = 1040$ nm (blue), obtained with $(a = 1, b = -1, d = 1)$.

For a particle with $R = 150$ nm (panel c), the dipolar source is negligible regardless of the pump wavelength, and the main contributions to $C_{sca}^{(2\omega)}$ arise from the multipoles with $n = 2, 3, 4$. Similarly, the main contributions for a particle with $R = 200$ nm arise from $n = 2, 3, 4$ for large wavelength, and from the multipoles $n = 5, 6$ for short wavelengths.

Figure 6.6 shows the SH scattering cross-section as function of the nanoparticle radius, for three values of the pump wavelength ($\lambda = 520$ nm, 780 nm, 1040 nm). The SH scattering cross-section increases more than 4 orders of magnitude when the particle size increases up to $R = 100$ nm. For larger radii, the SH scattering cross-section saturates and a small modulation takes place. For small particle size, the highest cross-section is shown when the particle is in plasmonic resonance (i.e., red curve). For larger particle size, the magnitude of $C_{sca}^{(2\omega)}$ is comparable for all the investigated pump wavelengths. Also in this case, similar trends have been found using the set of *R-S* parameters $(a = 0.5 - i0.25, b = 0.1, d = 1)$.

6.3.3 *SH power dependence on the pump polarization*

The SH power radiated at right angle from the propagation direction of the pump allows for the recognition of even- and odd-order multipolar contributions to the SH generation process, as already pointed out. Figure 6.7 shows $dP_{\|}^{(2\omega)}/d\Omega$ and $dP_{\perp}^{(2\omega)}/d\Omega$ as function of the polarization angle α of the pump, for two different choices of *R-S* parameters. The first row (a-d) is relative to the *R-S* parameter set $(a = 1, b = -1, d = 1)$, while the second row (e-h) is relative to the set $(a = 0.5 - i0.25, b = 0.1, d = 1)$. Four different values of particle size are presented: $R = 10$ nm (a,e), $R = 100$ nm (b,f), $R = 150$ nm (c,g), $R = 200$ nm (d,h). Both $dP_{\|}^{(2\omega)}/d\Omega$ and $dP_{\perp}^{(2\omega)}/d\Omega$ are normalized to the maximum of the most intense component. For small (a,e) and very large (d,h) radii, $dP_{\|}^{(2\omega)}/d\Omega$ prevails over the $dP_{\perp}^{(2\omega)}/d\Omega$ for both sets of the *R-S* parameters. For intermediate sizes (b,c,f,g), $dP_{\|}^{(2\omega)}/d\Omega$ and $dP_{\perp}^{(2\omega)}/d\Omega$ are comparable, and their relative intensities strongly depend on the particular choice of the *R-S* parameters. For small particles, $dP_{\|}^{(2\omega)}/d\Omega$ is independent of the polarization angle α (panels a,e), while up to 4 lobes can appear for larger particles, as it will be shown more in detail in Fig. 6.8. The graphs of the component $dP_{\perp}^{(2\omega)}/d\Omega$ feature four lobes oriented along the bisectors of the 4 quadrants, in each of the investigated case.

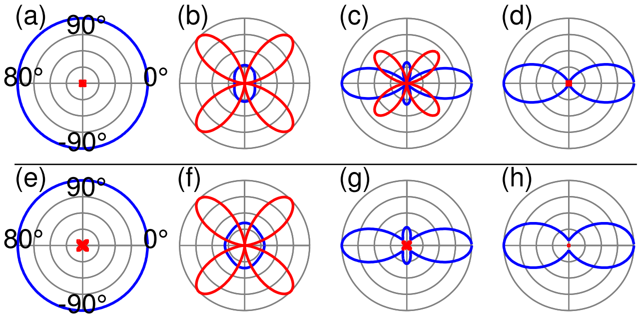

Figure 6.7: SH power per unit solid angle collected at right angle from the pump beam (Fig. 6.2) as function of the pump polarization angle α, for nanosphere with $R = 10$ nm (a,e), $R = 100$ nm (b,f), $R = 150$ nm (c,g), $R = 200$ nm (d,h), obtained by using (a-d) $(a = 1, b = -1, d = 1)$ and (e-h) $(a = 0.5 - i0.25, b = 0.1, d = 1)$. The pump wavelength is $\lambda = 780$ nm. The blue line corresponds to the $\|$ component and the red line to the $\perp$ component with respect to the scattering plane. All the graphs are normalized to the maximum of the most intense component.

The appearance of an octupolar SH source significantly modifies the shape of $dP_{\|}^{(2\omega)}/d\Omega$. In the Rayleigh limit the $\|$ component generated by the SH dipolar source fully prevails over the $\perp$ component generated by the SH quadrupolar source. As the radius increases, the intensity of the SH octupolar source increases due to the retardation

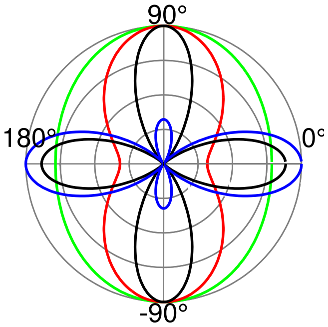

Figure 6.8: SH power per unit solid angle of the $\parallel$ component collected at right angle from the pump beam (Fig. 6.2), as function of the pump polarization angle α, for nanospheres of size $R = 80$ nm (green), $R = 120$ nm (red), $R = 140$ nm (black), $R = 150$ nm(blue) and $(a = 1, b = -1, d = 1)$. The pump wavelength is $\lambda = 780$ nm, all the curves are normalized to their own maximum.

effects, as pointed out in the previous Section. Due to the interference in the far field of the SH dipolar and octupolar fields, the $dP_{\parallel}^{(2\omega)}/d\Omega$ reduces significantly until it becomes smaller than $dP_{\perp}^{(2\omega)}/d\Omega$ (b,c). As the radius further increases, the SH octupolar source prevails over the SH dipolar source, and the shape of $dP_{\parallel}^{(2\omega)}/d\Omega$ gets close to that of an octupole (d,e).

The details of the transition from the dipole to the octupole pattern as the radius increases are shown in Fig. 6.8. First, the circular shape of $dP_{\parallel}^{(2\omega)}/d\Omega$ is shrunk along the directions $\alpha = 0°, 180°$, until the amplitude reaches a null (green and red curves). Then, two lobes arise along these directions (black curve), forming a four-lobe pattern. As the radius further increases, the intensities of the two lobes along the directions at $\alpha = 0°, 180°$ prevail over the intensities of the lobes along the directions at $\alpha = 90°, 270°$ (blue curve). In conclusion we found that, if either the SH dipole or the SH octupole prevail, the polarization properties of the SH radiation obtained by the two sets of *R*-*S* parameters are similar. Otherwise, the interference between the two SH multipoles introduces significant differences. This may provide a fingerprint to evaluate the parameters in the framework of the *R*-*S* model.

6.3.4 *SH radiation diagrams*

Figure 6.9 shows the angular distribution of the SH radiation generated by gold nanospheres, obtained by means of the *R*-*S* parameters $(a = 1,\ b = -1,\ d = 1)$. The first row (a,b) is relative to a small sphere ($R = 10$ nm) and the second row (c,d) to a large sphere ($R = 150$ nm). In the first column (a,c) the pump wavelength is $\lambda = 520$ nm, while in the second column (b,d) $\lambda = 780$ nm.

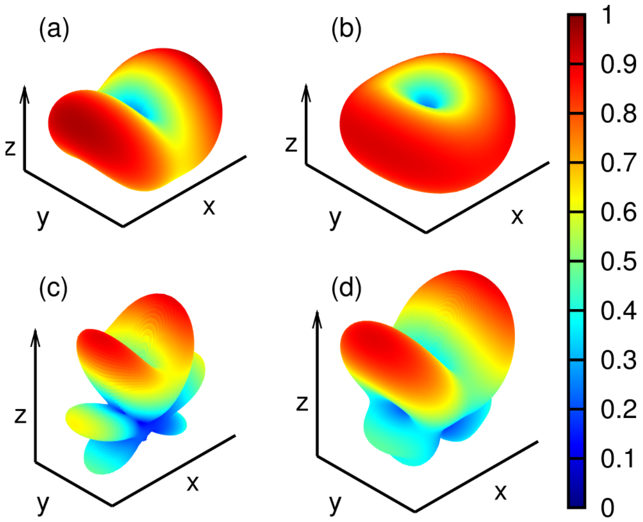

Figure 6.9: SH radiation diagrams for nanospheres of size $R = 10$ nm (panels a,b), $R = 150$ nm (panel c, d), obtained by using $(a = 1, b = -1, d = 1)$. Panels (a, c) are relative to the pump wavelength $\lambda = 520$ nm, and panels (b,d) to $\lambda = 780$ nm. All the intensities are normalized to their own maximum.

For particles with $R = 10$ nm, the dipolar and quadrupolar SH sources dominate the response, in agreement with the Rayleigh limit. In particular, we notice that the quadrupolar SH source is more important at $\lambda = 520$ nm, while at $\lambda = 780$ nm the dipolar mode fully dominates the response. As the particle radius increases, higher order modes come into play, resulting in an higher number of secondary lobes. For particles with $R = 150$ nm, the octupolar mode dominates the angular distribution of the SH radiation at $\lambda = 780$ nm. Moreover, for each particle size and pump wavelength, the lobes display a preferential alignment along the polarization direction of the pump field. Figure 6.10 shows the two cuts of the 3D radiation diagram along the xOz, and yOz plane. It is worth noting that the SH power vanishes in both the forward- and backward-scattering directions, regardless of R. This selection rule is a direct consequence of the rotational symmetry of the sphere around the propagation direction of the pump. Two lobes, directed orthogonally to the pump propagation direction, characterize the radiation diagrams of small particles. As the particle size increases, the lobes with higher power tend to come closer to the

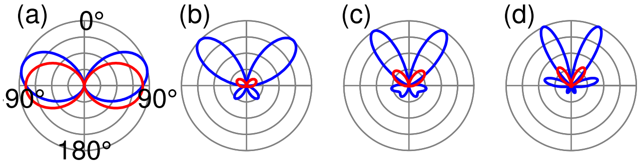

Figure 6.10: SH radiation diagrams as function of θ angle, at $\varphi = 0°$ (blue) and $\varphi = 90°$ (red), for nanospheres of size $R = 10\ \mathrm{nm}$ (a), $R = 100\ \mathrm{nm}$ (b), $R = 150\ \mathrm{nm}$ (c), and $R = 200\ \mathrm{nm}$ (d) and $(a = 1, b = -1, d = 1)$. The pump wavelength is $\lambda = 780\ \mathrm{nm}$, for each panel the curves are normalized to the maximum of the most intense one.

forward direction, while the lobes in the backward direction decrease in amplitude. The same trend is observed if the particle size is fixed and the pump wavelength decreases. This behavior has been already observed experimentally for silver nanoparticles in Ref. [119].

6.4 CONCLUSION

We have developed a full-wave analytical solution for the second-harmonic generation from a metal spherical particle of arbitrary size. This approach extends the existing theories, enabling a rigorous treatment of all the sources of SH radiation, located both on the surface and in the bulk of the particle.

The solution of the problem is derived in the framework of the Mie theory by expanding the pump field, the nonlinear polarization sources and the second-harmonic fields in series of spherical vector wave functions, and enforcing the boundary conditions at the sphere surface.

We investigated the SH radiation of gold nanospheres by using the Rudnick-Stern model for the SH sources. In particular, we studied the spatial distributions of the nonlinear polarization sources, which display significant symmetries due to the spherical geometry. We investigated the SH cross-section dependence on the pump wavelength, demonstrating the contribution of SH multipoles up to the order $N = 6$, as the particle radius increases up to $\sim 200\ \mathrm{nm}$. Similarly, we studied the multipolar origin of the SH radiation diagrams, and showed significant analogies with experimental works in literature. Eventually, we investigated the SH radiated power as function of the pump polarization angle. In particular, we compared the solutions obtained by using as Rudnick-Stern parameters both the Sipe's model values and the values proposed in Ref. [52]. It resulted that the SH radiation dependence on the pump polarization significantly varies with these parameters, and the shape and the relative intensities of the SH p- and s- components are function of them.

The application of the proposed method in combination with experimental observation, can improve the general understanding of nonlinear processes in metals, and can lead to an accurate evaluation of weights for the different SH sources. The theory of SH scattering can be easily extended to the multiparticle case. This approach can also guide the design of novel nanoplasmonic devices with enhanced SH emission for a wide range of applications,[120] including sensors for probing physical and chemical properties of material surfaces.

7

GOLD COLLOIDS

In recent years, several experiments were performed on the SH generation from noble metal surfaces and colloids [51, 52, 121], confirming the comparable magnitude of the nonlocal bulk and local surface SH sources. In the present Chapter, we estimate the relative contributions of the SH sources, by combining SH generation experiments on a set of differently-sized gold colloids and theoretical data of the SH scattering from gold nano-spheres.

SH-intensity measurements are performed on colloidal gold as function of the polarization state of the pump beam, in order to separate the contributions of even- and odd-order multipoles. The experimental data are analyzed in the framework of the hydrodynamic model combined with a full-wave electromagnetic solver for the SH scattering from spherical particles. Since the experimental setup allows for the selection of even- and odd-order SH multipoles, the natural choice for our calculation is the analytical solution of the problem of SH generation based on the expansion of the fields and the sources in SVWFs developed in the previous Chapter, taking into account both the nonlocal bulk and the local surface SH sources [122]. We observe a dependence of the surface contribution to the SH radiation on the particle size, and we measure the detailed transition in the SH dipolar and octupolar interference patterns.

An estimation of the relative weights of the bulk and the surface nonlinear sources has been proposed for single-sized gold nanoparticles in Ref. [52], by using a Finite Element Method (FEM) for the calculations, where the second-order bulk polarization $\mathbf{P}_b^{(2\omega)}$ has been expressed as:

$$\mathbf{P}_b^{(2\omega)} = \varepsilon_0 \gamma \nabla \left(\mathbf{E}^{(\omega)} \cdot \mathbf{E}^{(\omega)} \right) , \tag{7.1}$$

and the surface polarization has been expressed as:

$$\mathbf{P}_s^{(2\omega)} = \varepsilon_0 \overset{\leftrightarrow}{\chi}_s^{(2\omega)} : \mathbf{E}^{(\omega)} \mathbf{E}^{(\omega)} , \tag{7.2}$$

The parameters $\chi_{\perp\perp\perp}$, $\chi_{\parallel\perp\parallel}$ and γ have been expressed as:

$$\chi_{\perp\perp\perp} = -\frac{a}{4} \chi_b(\omega) \frac{\omega_p^2}{\omega^2} \frac{\varepsilon_0}{e n_0}, \tag{7.3a}$$

$$\chi_{\parallel\perp\parallel} = -\frac{b}{2} \chi_b(\omega) \frac{\omega_p^2}{\omega^2} \frac{\varepsilon_0}{e n_0}, \tag{7.3b}$$

$$\gamma = -\frac{d}{8} \chi_b(\omega) \frac{\omega_p^2}{\omega^2} \frac{\varepsilon_0}{e n_0}, \tag{7.3c}$$

where $\chi_b(\omega)$ is the metal linear susceptibility. The coefficients (a, b, d), usually referred to as *Rudnick-Stern (R-S)* parameters [42], represent the weight of the SH sources, respectively normal and tangent to the surface, and bulk, as previously discussed in the Thesis.

7.1 PUMP-POLARIZATION MEASUREMENTS

We perform SH generation experiments in the configuration represented in Fig. 7.1. The gold colloid, symbolically represented as a spherical particle, is excited by a pulsed Ti:Sapphire laser (Mai Tai HP, Spectra Physics), propagating along the z-axis. The pulse width is 120 fs, with a repetition rate of 80 MHz. We perform the experiments at the two incident wavelengths $\lambda = 800$ nm and $\lambda = 840$ nm, with linearly-polarized light. The pump beam polarization $\boldsymbol{E}_0^{(\omega)}$ is rotated in the xOy plane, where α is the angle formed with the x-axis. The beam is focused onto the colloidal solution through a 20x microscope objective. We measure the SH intensity along the x-axis, i. e. the excitation and the collection directions are at right angle. The signal is collected by a 30 mm lens and it is filtered by a 650 nm short-pass filter to reduce the intensity of the scattered pump frequency. Eventually, it passes through a monochromator and is detected by a photomultiplier tube. A lock-in amplifier extracts the signal modulated by a mechanical chopper. This excitation-collection configuration has the remarkable property to allow for the separation of the SH intensity generated from different SH multipoles. In particular, the collected SH intensity is analyzed in its p- and s-components with respect to the xOz scattering plane, respectively along the z-axis and the y-axis. The odd-order multipoles only contribute to the p-component (along the y-axis) of the SH signal, whereas the even-order multipoles only contribute to the s-component (along the z-axis) [122].

We perform SH intensity measurements on a set of gold colloids (BBI Life Sciences) with average radii ranging from $R = 40$ nm to $R = 100$ nm, by varying the polarization angle α of the pump beam. The pump-polarization dependence of the SH p- and s-components are represented in Fig. 7.2 for two pump wavelengths, respectively $\lambda = 800$ nm and $\lambda = 840$ nm. For the cases of interest of the present work, it turns out that the non-negligible SH multipoles are the dipole $(n = 1)$ and octupole $(n = 3)$ for the SH p-component, and the quadrupole $(n = 2)$ for the s-component. The SH radiation from higher-order multipole is negligible, as demonstrated by rigorous analytical calculations in the following.

The pump-polarization dependence of the SH p-component is determined by the interference between the SH dipole and octupole. On the contrary, the pump-polarization dependence of the SH s-component is only dominated by the SH quadrupole, and no interference appears. The relative intensity between the maxima of the p- and s-

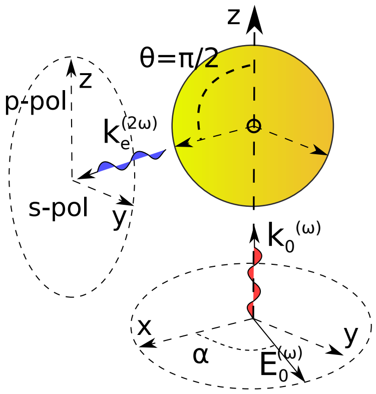

Figure 7.1: Schematic of the experimental setup. The pump beam $k_0^{(\omega)}$ propagates along the z-axis, and it is linearly-polarized in the xOy plane (α is the angle between the x-axis and the electric field $\boldsymbol{E}_0^{(\omega)}$. The signal is collected along the x-axis and its p- and s-components, with respect to the scattering plane xOz, are analyzed.

components are function of the particle size. For $R = 40$ nm, the p-component prevails over the s-component for $\lambda = 840$ nm, and they are of comparable magnitude for $\lambda = 800$ nm. For $R = 50$ nm, the destructive interference between the SH dipole and octupole reduces the intensity of the p-component with respect to the previous particle size. The minimum of SH intensity for the p-component occurs for $R = 75$ nm, where the s-component prevails for both pump wavelengths. Eventually for $R = 100$ nm, the SH octupole begins to prevail over the dipole. The interference between the two multipoles still occurs, and the p-component has it maxima for $\alpha = 0$ and $\alpha = \pi/2$ (p- and s-polarized pump). For both cases $\lambda = 800$ nm and $\lambda = 840$ nm, the shape of the SH p-component as function of the pump-polarization angle α is given by the interference between the SH dipole and octupole. Moreover, the relative intensities of the p- and s-components significantly vary with λ.

In the small-particle limit (i. e. $R << \lambda/2\pi$), the p-component is governed by the SH dipole, resulting in a SH intensity independent of the pump-polarization angle α [61]. In 2010 Bachelier *et al.*observed the interference between the SH dipole and octupole for particles of size $R = 150$ nm [123]. In the previous Chapter we predicted, by using the *R*-*S* parameters derived from the hydrodynamic model, that the SH dipole-octupole interference would provide a variety of patterns in the p-component α-dependence, strongly depending on the particle size. In particular, we guessed the appearance of two maxima at $\alpha = 0$ and $\alpha = \pi/2$. In the present Chapter, we show a significant part of the transition between the pure dipolar and octupolar α-dependence in Fig. 7.4, and we confirm the previous predictions about the SH p-component maxima located at $\alpha = 0$ and $\alpha = \pi/2$.

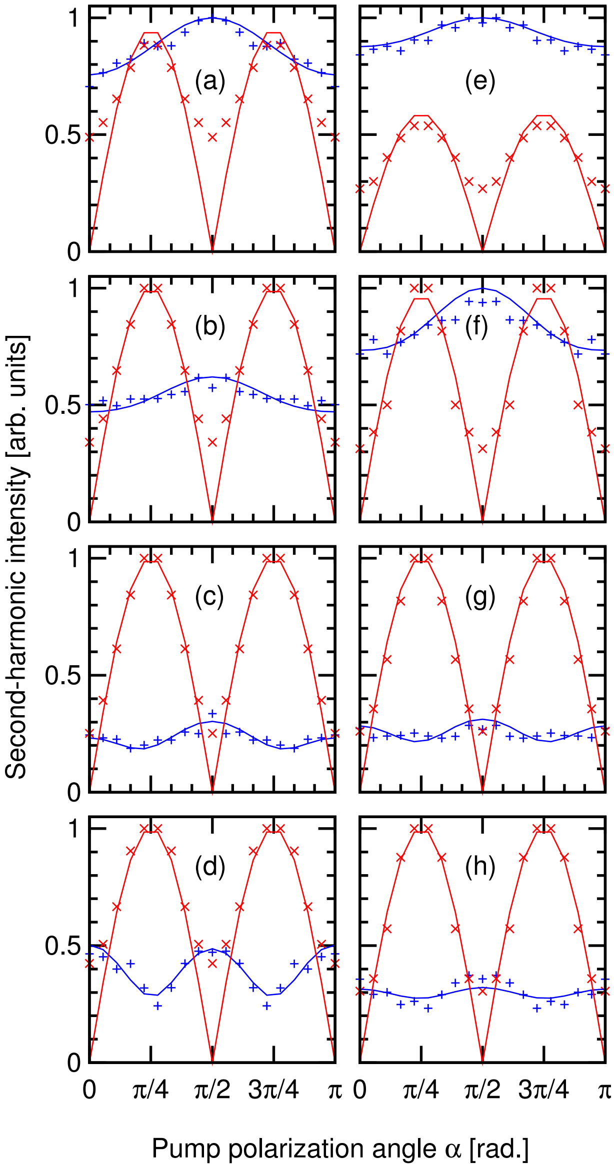

Figure 7.2: Intensity of the SH p- (blue) and s- (red) components as function of the angle of polarization of the pump beam α, for $R = 40\ \mathrm{nm}$ (a,e), $R = 50\ \mathrm{nm}$ (b,f), $R = 75\ \mathrm{nm}$ (c,g) and $R = 100\ \mathrm{nm}$ (d,h). The pump wavelengths are $\lambda = 800\ \mathrm{nm}$ (left column) and $\lambda = 840\ \mathrm{nm}$ (right column). The curves in each panel are normalized to the maximum of the most intense component. Points are experimental acquisition and lines are numerical data.

7.2 NUMERICAL ANALYSIS

In order to estimate the relative contributions of the SH nonlinear sources, we study the pump-polarization dependence of the SH intensity in the framework of the full-wave analytical solution for the problem of SH generation from gold nano-spheres, developed in the previous Chapter. In particular, this approach allows us to calculate the SH power per unit solid angle $\frac{dP^{(2\omega)}_{\hat{\varepsilon}^*}(\hat{\boldsymbol{x}})}{d\Omega}$, radiated along the x-axis and collected through an analyzer with polarization state $\hat{\varepsilon}^* = \hat{\boldsymbol{z}}$ (SH p-component) and $\hat{\varepsilon}^* = \hat{\boldsymbol{y}}$ (SH s-component):

$$\frac{dP^{(2\omega)}_{\hat{\varepsilon}^*}(\hat{\boldsymbol{x}})}{d\Omega} = \lim_{r\to\infty} \frac{\left|rE_c^{(2\omega)}\right|^2}{2\zeta_e} \left| \hat{\varepsilon}^* \cdot \sum_{n=1}^{N} \sum_{m=-n}^{n} b_{mn}^{(2\omega)} \mathbf{M}_{mn}^{(3)} \left(k_e^{(2\omega)} r, \theta = \frac{\pi}{2}, \phi = 0\right) \right.$$
$$\left. + a_{mn}^{(2\omega)} \mathbf{N}_{mn}^{(3)} \left(k_e^{(2\omega)} r, \theta = \frac{\pi}{2}, \phi = 0\right) \right|^2 ,$$

where (r, θ, ϕ) are spherical coordinates having origin in the sphere center, $k_e^{(2\omega)}$ and ζ_e respectively are the wavevector and the impedance of the external medium, $E_c^{(2\omega)}$ is a characteristic electric field expressing the order of magnitude of the SH electric field in the nanoparticle, and N is the maximum order of SVWF used.

Our calculations are done by setting $N = 10$, but it turns out that only the SVWFs with $n = 1, 2, 3$ are significant for the investigated particle size and incident wavelength. The SH scattering coefficients $a_{mn}^{(2\omega)}, b_{mn}^{(2\omega)}$ are function of the incident field wavelength λ and polarization angle α, and of the particle size and permittivity, as discussed in the previous Chapter.

The combination of the SH generation experiments and calculations allows us to evaluate the *R-S* parameters. Specifically, we proceed by minimizing the Root-Mean-Square Deviation (RMSD) between experimental and theoretical curves of the pump-polarization dependence in the configuration described in Fig. 7.1. Numerical data are shown in Fig. 7.2 with solid lines. The experimental setup allows for the measurement of the relative intensities of the two SH components, but not their absolute values. Consequently, the constraints for the minimization problem are two, while the degrees of freedom are the three real parameters (a, b, d). For the sake of the well-conditioning of the problem, we fix one of the *R-S* coefficients to an arbitrary value. In particular, we lead our analysis by imposing $d = 1$ for each particle size. As a matter of fact, d is predicted to be unitary in the hydrodynamic model that we adopt for the expression of the nonlocal bulk and local surface susceptibilities. This choice allows for the parameters a and b to vary with the particle size.

The estimation of the *R-S* parameters given by Bachelier *et al.*with FEM calculations, by considering the SH p-component of gold particles with radius $R = 75$ nm and an incident wavelength $\lambda = 800$ nm

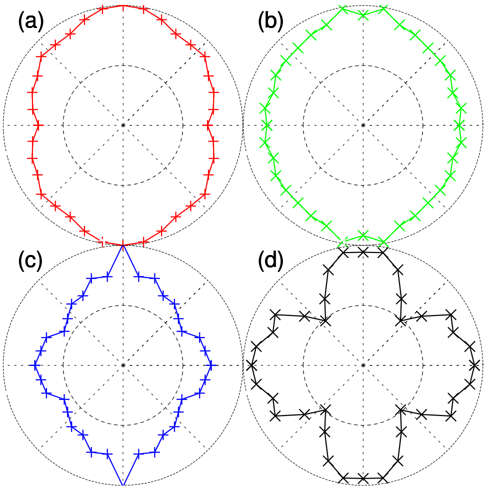

Figure 7.3: Intensity of the SH p-component as function of the angle of polarization of the pump beam α, for $R = 40\ \mathrm{nm}$ (a), $R = 50\ \mathrm{nm}$ (b), $R = 75\ \mathrm{nm}$ (c) and $R = 100\ \mathrm{nm}$ (d). The pump wavelength is $\lambda = 800\ \mathrm{nm}$. Curves are not to scale.

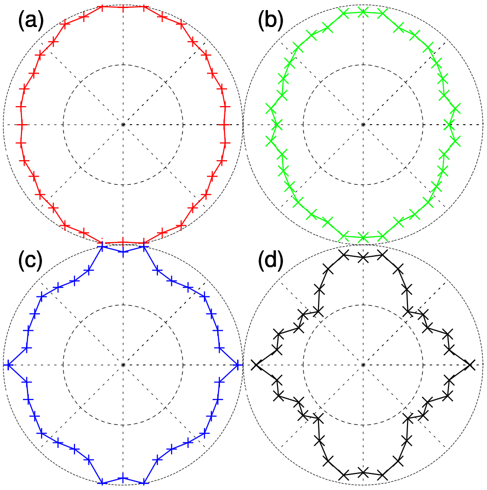

Figure 7.4: Intensity of the SH p-component as function of the angle of polarization of the pump beam α, for $R = 40\ \mathrm{nm}$ (a), $R = 50\ \mathrm{nm}$ (b), $R = 75\ \mathrm{nm}$ (c) and $R = 100\ \mathrm{nm}$ (d). The pump wavelength is $\lambda = 840\ \mathrm{nm}$. Curves are not to scale.

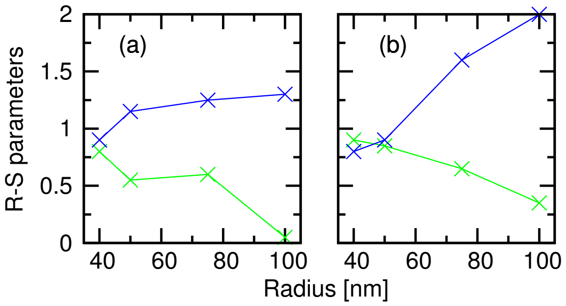

Figure 7.5: Estimated relative values of the Rudnick-Stern parameters a (blue) and b (green) as function of the gold nano-particle size. The pump wavelengths are $\lambda = 800$ nm (a) and $\lambda = 840$ nm (b).

[52], provided the optimal set of values $(d = 1,\ b = 0.1, a = 0.5 + i0.2)$. Our works are in agreement on the observation that the *R-S* parameters related to Sipe's model are unable to predict the experimental SH dependence on the pump-polarization. However, their estimated values of the *R-S* parameters are different from the results derived here. In particular, in our work we use real-valued R-S parameters for the sake of the well-conditioning of the problem, as previously discussed. Moreover, our estimation of the relative weights of the SH sources is done by minimizing the RMSD of both the p- and s-components. Therefore, we account for both the p- and s-components with the same *R-S* parameter set, for each particle size. Eventually, we believe that the SH experiments, allowing for the separation of the SH multipoles, are more accurately described by numerical calculations based in a multipole expansion of the fields and the sources, rather than other approaches.

Figure 7.5 shows the calculated *R-S* parameters as function of the particle size, and a clear trend for their relative contributions can be observed. The parameters a and b, representing the weights of the surface contributions respectively normal and tangent to the surface with respect to the bulk source, vary with the particle radius R. This result is expected since the surface condition also varies with the particle size. For the smallest investigated size $R = 40$ nm, the *R-S* parameters are approximately of unitary amplitude. As the particle size increases, a increases whereas b decreases. Eventually, for the largest investigated size $R = 100$ nm, b is almost zero for both wavelengths. On the contrary, at $\lambda = 800$ nm a as slightly increased its value. At $\lambda = 800$ nm, a is almost the double of d. These results are a confirmations of the strong dependence of the selvedge effects on the surface conditions [42]. It is clear that the expression for the *R-S* parameters derived in the hypothesis of translational symmetry are not able to account for effects taking place in the selvedge region due to the finite size of the particle. Our experiments suggest that multipolar effects in the selvedge neglected so far are responsible for the variation of the SH sources relative magnitude.

7.3 CONCLUSION

In conclusion, we evaluated the relative magnitude of the nonlocal bulk and local surface contributions to the SH generation from differently-sized gold colloids, in the framework of the hydrodynamic model for the conduction electrons. Both surface terms, normal and tangent to the surface, are found to be strongly dependent on the particle size. We measured novel interference patterns between the SH dipole and octupole in the SH intensity. This study has explored the possibility to model the nonlinear response of metal nanostructures in the framework of the hydrodynamic model. It indicates the need for a proper treatment of nonlinear effects from curved surfaces, in order to rigorously understand second-order nonlinear effects from metal nanostructures.

8

PLANAR ARRAYS OF AU NANOPARTICLES

In the last decade, the SH generation from planar arrays of metal nanoparticles has been investigated for a variety of particle shapes, sizes, and under different excitation-collection and polarization conditions [124, 125, 126, 127, 128, 29]. In order to maximize the intensity of the SH generation from a planar array, the particle shape, the interparticle separations and the array geometry must be designed to excite the LSPs at the fundamental wavelength, producing strong near-field enhancement. This is due to the fact that the intensity of the SH generation signal grows with the square of the intensity of the local electric field at the pump wavelength.

In addition, the particle shape plays a fundamental role due to symmetry selection rules governing the SH generation [39]. For example, L-shaped particles have been specifically studied to remove single particle centrosymmetry. In this case, the linear and nonlinear optical behavior is strongly dependent on the polarization state of the excitation [124, 125].

In 1999 Lamprecht et al. demonstrated that the SH generation signal from arrays of L-shaped particles can be greatly increased if the particles are oriented in such a way that the overall array is non-centrosymmetric [124]. Canfield *et al.*investigated SH generation from non-centrosymmetric dimers, demonstrating that the asymmetry of the local electric field distribution over the entire array plays a role in SH generation as important as the enhancement of the near-field intensity at the pump frequency [29]. Angularly resolved studies of the SH generation from discontinuous metal percolation films also featured strong peaks of SH signal in the direction of specular reflection, as well as a diffuse scattering background [129]. However, the role of the planar array geometry on the SH generation from metal nanoparticles is not yet fully understood.

Deterministic aperiodic nanostructures (DANS) have been shown to exhibit distinctive scattering properties associated to the increased localization of photonic-plasmonic modes, such as broadband scattering resonances, enhanced near-field intensities, largely controllable angular scattering, enhanced colorimetric responses and Raman cross-sections employed for biosensing applications [130, 131, 132, 133]. Recently, DANS lacking both translational and rotational symmetry, consisting of aperiodic Vogel spirals of metal nanoparticles, have also been demonstrated to exhibit polarization-insensitive light diffraction and distinctive photonic modes carrying discrete values of optical angular momentum [134, 135, 136].

In this Chapter, we investigate the role of the array geometry on the intensity and on the polarization properties of the SH generation from metal nano-cylinders arranged in planar structures of progressively increasing complexity. In particular we focus on periodic, quasi-periodic Fibonacci and aperiodic golden angle spiral arrays in the nonlinear optical regime. Detailed studies on the Fibonacci and golden angle spiral geometries as well as their linear scattering properties have been discussed in literature [130, 131, 132, 133, 134, 135, 136].

We demonstrate optical SH generation in planar arrays of cylindrical Au nanoparticles arranged in periodic and deterministic aperiodic geometries. In order to understand the respective roles of near-field plasmonic coupling and long-range photonic interactions on the SH generation signal, we systematically vary the interparticle separation from 60 nm to distances comparable to the incident pump wavelength. Using polarization-resolved measurements under femtosecond pumping, we demonstrate multipolar SH generation signal largely tunable by the array geometry. Moreover, we show that the SH generation signal intensity is maximized by arranging Au nanoparticles in aperiodic spiral arrays[1] .

The possibility to engineer multipolar SH generation in planar arrays of metal nanoparticles paves the way to the development of novel optical elements for Nanophotonics, such as nonlinear optical sensors, compact frequency converters, optical mixers, and broadband harmonic generators on a chip.

---

[1] The figures in the present Section have been adapted with permission from Ref. [105]. Copyright (2012) Optical Society of America

8.1 ARRAY DESIGN AND FABRICATION

We investigate SH generation in periodic, Fibonacci and golden angle spiral arrays of cylindrical gold nanoparticles with a height of 30 nm and a diameter of 200 nm. The dimensions of the gold nanocylinders have been chosen in such a way that the peak of the scattered pump signal is overlapping the pump wavelength (i.e., 780 nm) in the absence of interactions among cylinders. The T-matrix numerical method has been employed for electromagnetic scattering calculations [137, 138], assuming a perfect cylindrical shape.

We fabricate a set of samples on a transparent fused silica substrate by EBL (see Appendix A.8). For each sample, a 180 nm-thick PMMA (poly(methyl methacrylate)) film is first spin-coated onto the substrate, and then soft-baked at 180°C for 20 minutes. The PMMA film is nanopatterned by EBL. A 2 nm Cr adhesion layer and a 30 nm gold layer are deposited over the PMMA film by electron beam evaporation. Finally the sample is immersed in heated acetone for the lift-off process. Each array has a circular shape with a diameter of 50 μm. In order to explore both the short-range plasmonic and long-range photonic coupling regimes, we consider arrays with edge-to-edge interparticle separations L ranging from 60 nm to 650 nm. For periodic and Fibonacci arrays the interparticle separation is defined as the minimum edge-to-edge particle separation, while for the golden angle spirals it is defined as the average nearest neighbor edge-to-edge separation, as discussed in Ref. [134, 135]. In Fig. 8.1 we show the SEMs of periodic (a), Fibonacci (b) and golden angle spiral (c) arrays with an interparticle separation of 60 nm.

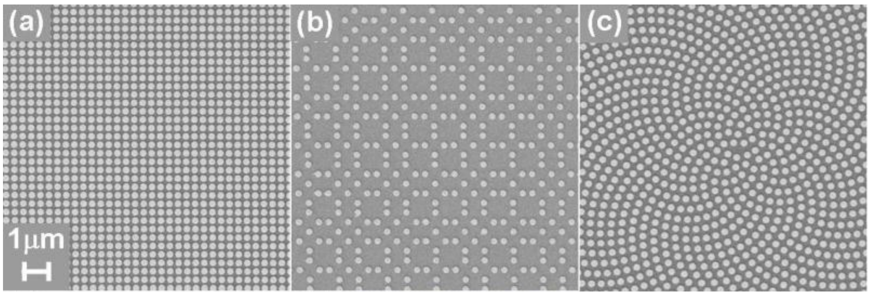

Figure 8.1: SEM micrographs of periodic (a), Fibonacci (b) and golden angle spiral (c) arrays of 200 − nm-diameter cylindrical gold nanoparticles with a separation of 60 nm.

8.2 DARK-FIELD CHARACTERIZATION

Prior to the SH generation experiments, we characterize the linear behavior of each fabricated array by measuring their dark-field scattering spectra over the wavelength range $\lambda = 400\ \mathrm{nm} - 900\ \mathrm{nm}$.

Dark-field spectroscopy consist of illuminating a sample with visible light and of collecting the scattered light only. The transmitted light is not involved in the collection. This can be accomplished both in transmission and reflection configurations, and it makes use of a high NA condenser and a pinhole for the excitation. An index-matching fluid can be possibly used to couple the condenser to the sample substrate. This configuration avoids low k-vectors to illuminate the sample, and only high k-vectors pass through. A low NA (high magnification) objective is used in the collection. The background scattering spectra of an unpatterned area is subtracted by the measured spectra. Then, the resulting spectra are normalized to the emission line shape of the excitation lamp.

In our experiments, we use a broadband halogen lamp, a 50x objective with 0.5 NA and a fiber coupled CCD spectrometer (Ocean Optics QE65000). Dark-field scattering spectra are plotted in Fig. 8.2 for the three array geometries and for different interparticle separations L. In periodic arrays (Fig. 8.2(a)) we notice that for values of L larger than the particle size (yellow, cyan, magenta and blue curves) the scattering resonance peak blue-shifts if L decreases due to photonic (i.e., diffractive) coupling among the nanoparticles. Conversely, for values of L comparable to the particle size (green and red curves), the quasi-static near-field interaction among closely spaced particles prevails over the photonic one, and a broad resonance towards the near-infrared is observed. We refer to this regime as plasmonic coupling. In contrast, Fibonacci arrays (Fig. 8.2(b)) exhibit a broader scattering peak around 800 nm with no remarkable shift as the interparticle separation L is varied. This scattering behavior is consistent with the inhomogeneous spatial distribution of nanoparticle dimers in Fibonacci arrays, that leads to a more incoherent scattering response largely insensitive to L [130, 131, 132, 133]. Interestingly, the scattering behavior of the golden angle spiral arrays (Fig. 8.2(c)) is similar to the one of periodic structures. In particular, the golden angle spiral array features well distinct photonic and plasmonic resonances, similar to periodic arrays. In fact it has recently been shown that these structures display local order, captured by oscillations in the particles radial correlation function and by a well-defined scattering ring in Fourier space [135]. In Fig. 8.2(d) we show the behavior of the scattered intensity at 780 nm, later utilized as the pump wavelength in the pulsed SH generation experiments, versus the interparticle separation for the different array geometries. In the case of periodic arrays (red squares), the highest value of the scattered intensity occurs at L = 611 nm, corresponding to a center-to-center interparticle distance of 811 nm. This resonance may be associated with surface plasmon coupling with the grating periodicity [139, 140]. Golden angle spiral arrays (blue circles) show a trend similar to that observed for periodic arrays. On the contrary, the linear scattering from Fibonacci arrays (green triangles) is almost insensitive to variations in L, consistently with its more incoherent nature. The increase in scattering signal when decreasing the interparticle separations in a Fibonacci arrays reflects the increase in the particle number.

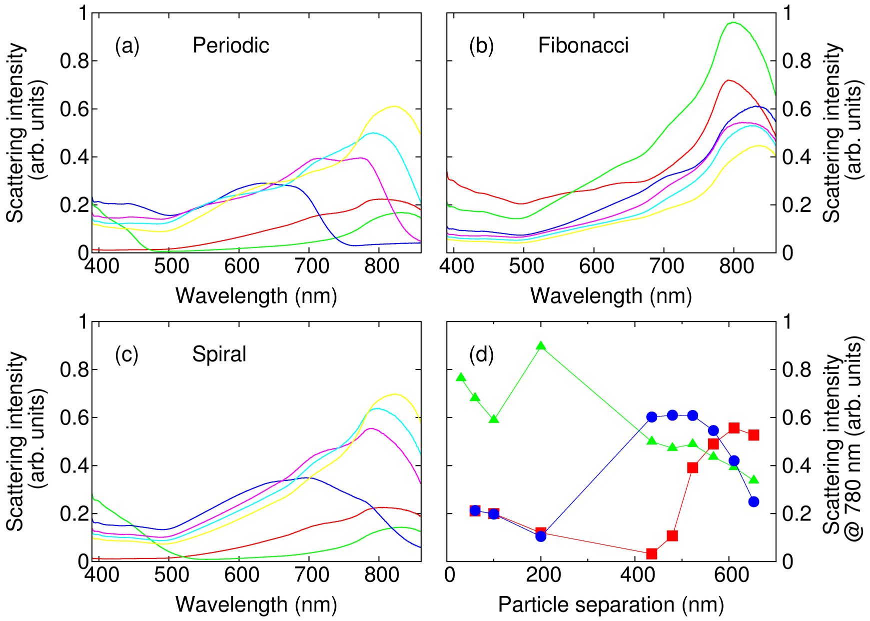

Figure 8.2: Dark-field scattering spectra for periodic (a), Fibonacci (b) and golden angle spiral (c) arrays with different interparticle separation L: 60 nm (red), 200 nm (green), 436 nm (blue), 523 nm (magenta), 567 nm (cyan), 653 nm (yellow). (d) Dark-field scattering intensity at $\lambda = 780$ nm for periodic (red squares), Fibonacci (green triangles) and golden angle Spiral (blue circles) arrays, as function of the particle separation L.

8.3 PUMP POWER DEPENDENCE

The SH generation from the three array geometries is studied by exciting the samples at 780 nm with a femtosecond Ti:Sapphire pulsed laser (Mai Tai HP, Spectra Physics), with a pulse width of 120 fs and repetition rate of 80 MHz, which is reduced to 10 MHz by an electro-optic pulse picker (Conoptics 360-80l). The laser beam is filtered by a 700 nm long-pass filter and has an average power of 40 mW. We utilize the specular reflection configuration shown schematically in Fig. 8.3(a). The excitation is obliquely incident on the sample surface at an angle $\phi = 45°$ and the reflected SH generation signal is collected. The beam is focused onto the array by an 85 mm focal length spherical lens. The signal is collected through a 50x microscope objective with a numerical aperture $NA = 0.5$ and is detected by a Newport 77348 photomultiplier tube (PMT) after passing through a monochromator (Cornerstone 260 1/4 m Triple Grating, Ruled, 1200 l/mm, 500 nm Blaze, 280 nm – 1600 nm Primar). A lock-in amplifier (Oriel Merlin) extracts the signal modulated by a mechanical chopper. The collected signal is filtered by a 650 nm short-pass filter before the PMT in order to reduce the intensity of the pump component at the detector.

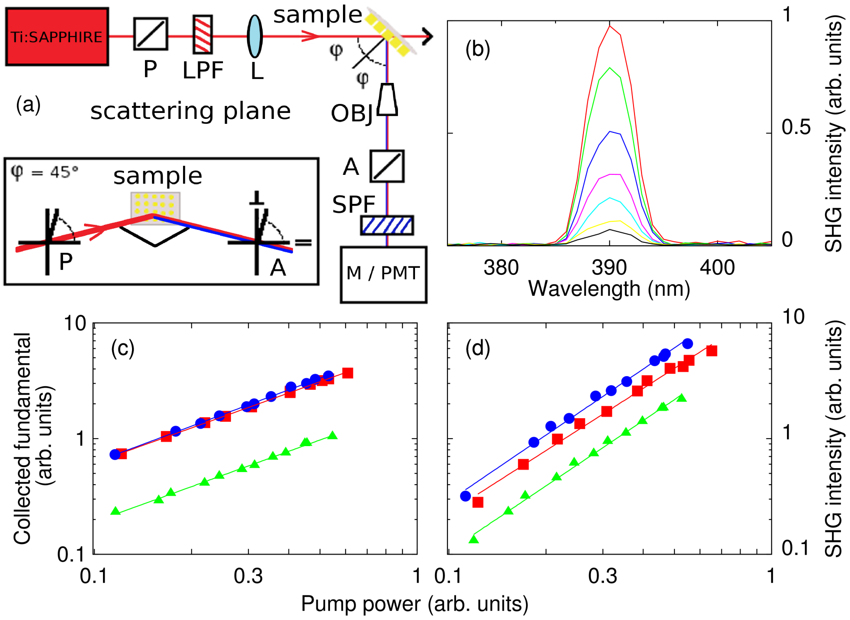

Figure 8.3: Schematics of the excitation-collection configuration (a). Spectra of SH generation (b) from arrays with interparticle separation of 60 nm, for several pump power densities W/W_{max}: 1 (red), 0.821 (green), 0.654 (blue), 0.525 (magenta), 0.402 (cyan), 0.290 (yellow), 0.213 (black). Collected intensities at pump wavelength (c, $\lambda = 780\mathrm{nm}$) and SH generation wavelength (d, $\lambda = 390\mathrm{nm}$), as function of the pump power intensity, for periodic (red squares), Fibonacci (green triangles) and golden angle spiral (blue circles) arrays with interparticle separation of 60 nm. Scales are logarithmic.

We measure the intensity of the collected signal both at the pump wavelength and at the SH generation wavelength (i.e., 390 nm). Fig. 8.3(b) shows representative SH generation spectra from arrays with interparticle separation $L = 60$ nm, as a function of the pump power density W normalized to the maximum pump power (W_{max}). We operate with $W_{max} \approx 2kWcm^2$ in order to preserve the particle structure and to avoid sample damaging. Fig. 8.3(c) and 8.3(d) show the intensity of the collected signals, at the pump and at the SH generation wavelength respectively, versus the pump power intensity for periodic (red squares), Fibonacci (green triangles) and golden angle spiral (blue circles) arrays with interparticle separation of 60 nm. A linear fit in a log-log scale indicates a slope ≈ 1 for the scaling of the fundamental signal and ≈ 1.8 scaling for the SH generation signal. A quadratic dependence of the SH generation signal on the pump power is the hallmark of a second order nonlinear process. We attribute the small discrepancy from the expected quadratic dependence to thermal effects in gold nanoparticles well below the melting point [127].

8.4 POLARIZATION DEPENDENCE OF THE SH GENERATION

The contribution of multipolar sources to SH generation can be recognized by their far-field emission. In what follows, we investigate the polarization properties of the second harmonic radiation with the aim of demonstrating its multipolar nature for the three planar array geometries [110, 141, 142, 123, 143, 59]. It was recently predicted that multipolar SH generation signal is more sensitive than the fundamental one for sensing applications [143]. We consider the components of the collected signal that are parallel and orthogonal to the scattering plane, defined by the directions of excitation and collection (inset of Fig. 8.3(a)). We measure the intensities of the two polarization components at the SH generation wavelength as a function of the input polarization angle of the pump beam through a polarizer/analyzer pair. A zero angle corresponds to a polarization parallel to the scattering plane. Following Brevet et al. [141, 142, 123], the experimental data are fitted using Eq. (8.1), where a, b and c are real parameters.

$$I(\gamma) = a\cos^4(\gamma) + b\cos^2(\gamma)\sin^2(\gamma) + c\sin^4(\gamma) \tag{8.1}$$

In Fig. 8.4(a) and 8.4(b) we show the intensities of the parallel and orthogonal components for the SH generation signal of periodic and golden angle spiral arrays, while Fig. 8.4(c) and 8.4(d) display the results of the Fibonacci array. We notice in Fig. 8.4(a) and 8.4(c) that the polar plots of each parallel component do not exhibit the typical patterns of a dipolar source, which is insensitive to the angle of polarization of the pump [110, 141, 142, 123]. This can be more clearly appreciated by the fact that, if using $2a = 2c = b$ in Eq. (8.1) as required for the parallel component of a dipolar source, we cannot fit the experimental data in Fig. 8.4. Hence, higher order multipolar contributions need to be considered due to symmetry breaking and retardation effects, which are particularly relevant for non-spherical particles in the investigated size regime.

On the other hand, a quadrupolar SH generation behavior is displayed by the orthogonal component for the Fibonacci array in Fig. 8.4(d), which can only be fitted when $a, c << b$. This is expected since for a pure quadrupolar source $a = c = 0$. To the best of our knowledge, this is the first time that a quadrupolar radiation patterns has been directly measured in the SH generation signal from planar arrays of metal nanoparticles. The polar plot in Fig. 8.4(d) is similar to the behavior of the orthogonal component of the SH generation measured in systems of non-interacting spherical nanoparticles [110, 141, 142, 123]. On the contrary, the photonic interactions among particles radically modify the SH generation radiated from periodic and golden angle spiral arrays. For these array geometries, the polarization patterns of the orthogonal components (Fig. 8.4(b)) are different from a pure quadrupole, and high order multipolar SH generation

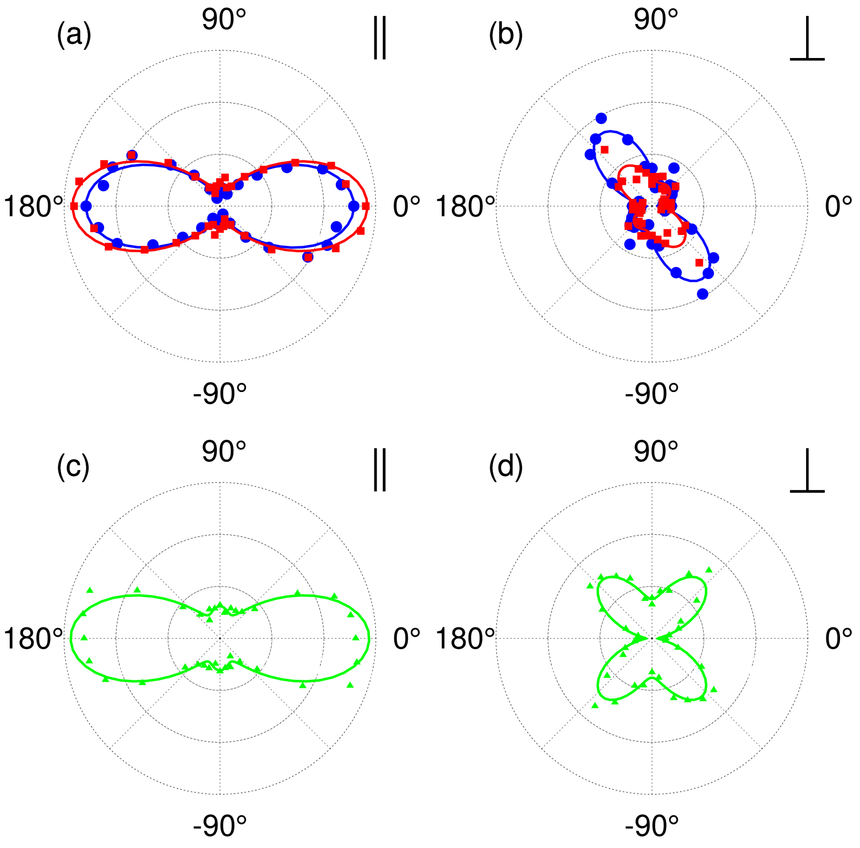

Figure 8.4: Parallel (a) and orthogonal (b) components of the SH generation for periodic (red) and spiral (blue) arrays. Parallel (c) and orthogonal (d) components of the SH generation for the Fibonacci array (green). Experimental data is with scattered symbols, least-squares fit is with continuous lines. The intensities in the plots of panel (a) have been reduced of the factor 11/4 for the sake of clearness.

is observed [142, 123]. In fact, Eq. (8.1) does not fit the experimental data for any value of the parameters, and a modified version must be introduced as in Ref. [141, 142]:

$$\begin{aligned} I(\gamma) = a\cos^4(\gamma) + b\cos^2(\gamma)\sin^2(\gamma) + c\sin^4(\gamma) + \\ d\cos^3(\gamma)\sin(\gamma) + e\cos(\gamma)\sin^3(\gamma) \end{aligned} \tag{8.2}$$

The quadrupolar SH generation polarization dependence displayed by Fibonacci quasi-periodic arrays with respect to periodic ones and golden angle spiral structures may reflect the different linear scattering behavior displayed at the fundamental frequency, as discussed in the previous Section. The values of the parameters a, b, c, d and e utilized to fit the experimental data are displayed in Table 8.1.

GEOMETRY	COMPONENT	A	B	C	D	E
Periodic	parallel	0.210	0.622	2.371	-	-
Fibonacci	parallel	0.206	-0.025	0.957	-	-
Spiral	parallel	0.371	0.501	2.610	-	-
Periodic	orthogonal	0.228	1.219	0.035	0.587	0.040
Fibonacci	orthogonal	0.252	1.642	0.038	-	-
Spiral	orthogonal	0.184	0.660	0.073	0.181	0.095

Table 8.1: Fitting Parameters.

8.5 DEPENDENCE ON THE INTERPARTICLE SEPARATION

The intensity of the SH generation is plotted as a function of the interparticle separation L for all the arrays in Fig. 8.5(a). A clear dependence of the SH generation signal on the interparticle distance L is observed, and the largest L produces the weakest SH generation response for each array geometry.

Moreover, we notice that golden angle spirals give rise to the most intense SH generation signals for all the investigated values of interparticle separations. On the other hand, for Fibonacci arrays the SH generation is the lowest for all separations. This can be attributed to the lower particle filling fraction of Fibonacci arrays. The variation in the particle filling fraction of all the arrays as a function of the interparticle separation is shown in the inset of Fig. 8.5(a). Furthermore, we notice that the superior performances of golden angle spirals over periodic arrays cannot simply be explained by the difference in particle filling fractions, as these are comparable across the investigated range of separations. Therefore, we attribute the enhanced SH generation to the asymmetric spatial near-field distribution in golden angle spiral arrays, which is a consequence of their distinctive spiral aperiodic order. The importance of the near-field intensity distribution at the pump wavelength for the SH generation optimization was already pointed out by Canfield et al. in the case of asymmetric metal nanoparticles [29].

In Fig. 8.5(b) we show a correlation between the intensities of the SH generation signal and of the scattered pump at 780 nm. A direct dependence of SH generation signal on the fundamental is demonstrated, showing that the SH generation is mainly driven by the optical behavior of the particle arrays at the pump frequency. In general, the SH generation process depends also on the particle array field distribution at the harmonic frequency, but in this case the strong absorption of gold at the SH generation frequency makes this dependence negligible. In order to better understand the role of the asymmetry of the spatial distributions of the pump field over the nanoparticle, we

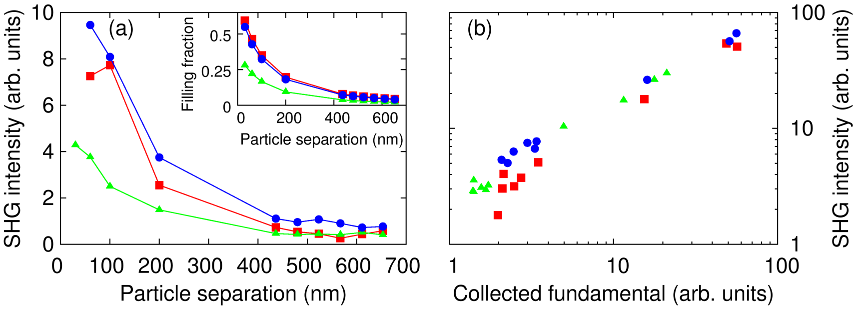

Figure 8.5: SH generation intensity (a) as a function of the interparticle separation L, for periodic (red squares), Fibonacci (green triangles) and golden angle Spiral (blue circles) arrays; (a inset) filling fraction of gold for periodic (red squares), Fibonacci (green triangles) and golden angle Spiral (blue circles) arrays. Correlation diagram between SH generation and pump collected signals (b).

show in Fig. 8.6 the calculated near-field patterns at 780 nm, obtained by the multiparticle Mie theory, introduced in Chapter 3 [54].

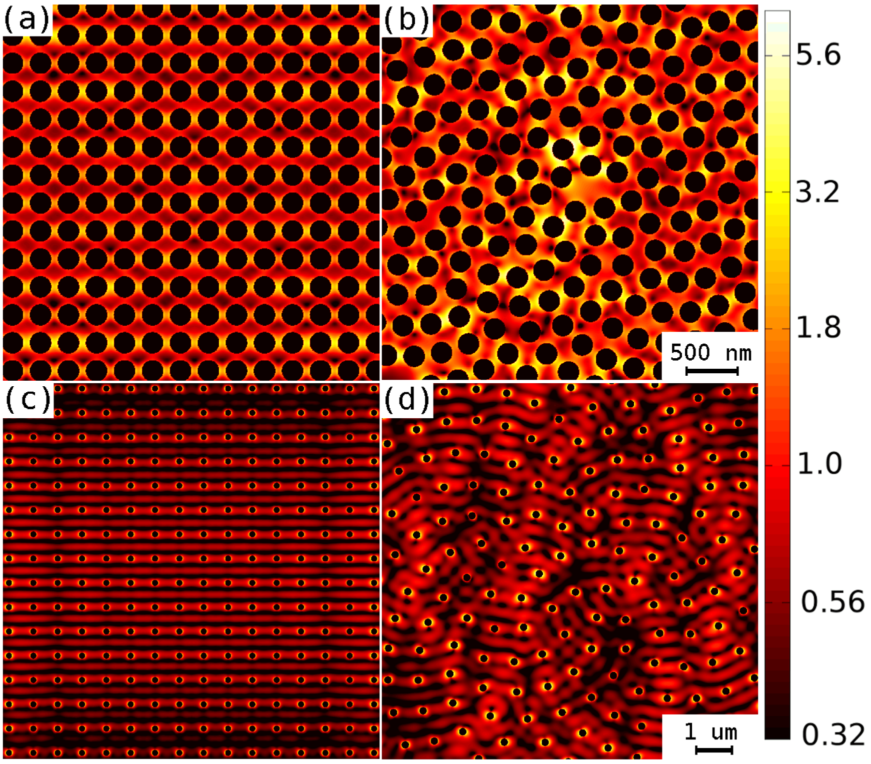

Figure 8.6: Near-field distribution at the pump frequency over periodic (a) and golden angle spiral (b) arrays with interparticle separation $L = 60$ nm. Near-field distribution at the fundamental frequency over periodic (c) and golden angle spiral (d) arrays with interparticle separation $L = 611$ nm. All the near-field maps are plotted in logscale.

The pump fields are calculated in the plane of the arrays for all the array geometries and for two particle separations (60 nm, 611 nm) characteristic of plasmonic near-field coupling and photonic coupling, respectively.

Fig. 8.6(a) and 8.6(c) show that periodic arrays display a very regular distribution of near-field around each nanoparticle, and the local field intensity is reduced as the particles are separated. Moreover, we notice that the field is strongly oriented along the direction of polarization of the pump beam. The highly symmetric nature of the near-field pump distribution in periodic plasmonic arrays reduces the SH generation signal due to destructive interference [144, 124]. In Fig. 8.6(b) and 8.6(d), we show the near-field distributions in golden angle spiral arrays for the photonic and plasmonic coupling regimes, respectively. The golden angle spiral geometry couples all the particles in the array but, differently from periodic structures, a very asymmetric near-field distribution results from the distinctive aperiodic order. This asymmetry of the pump fields in the golden angle spirals prevents destructive interference effects in the SH generation for all interparticle separations, resulting in a stronger SH generation signal, as we experimentally demonstrated over a large range of particle separations.

8.6 CONCLUSION

In conclusion, in this Chapter we studied the role of the planar array geometry on the SH generation from gold nanoparticles. In particular we investigated periodic arrays, quasi-periodic and aperiodic arrays. We demonstrated quadrupolar SH generation from planar arrays of metal nanoparticles and its tunability with the array geometry. Moreover, we demonstrated more intense SH generation in aperiodic golden angle spiral geometry compared to the periodic one, and over a large range of particle separations. We explain this behavior by the asymmetric near-field distribution of aperiodic golden angle spiral at the pump wavelength. These results are important for the development of novel optical elements for nonlinear Nanophotonics applications, such as switchers, frequency converters and nonlinear optical sensors on a planar chip.

Part IV

CONCLUSION AND OUTLOOK

This Thesis presents novel results in the design of plasmonic nanostructures, both in the linear and the nonlinear optical regimes.

In particular, plasmonic heterostructures composed by gold and silver nanoparticles have been investigated. It has been shown that the hybrid LSPs can be tuned by changing the interparticle separation and the particle size of the elementary heterodimer. Moreover, it has been demonstrated that asymmetric heterodimers can be employed to obtain NFE peaks with equal intensity, both for the gold and the silver wavelengths. Eventually, these heterostructures can be organized in planar arrays for realizing a plasmonic substrates, and it has been shown that the array period is a further parameter to tune the optical response of the investigated heterostructures.

It has been also shown that the design of plasmonic nanostructures can be performed by using the optimization of a well-defined objective function, such as the NFE. As a result, it has been demonstrated that two different mechanisms need to be simultaneously optimized: the near-field coupling between closely spaced particles and the far-field radiative coupling of far-spaced particles. It also turned out that the building blocks for the highest NFE are isolated particles and dimers for silver and gold aggregates, respectively. The distances between these building blocks needs to be optimized to obtain constructive interference with the external field excitation. With this method, order of ten improvement over dimers and order of one hundred improvement over periodic gratings in Raman enhancement are achieved.

Importantly, in the present Thesis a full-wave analytical solution for the second-harmonic generation from a metal spherical particle of arbitrary size has been developed, extending the theories already existing in literature. In this way, a rigorous treatment of all the sources of SH radiation, located both on the surface and in the bulk of the particle is enabled. As a result, the SH radiation of gold nanospheres by using the Rudnick-Stern model for the SH sources has been investigated. In particular, the spatial distributions of the nonlinear polarization sources has been studied, which display significant symmetries due to the spherical geometry. The SH cross-section dependence on the pump wavelength demonstrates the contribution of SH multipoles up to the order $N = 6$, as the particle radius increases up to $\sim 200\ \mathrm{nm}$. Eventually, the investigated SH radiated power as function of the pump polarization angle has showed a significantly dependence on the Rudnick-Stern parameters. The application of the proposed method in combination with experimental observation, can improve the general understanding of nonlinear processes in metals, and can lead to an accurate evaluation of the weights for the different SH sources.

The relative magnitude of the nonlocal bulk and local surface contributions to the SH generation from differently-sized gold colloids has been experimentally investigated. Both surface terms, normal and tangent to the surface, are found to be strongly dependent on the particle size. Novel interference patterns between the SH dipole and octupole in the SH intensity have been shown.

Eventually, the role of the planar array geometry on the SH generation from gold nanoparticles has been investigated. A quadrupolar SH generation from planar arrays of metal nanoparticles has been shown, along with its tunability with the array geometry. A more intense SH generation in aperiodic golden angle spiral geometry compared to the periodic one has been found, due to the asymmetric near-field distribution of aperiodic golden angle spiral at the pump wavelength.

These results clearly promise the possibility to realize nanoscale photonic devices working at optical wavelengths, based on the plasmonic resonances. As a matter of fact, the LSPs in metal nanoparticles have the sufficient degree of tunability for designing real devices for applications ranging from sensing to light control. In particular, the study of the nonlinear optical effects in the metal nanostructures will enable applications of fundamental importance for the telecommunication industry.

It is worth noticing that the results obtained in the present Thesis also indicate the need for a more deep understanding of the Physics beyond light-matter interactions at nanoscale. In particular, the effects at curved metal surfaces seem to have great relevance in the optical response of plasmonic nanostructures, especially in the nonlinear regime. Moreover, a realistic design of plasmonic devices cannot disregard quantum effects of the electron-photon interaction, both in the metal bulk and at the surface.

Part V

APPENDIX

A

APPENDIX

A.1 FORMALISM

The *International System of Units* (SI) is coherently used in the present Thesis. An effort has been made to convert all the physical quantities expressed from the literature in other systems, into the SI.

All the time-domain quantities are expressed in lowercase, whereas all the frequency-domain quantities are expressed in uppercase.

All the quantities in `plaintext` are scalars, while all the quantities in ***boldtext*** are vectors. Occasionally, tensorial quantities are expressed with an upper double arrow $\overleftrightarrow{t}$.

A.2 ELECTRIC AND MAGNETIC MULTIPOLES

Given a time-harmonic polarization volume density $\boldsymbol{P}_b = \boldsymbol{P}_b(\omega, \boldsymbol{r})$ inside a domain Ω, the electric dipole $\boldsymbol{p}$, the magnetic dipole $\boldsymbol{m}$ and the electric quadrupole $\overleftrightarrow{Q}$ are defined as:

$$
\begin{aligned}
\boldsymbol{p} &= \int_\Omega \boldsymbol{P}_b \, dV \\
\boldsymbol{m} &= \frac{i\omega}{2} \int_\Omega \boldsymbol{r} \times \boldsymbol{P}_b \, dV \\
\overleftrightarrow{\boldsymbol{Q}} &= 3 \int_\Omega [\boldsymbol{P}_b \boldsymbol{r} + \boldsymbol{r} \boldsymbol{P}_b] dV - \operatorname{tr}\left(\int_\Omega [\boldsymbol{P}_b \boldsymbol{r} + \boldsymbol{r} \boldsymbol{P}_b] dV \right) \boldsymbol{I}
\end{aligned}
$$

Given a time-harmonic polarization surface density $\boldsymbol{P}_s = \boldsymbol{P}_s(\omega, \boldsymbol{r})$ over the boundary of Ω, the electric dipole $\boldsymbol{p}$, the magnetic dipole $\boldsymbol{m}$ and the electric quadrupole $\overleftrightarrow{Q}$ are:

$$
\begin{aligned}
\boldsymbol{p} &= \int_{\partial\Omega} \boldsymbol{P}_s \, dS \\
\boldsymbol{m} &= \frac{i\omega}{2} \int_{\partial\Omega} \boldsymbol{r} \times \boldsymbol{P}_s \, dS \\
\boldsymbol{Q} &= 3 \int_{\partial\Omega} [\boldsymbol{P}_s \boldsymbol{r} + \boldsymbol{r} \boldsymbol{P}_s] dS - \operatorname{tr}\left(\int_{\partial\Omega} [\boldsymbol{P}_s \boldsymbol{r} + \boldsymbol{r} \boldsymbol{P}_s] dS \right) \boldsymbol{I}
\end{aligned}
$$

The domain Ω irradiates the electric field $\boldsymbol{E} = \boldsymbol{E}(\boldsymbol{r})$ given by:

$$
\boldsymbol{E}(\boldsymbol{r}) = k^2 \frac{e^{-ikr}}{4\pi\epsilon_0 r} [\hat{\boldsymbol{r}} \times \boldsymbol{p}_{eff}(\hat{\boldsymbol{r}})] \times \hat{\boldsymbol{r}}
$$

where $\hat{\boldsymbol{r}} = \frac{\boldsymbol{r}}{|\boldsymbol{r}|}$ is a unit vector and $\boldsymbol{p}_{eff}(\hat{\boldsymbol{r}}) = \boldsymbol{p} - \frac{1}{c_0} \hat{\boldsymbol{r}} \times \boldsymbol{m} + \frac{ik}{6} \overleftrightarrow{\boldsymbol{Q}} \hat{\boldsymbol{r}}$.

A.3 SCALAR AND VECTOR SPHERICAL HARMONICS

The scalar spherical harmonics $Y_{lm}(\theta, \phi)$ [22, 145] are defined as:

$$Y_{lm}(\theta, \phi) = \sqrt{\frac{2l+1}{4\pi}\frac{(l-m)!}{(l+m)!}} P_l^m(\cos\theta) e^{im\phi}$$

where $-1 \leqslant \cos\theta \leqslant 1$, $0 \leqslant \phi \leqslant 2\pi$ and $P_l^m = P_l^m(x)$ are associated Legendre function of degree l and order m. They represent an orthonormal basis in $\mathbb{C}$.

The vector spherical harmonics $\boldsymbol{X}_{mn} = \boldsymbol{X}_{mn}(\theta, \phi)$ [22] are:

$$\begin{aligned}\boldsymbol{X}_{lm}(\theta, \phi) = i\frac{1}{\sqrt{l(l+1)}} \sqrt{\frac{2l+1}{4\pi}\frac{(l-m)!}{(l+m)!}} \cdot \\ \left[i\pi_{ml}(\cos\theta)\,\hat{\theta} - \tau_{ml}(\cos\theta)\,\hat{\phi}\right] e^{im\phi} \ ,\end{aligned}$$

where $\pi_{mn} = \pi_{mn}(x)$ and $\tau_{mn} = \tau_{mn}(x)$ are angular functions [54] defined as:

$$\begin{aligned}\pi_{mn}(\cos\theta) &= \frac{m}{\sin\theta} P_n^m(\cos\theta) \\ \tau_{mn}(\cos\theta) &= \frac{d}{d\theta} P_n^m(\cos\theta) \ .\end{aligned}$$

The vector spherical harmonics $(\boldsymbol{Y}_{JM}^{(1)}, \boldsymbol{Y}_{JM}^{(0)}, \boldsymbol{Y}_{JM}^{(-1)},)$ defined in Ref. [145] are an orthonormal basis in $\mathbb{C}^3$, and they have the following relations with $Y_{lm}(\theta, \phi)$ and $\boldsymbol{X}_{lm}(\theta, \phi)$:

$$\begin{aligned}\boldsymbol{Y}_{JM}^{(1)}(\theta, \phi) &= -i\hat{\boldsymbol{r}} \times \hat{\boldsymbol{X}}_{JM}(\theta, \phi) \\ \boldsymbol{Y}_{JM}^{(0)}(\theta, \phi) &= \hat{\boldsymbol{X}}_{JM}(\theta, \phi) \\ \boldsymbol{Y}_{JM}^{(-1)}(\theta, \phi) &= \hat{\boldsymbol{r}} Y_{JM}(\theta, \phi)\end{aligned}$$

They are suitably oriented with respect to the unit vector $\hat{\boldsymbol{r}}$, specified by the spherical coordinate system.

A.4 SCALAR PRODUCT OF SPHERICAL HARMONICS

In the following, some useful properties of the scalar products of the vector spherical harmonics $(\boldsymbol{Y}^{(1)}_{JM}, \boldsymbol{Y}^{(0)}_{JM}, \boldsymbol{Y}^{(-1)}_{JM},)$ are listed:

$$
\begin{aligned}
\boldsymbol{Y}^{(0)}_{J_1M_1} \cdot \boldsymbol{Y}^{(0)}_{J_2M_2} &= \sum_J W^{(0,0)}_{J_1M_1J_2M_2JM} \\
\boldsymbol{Y}^{(1)}_{J_1M_1} \cdot \boldsymbol{Y}^{(1)}_{J_2M_2} &= \sum_J W^{(1,1)}_{J_1M_1J_2M_2JM} \\
\boldsymbol{Y}^{(0)}_{J_1M_1} \cdot \boldsymbol{Y}^{(1)}_{J_2M_2} &= \sum_J W^{(0,1)}_{J_1M_1J_2M_2JM} \\
\boldsymbol{Y}^{(-1)}_{J_1M_1} \cdot \boldsymbol{Y}^{(-1)}_{J_2M_2} &= \sum_J W^{(-1,-1)}_{J_1M_1J_2M_2JM}
\end{aligned}
$$

where

$$
W^{(0,0)}_{J_1M_1J_2M_2JM} = W^{n_1,n_1,m_1,n_2,n_2,m_2}_{nm}
$$

$$
\begin{aligned}
W^{(0,1)}_{J_1M_1J_2M_2JM} = &\sqrt{\frac{n_2+1}{2n_2+1}} W^{n_1,n_1,m_1,n_2-1,n_2,m_2}_{nm} \\
&+ \sqrt{\frac{n_2}{2n_2+1}} W^{n_1,n_1,m_1,n_2+1,n_2,m_2}_{nm}
\end{aligned}
$$

$$
\begin{aligned}
W^{(1,1)}_{J_1M_1J_2M_2JM} = &\sqrt{\frac{n_1+1}{2n_1+1}} \sqrt{\frac{n_2+1}{2n_2+1}} W^{n_1-1,n_1,m_1,n_2-1,n_2,m_2}_{nm} \\
&+ \sqrt{\frac{n_1}{2n_1+1}} \sqrt{\frac{n_2}{2n_2+1}} W^{n_1+1,n_1,m_1,n_2+1,n_2,m_2}_{nm} \\
&+ \sqrt{\frac{n_1+1}{2n_1+1}} \sqrt{\frac{n_2}{2n_2+1}} W^{n_1-1,n_1,m_1,n_2+1,n_2,m_2}_{nm} \\
&+ \sqrt{\frac{n_1}{2n_1+1}} \sqrt{\frac{n_2+1}{2n_2+1}} W^{n_1+1,n_1,m_1,n_2-1,n_2,m_2}_{nm}
\end{aligned}
$$

$$
\begin{aligned}
W^{(-1,-1)}_{J_1M_1J_2M_2JM} = &\sqrt{\frac{n_1}{2n_1+1}} \sqrt{\frac{n_2}{2n_2+1}} W^{n_1-1,n_1,m_1,n_2-1,n_2,m_2}_{nm} \\
&+ \sqrt{\frac{n_1+1}{2n_1+1}} \sqrt{\frac{n_2+1}{2n_2+1}} W^{n_1+1,n_1,m_1,n_2+1,n_2,m_2}_{nm} \\
&- \sqrt{\frac{n_1}{2n_1+1}} \sqrt{\frac{n_2+1}{2n_2+1}} W^{n_1-1,n_1,m_1,n_2+1,n_2,m_2}_{nm} \\
&- \sqrt{\frac{n_1+1}{2n_1+1}} \sqrt{\frac{n_2}{2n_2+1}} W^{n_1+1,n_1,m_1,n_2-1,n_2,m_2}_{nm}
\end{aligned}
$$

$$W_{LM}^{L1,J1,M1,L2,J2,M2} = (-1)^{J_2+L_1+L}\sqrt{\frac{(2J_1+1)(2J_2+1)(2L_1+1)(2L_2+1)}{4\pi(2L+1)}}\cdot$$
$$\begin{Bmatrix} L_1 & L_2 & L \\ J_2 & J_1 & 1 \end{Bmatrix} C^{L0}_{L_1 0 L_2 0}\, C^{LM}_{J_1 M_1 J_2 M_2}$$

and $C^{JM}_{J_1M_1J_2M_2}$ are the Clebsch-Gordan coefficients (Chapter 8 in Ref. [145]), and the quantities in braces are Wigner 6j and 9j symbols (Chapters 9 and 10 in Ref. [145]).

A.5 VECTOR PRODUCT OF SPHERICAL HARMONICS

In the following, some useful properties of the vector products of the vector spherical harmonics ($\boldsymbol{Y}^{(1)}_{JM}, \boldsymbol{Y}^{(0)}_{JM}, \boldsymbol{Y}^{(-1)}_{JM},$) are listed:

$$\boldsymbol{Y}^{(0)}_{J_1M_1} \times \boldsymbol{Y}^{(-1)}_{J_2M_2} = \sum_J i\left[C^{(0,0,-1)}_{J_1M_1J_2M_2JM}\boldsymbol{Y}^{(0)}_{JM} + C^{(1,0,-1)}_{J_1M_1J_2M_2JM}\boldsymbol{Y}^{(1)}_{JM}\right]$$
$$\boldsymbol{Y}^{(1)}_{J_1M_1} \times \boldsymbol{Y}^{(-1)}_{J_2M_2} = \sum_J i\left[C^{(0,1,-1)}_{J_1M_1J_2M_2JM}\boldsymbol{Y}^{(0)}_{JM} + C^{(1,1,-1)}_{J_1M_1J_2M_2JM}\boldsymbol{Y}^{(1)}_{JM}\right]$$

where

$$C^{(0,0,-1)}_{J_1M_1J_2M_2JM} = \sqrt{\frac{3}{2\pi}}(2J_1+1)C^{JM}_{J_1M_1J_2M_2}\cdot$$
$$\left[\sqrt{(J_2)(2J_2-1)}\begin{Bmatrix} J_1 & J_1 & 1 \\ J_2 & J_2-1 & 1 \\ J & J & 1 \end{Bmatrix} C^{J0}_{(J_1)(0)(J_2-1)(0)}\right.$$
$$\left. -\sqrt{(J_2+1)(2J_2+3)}\begin{Bmatrix} J_1 & J_1 & 1 \\ J_2 & J_2+1 & 1 \\ J & J & 1 \end{Bmatrix} C^{J0}_{(J_1)(0)(J_2+1)(0)}\right]$$

$$
\begin{aligned}
&C^{(1,0,-1)}_{J_1M_1J_2M_2JM} = \sqrt{\frac{3}{2\pi}}(2J_1+1)C^{JM}_{J_1M_1J_2M_2}\cdot \\
&\left[\sqrt{(J_2)(2J_2-1)}\begin{Bmatrix} J_1 & J_1 & 1 \\ J_2 & J_2-1 & 1 \\ J & J+1 & 1 \end{Bmatrix} C^{(J+1)0}_{(J_1)(0)(J_2-1)(0)}\sqrt{\frac{J}{2J+1}}\right. \\
&-\sqrt{(J_2+1)(2J_2+3)}\ \begin{Bmatrix} J_1 & J_1 & 1 \\ J_2 & J_2+1 & 1 \\ J & J+1 & 1 \end{Bmatrix} C^{(J+1)0}_{(J_1)(0)(J_2+1)(0)}\sqrt{\frac{J}{2J+1}} \\
&+\sqrt{(J_2)(2J_2-1)}\begin{Bmatrix} J_1 & J_1 & 1 \\ J_2 & J_2-1 & 1 \\ J & J-1 & 1 \end{Bmatrix} C^{(J-1)0}_{(J_1)(0)(J_2-1)(0)}\sqrt{\frac{J+1}{2J+1}} \\
&\left.-\sqrt{(J_2+1)(2J_2+3)}\ \begin{Bmatrix} J_1 & J_1 & 1 \\ J_2 & J_2+1 & 1 \\ J & J-1 & 1 \end{Bmatrix} C^{(J-1)0}_{(J_1)(0)(J_2+1)(0)}\sqrt{\frac{J+1}{2J+1}}\right]
\end{aligned}
$$

$$
\begin{aligned}
&C^{(0,1,-1)}_{J_1M_1J_2M_2JM} = \sqrt{\frac{3}{2\pi}}C^{JM}_{J_1M_1J_2M_2}\cdot \\
&\left[\sqrt{(J_1+1)(J_2)(2J_1-1)(2J_2-1)}\begin{Bmatrix} J_1 & J_1-1 & 1 \\ J_2 & J_2-1 & 1 \\ J & J & 1 \end{Bmatrix} C^{J0}_{(J_1-1)(0)(J_2-1)(0)}\right. \\
&-\sqrt{(J_1+1)(J_2+1)(2J_1-1)(2J_2+3)}\begin{Bmatrix} J_1 & J_1-1 & 1 \\ J_2 & J_2+1 & 1 \\ J & J & 1 \end{Bmatrix} C^{J0}_{(J_1-1)(0)(J_2+1)(0)} \\
&+\sqrt{(J_1)(J_2)(2J_1+3)(2J_2-1)}\begin{Bmatrix} J_1 & J_1+1 & 1 \\ J_2 & J_2-1 & 1 \\ J & J & 1 \end{Bmatrix} C^{J0}_{(J_1+1)(0)(J_2-1)(0)} \\
&\left.-\sqrt{(J_1)(J_2+1)(2J_1+3)(2J_2+3)}\begin{Bmatrix} J_1 & J_1+1 & 1 \\ J_2 & J_2+1 & 1 \\ J & J & 1 \end{Bmatrix} C^{J0}_{(J_1+1)(0)(J_2+1)(0)}\right]
\end{aligned}
$$

$$
\begin{aligned}
C^{(1,1,-1)}_{J_1M_1J_2M_2JM} = \sqrt{\frac{3}{2\pi}} C^{JM}_{J_1M_1J_2M_2}\cdot \\
\Bigg[& \sqrt{(J_1+1)(J_2)(2J_1-1)(2J_2-1)} \begin{Bmatrix} J_1 & J_1-1 & 1 \\ J_2 & J_2-1 & 1 \\ J & J+1 & 1 \end{Bmatrix} C^{(J+1)0}_{(J_1-1)(0)(J_2-1)(0)} \sqrt{\frac{J}{2J+1}} \\
& -\sqrt{(J_1+1)(J_2+1)(2J_1-1)(2J_2+3)} \begin{Bmatrix} J_1 & J_1-1 & 1 \\ J_2 & J_2+1 & 1 \\ J & J+1 & 1 \end{Bmatrix} C^{(J+1)0}_{(J_1-1)(0)(J_2+1)(0)} \sqrt{\frac{J}{2J+1}} \\
& +\sqrt{(J_1)(J_2)(2J_1+3)(2J_2-1)} \begin{Bmatrix} J_1 & J_1+1 & 1 \\ J_2 & J_2-1 & 1 \\ J & J+1 & 1 \end{Bmatrix} C^{(J+1)0}_{(J_1+1)(0)(J_2-1)(0)} \sqrt{\frac{J}{2J+1}} \\
& -\sqrt{(J_1)(J_2+1)(2J_1+3)(2J_2+3)} \begin{Bmatrix} J_1 & J_1+1 & 1 \\ J_2 & J_2+1 & 1 \\ J & J+1 & 1 \end{Bmatrix} C^{(J+1)0}_{(J_1+1)(0)(J_2+1)(0)} \sqrt{\frac{J}{2J+1}} \\
& +\sqrt{(J_1+1)(J_2)(2J_1-1)(2J_2-1)} \begin{Bmatrix} J_1 & J_1-1 & 1 \\ J_2 & J_2-1 & 1 \\ J & J-1 & 1 \end{Bmatrix} C^{(J-1)0}_{(J_1-1)(0)(J_2-1)(0)} \sqrt{\frac{J+1}{2J+1}} \\
& -\sqrt{(J_1+1)(J_2+1)(2J_1-1)(2J_2+3)} \begin{Bmatrix} J_1 & J_1-1 & 1 \\ J_2 & J_2+1 & 1 \\ J & J-1 & 1 \end{Bmatrix} C^{(J-1)0}_{(J_1-1)(0)(J_2+1)(0)} \sqrt{\frac{J+1}{2J+1}} \\
& +\sqrt{(J_1)(J_2)(2J_1+3)(2J_2-1)} \begin{Bmatrix} J_1 & J_1+1 & 1 \\ J_2 & J_2-1 & 1 \\ J & J-1 & 1 \end{Bmatrix} C^{(J-1)0}_{(J_1+1)(0)(J_2-1)(0)} \sqrt{\frac{J+1}{2J+1}} \\
& -\sqrt{(J_1)(J_2+1)(2J_1+3)(2J_2+3)} \begin{Bmatrix} J_1 & J_1+1 & 1 \\ J_2 & J_2+1 & 1 \\ J & J-1 & 1 \end{Bmatrix} C^{(J-1)0}_{(J_1+1)(0)(J_2+1)(0)} \sqrt{\frac{J+1}{2J+1}} \Bigg]
\end{aligned}
$$

where $C^{JM}_{J_1M_1J_2M_2}$ are the Clebsch-Gordan coefficients (Chapter 8 in Ref. [145]), and the quantities in braces are Wigner 6j and 9j symbols (Chapters 9 and 10 in Ref. [145]).

A.6 SPHERICAL VECTOR WAVEFUNCTIONS

The spherical vector wavefunctions $\left\{\mathbf{M}_{mn}^{(J)}, \mathbf{N}_{mn}^{(J)}\right\}$ [22, 54] are:

$$\begin{aligned}\mathbf{M}_{mn}^{(J)}(kr,\theta,\phi) &= z_n^{(J)}(kr)\,\mathbf{X}_{nm}(\theta,\phi)\\ \mathbf{N}_{mn}^{(J)}(kr,\theta,\phi) &= \frac{1}{k}\nabla\times\mathbf{M}_{mn}^{(J)}\end{aligned}$$

where $z_n^{(J)} = z_n^{(J)}(kr)$,with the apices $J = 1,2,3,4$, is one of the four kinds of the spherical Bessel functions, namely:

- $z_n^{(1)}$ Bessel functions of the first kind: $j_n = j_n(kr)$
- $z_n^{(2)}$ Bessel functions of the second kind: $y_n = y_n(kr)$
- $z_n^{(3)}$ Hankel functions of the first kind: $h_n^{(1)} = h_n^{(1)}(kr)$
- $z_n^{(4)}$ Hankel functions of the second kind: $h_n^{(2)} = h_n^{(2)}(kr)$

$\mathbf{X}_{nm} = \mathbf{X}_{nm}(\theta,\phi)$ are vector spherical harmonics (see Appendix A.3). The spherical vector wavefunctions are indexed by the order m and the degree n of the vector spherical harmonics.

It is worth noticing that $\left\{\mathbf{M}_{mn}^{(J)}, \mathbf{N}_{mn}^{(J)}\right\}$ are slightly different from those $\left\{\mathbf{M}_{mn}^{(J)}, \mathbf{N}_{mn}^{(J)}\right\}^{Xu}$ defined by Xu in Ref. [54], and in particular the following relations hold:

$$\begin{aligned}\mathbf{M}_{mn}^{(J)}(\theta,\phi) &= i\frac{1}{\sqrt{l(l+1)}}\sqrt{\frac{2l+1}{4\pi}\frac{(l-m)!}{(l+m)!}}\mathbf{M}_{mn}^{(J)}(\theta,\phi)^{Xu}\\ \mathbf{N}_{mn}^{(J)}(\theta,\phi) &= i\frac{1}{\sqrt{l(l+1)}}\sqrt{\frac{2l+1}{4\pi}\frac{(l-m)!}{(l+m)!}}\mathbf{N}_{mn}^{(J)}(\theta,\phi)^{Xu}\ ,\end{aligned}$$

A.7 SURFACE ENHANCED RAMAN SCATTERING

The Raman scattering is the inelastic scattering of light with the vibrational states of an object, such as a molecule or a crystal. The scattered light is shifted in frequency to lower energy (Stokes-shifted component) and to higher energy (anti-Stokes-shifted component) with respect to the elastic component.

The scattering of a photon having energy $\hbar\omega_{inc}$, with a phonon having energy $\hbar\omega_v$ can result (Stokes shift) in a photon with lower energy $\hbar(\omega_{inc} - \omega_v)$ or (anti-Stokes shift) in a photon with higher energy $\hbar(\omega_{inc} + \omega_v)$ with respect to the incident photon, as shown in the diagram in Fig. A.1. The power P_{RS} of the Raman scattering signal is proportional to the intensity I_{inc} of the incident light:

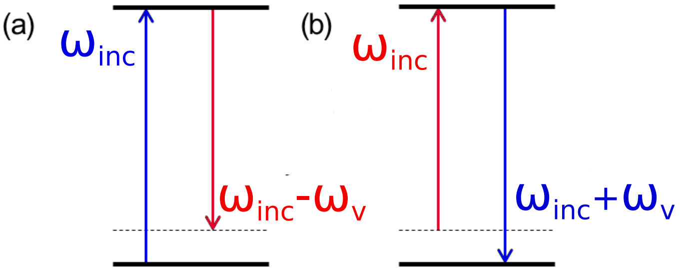

Figure A.1: An incident photon of energy $\hbar\omega_{inc}$ interacts with a vibrational mode of energy $\hbar\omega_v$, resulting in (a) Stokes and (b) anti-Stokes scattering.

$$P_{RS} = \sigma I_{inc}$$

where σ is the Raman scattering cross section. It depends on the molecule and it is typically in the range $\approx 10^{-33} - 10^{-29}\text{m}^2$, resulting in a very inefficient process.

The Raman scattering signal can be largely amplified by surface effects, for instance in proximity of plasmonic nanostructures. In fact, it has been demonstrated that the Raman scattering power depends on the local electric field E_{loc} in proximity of the vibrating molecule [90]:

$$P_{RS} \propto |E_{loc}(\omega_{inc})|^2 |E_{loc}(\omega_{inc} \pm \omega_v)|^2$$

In the approximation $|E_{loc}(\omega_{inc} \pm \omega_v)| \approx |E_{loc}(\omega_{inc})|$, the Raman scattering signal grows with the fourth power of the local electric field at the incident frequency ω_{inc}.

Since the vibrational modes of molecules are unique, the Surface Enhanced Raman Scattering (SERS) is an outstanding technique for chemical fingerprinting, and for label-free chemical and biological sensing. SERS signals have been detected down to the single molecule limit.

The SERS technique has been used in Chapter 5 to probe the near field properties of plasmonic arrays. In particular, each pattern has been excited by a 785 nm unpolarized diode laser that was fiber coupled to a $40x$ objective ($NA = 0.65$) through an upright Olympus (BX51 WI) microscope. The laser power focused through the objective was $20.5\ mW$. The back-scattered signal was sent to an electrically cooled ($-75C$) CCD (Andor DU401-BR-DD) via an Andor Shamrock 303i grating spectrometer. The grating used had 600 lines/mm blazed at $750\ \mathrm{nm}$. All spectra were averaged over 10 measurements using a $0.1\ s$ integration time. Prior to taking measurements on any enhanced substrates, the grating spectrometer was first calibrated by referencing the $520\ \mathrm{cm}^{-1}$ line of silicon.

A.8 ELECTRON-BEAM LITHOGRAPHY

The Electron Beam Lithography (EBL) has been used to fabricate the metal nanostructures investigated in Chapters 5 and 8. Oppositely to chemical fabrication processes, the EBL method is used to obtain reproducible arrays of well-defined size and shape. Although feature sizes down to $7\ \mathrm{nm}$ have been reported in literature, the devices discussed in the present Thesis require particle with a minimum edge-to-edge separation of $25\ \mathrm{nm}$ and larger diameters than $100\ \mathrm{nm}$.

EBL uses a raster scanned electron beam to pattern a resist mask with sub-micron sized features. The process flow used to fabricate samples is described in the following:

1. Sample cleaning. A quartz wafer is cleaned using an RCA clean and solvent wash. The RCA cleaning consists of two cleaning solutions, each followed by a thorough rinse in deionized (DI) water. The first solution contains ammonium hydroxide (NH_4OH) to remove organic contaminants as well as a few metals such as titanium and silver. The second solution contains hydrogen chloride (HCl) to remove many ionic contaminants such as aluminum and other metals. The solvent wash removes any remaining organic contaminants, and consists of sonication in acetone, methanol and IPA. The sample is blown dry with N_2 and baked on a hot-plate at $115^{circ}C$ to evaporate any remaining liquid.

2. Spin coating. The samples is coated with 950 PMMA A3 resist and spun at 2500 RPM. Then it is baked in an oven at $180^{\circ}C$ for 20 minutes to evaporate out the anisole solvent in the PMMA resist, providing an even coating of resist $180\ \mathrm{nm}$-thick.

3. Sacrificial metal film deposition. A sacrificial $5\ \mathrm{nm}-thick$ layer of Au is sputtered to promote conductivity between the electron-beam and the isolating SiO_2 substrate, to prevent charging.

4. Lithography. The EBL system consists of a Zeiss SUPRA 40VP SEM equipped with a Raith beam blanker and NPGS nanopat-

terning software. The $30kV$ electron beam is raster scanned over the resist by using a CAD file to determine the coordinates. The separation between the electron-beam gun and sample surface (working distance) is $6\ mm$. The measured current is in the range $35\ pA - 40\ pA$. The area dosage is in the range $250 - 400\mu C/cm^2$.

5. Sacrificial metal film etch. The sacrificial Au layer is selectively removed using Gold Etchant TFA.
6. Development. The sample is developed in a $3:1$ solution of $IPA : MIBK$ for 70 seconds. Then it is rinsed in neat IPA and blown dry with N_2.
7. Metal deposition. The sample is ashed in O_2 flow at $200sccm$ for 25 seconds using a PVA TePla America M4L plasma asher at $200W$ RF power. A $2\ nm$ Ti adhesion layer and a $28\ nm$ Au film are evaporated using the electron-beam evaporation with a CHA Solution controlled by a Sycon STC-2000A deposition rate controller. This evaporation method makes use of an electron-beam focused onto a metal-filled crucible under very low pressure (around 1 x 10-6 torr), which heats up to the evaporation temperature and deposits on the substrate. The sample mount rotates to ensure a uniform coverage of metal across the planar surface of the samples. i
8. Liftoff. The sample is agitated in acetone to dissolve the PMMA for 2 minutes. Then it is sonicated for 30 seconds to remove the PMMA and it is dried in N_2.

BIBLIOGRAPHY

[1] Jensen Li and C. T. Chan. Double-negative acoustic metamaterial. *Phys. Rev. E*, 70:055602, Nov 2004.

[2] Shu Zhang, Leilei Yin, and Nicholas Fang. Focusing ultrasound with an acoustic metamaterial network. *Phys. Rev. Lett.*, 102:194301, May 2009.

[3] D. R. Smith, J. B. Pendry, and M. C. K. Wiltshire. Metamaterials and negative refractive index. *Science*, 305(5685):788–792, 2004.

[4] Vladimir M. Shalaev. Optical negative-index metamaterials. *Nat Photon*, 1:41,48, 2007.

[5] I. Brodie and J.J. Muray. *The Physics of Micro/Nano-Fabrication*. Microdevices : Physics and Fabrication Technologies. Springer, 1993.

[6] Yong Chen and Anne Pepin. Nanofabrication: Conventional and nonconventional methods. *Electrophoresis*, 22(2):187–207, 2001.

[7] Shuguang Zhang. Fabrication of novel biomaterials through molecular self-assembly. *Nat Biotech*, 21:1171,1178, 2003.

[8] Claudio De Rosa, Cheolmin Park, Edwin L. Thomas, and Bernard Lotz. Microdomain patterns from directional eutectic solidification and epitaxy. *Nature*, 405:433,437, 2000.

[9] Sung Ha Park, Peng Yin, Yan Liu, John H. Reif, Thomas H. LaBean, and Hao Yan. Programmable dna self-assemblies for nanoscale organization of ligands and proteins. *Nano Letters*, 5(4):729–733, 2005.

[10] Shawn M. Douglas, Hendrik Dietz, Tim Liedl, Bjorn Hogberg, Franziska Graf, and William M. Shih. Self-assembly of dna into nanoscale three-dimensional shapes. *Nature*, 459:414,418, 2009.

[11] H.J. Levinson. *Principles Of Lithography*. Press Monographs. Society of Photo Optical, 2005.

[12] Wei Chen and Haroon Ahmed. Fabrication of 5-7 nm wide etched lines in silicon using 100 kev electron beam lithography and polymethylmethacrylate resist. *Applied Physics Letters*, 62(13):1499 –1501, mar 1993.

[13] C. Vieu, F. Carcenac, A. Pepin, Y. Chen, M. Mejias, A. Lebib, L. Manin-Ferlazzo, L. Couraud, and H. Launois. Electron beam lithography: resolution limits and applications. *Applied Surface Science*, 164(1,4):111,117, 2000.

[14] H. W. Kroto, J. R. Heath, S. C. O'Brien, R. F. Curl, and R. E. Smalley. C60: Buckminsterfullerene. *Nature*, 318:162,163, 1985.

[15] Adrian Bachtold, Peter Hadley, Takeshi Nakanishi, and Cees Dekker. Logic circuits with carbon nanotube transistors. *Science*, 294(5545):1317–1320, 2001.

[16] A. K. Geim and K. S. Novoselov. The rise of graphene. *Nat Mater*, 6:183,191, 2007.

[17] A. N. Grigorenko, M. Polini, and K. S. Novoselov. Graphene plasmonics. *Nat Photon*, 6:749,758, 2012.

[18] B. Bhushan. *Springer Handbook of Nanotechnology*. Gale virtual reference library. Springer Science+Business Media, Incorporated, 2007.

[19] Z. Cui. *Nanofabrication: Principles, Capabilities and Limits*. Springer London, Limited, 2008.

[20] Vladimir M. Shalaev, Wenshan Cai, Uday K. Chettiar, Hsiao-Kuan Yuan, Andrey K. Sarychev, Vladimir P. Drachev, and Alexander V. Kildishev. Negative index of refraction in optical metamaterials. *Opt. Lett.*, 30(24):3356–3358, Dec 2005.

[21] V. G. Veselago. The electrodynamics of substances with simultaneously negative values of ϵ and μ. *Physics-Uspekhi*, 10(4):509–514, 1968.

[22] J.D. Jackson. *Classical Electrodynamics*. Wiley, 1998.

[23] C. Kittel. *Introduction to Solid State Physics, 7th Ed*. Wiley India Pvt. Limited, 2007.

[24] C. Kittel. *Quantum Theory of Solids*. Wiley, 1987.

[25] J.A. Stratton. *Electromagnetic Theory*. IEEE Press Series on Electromagnetic Wave Theory. Wiley, 2007.

[26] J.G. Van Bladel. *Electromagnetic Fields*. IEEE Press Series on Electromagnetic Wave Theory. John Wiley & Sons, 2007.

[27] C.F. Bohren and D.R. Huffman. *Absorption and Scattering of Light by Small Particles*. Wiley Science Series. Wiley, 2008.

[28] Katrin Kneipp, Yang Wang, Harald Kneipp, Lev T. Perelman, Irving Itzkan, Ramachandra R. Dasari, and Michael S. Feld. Single molecule detection using surface-enhanced raman scattering (sers). *Phys. Rev. Lett.*, 78:1667–1670, Mar 1997.

[29] Brian K. Canfield, Hannu Husu, Janne Laukkanen, Benfeng Bai, Markku Kuittinen, Jari Turunen, and Martti Kauranen. Local field asymmetry drives second-harmonic generation in noncentrosymmetric nanodimers. *Nano Letters*, 7(5):1251–1255, 2007.

[30] J.B. Pendry, A.J. Holden, D.J. Robbins, and W.J. Stewart. Magnetism from conductors and enhanced nonlinear phenomena. *Microwave Theory and Techniques, IEEE Transactions on*, 47(11):2075 –2084, nov 1999.

[31] D. R. Smith, Willie J. Padilla, D. C. Vier, S. C. Nemat-Nasser, and S. Schultz. Composite medium with simultaneously negative permeability and permittivity. *Phys. Rev. Lett.*, 84:4184–4187, May 2000.

[32] R. A. Shelby, D. R. Smith, and S. Schultz. Experimental verification of a negative index of refraction. *Science*, 292(5514):77–79, 2001.

[33] J. B. Pendry. Negative refraction makes a perfect lens. *Phys. Rev. Lett.*, 85:3966–3969, Oct 2000.

[34] Katrin Kneipp, Harald Kneipp, Ramasamy Manoharan, Eugene B. Hanlon, Irving Itzkan, Ramachandra R. Dasari, and Michael S. Feld. Extremely large enhancement factors in surface-enhanced raman scattering for molecules on colloidal gold clusters. *Appl. Spectrosc.*, 52(12):1493–1497, Dec 1998.

[35] Alec Rose, Da Huang, and David R. Smith. Controlling the second harmonic in a phase-matched negative-index metamaterial. *Phys. Rev. Lett.*, 107:063902, Aug 2011.

[36] V. Volterra. *Theory Of Functionals And Of Integral And Integro-differential Equations*. Dover Phoenix Editions. Dover Publications, 2005.

[37] Alexandre Vial, Anne-Sophie Grimault, Demetrio Macias, Dominique Barchiesi, and Marc Lamy de la Chapelle. Improved analytical fit of gold dispersion: application to the modeling of extinction spectra with a finite-difference time-domain method. *Phys. Rev. B*, 71:085416, Feb 2005.

[38] P. B. Johnson and R. W. Christy. Optical constants of the noble metals. *Phys. Rev. B*, 6:4370–4379, Dec 1972.

[39] R.W. Boyd. *Nonlinear Optics*. Academic Press. Elsevier Science, 2008.

[40] S.A. Maier. *Plasmonics: Fundamentals and Applications*. Springer, 2007.

[41] L. Novotny and B. Hecht. *Principles of Nano-Optics*. Principles of Nano-optics. Cambridge University Press, 2006.

[42] Joseph Rudnick and E. A. Stern. Second-harmonic radiation from metal surfaces. *Phys. Rev. B*, 4:4274–4290, Dec 1971.

[43] J. E. Sipe, V. C. Y. So, M. Fukui, and G. I. Stegeman. Analysis of second-harmonic generation at metal surfaces. *Phys. Rev. B*, 21:4389–4402, May 1980.

[44] M. Corvi and W. L. Schaich. Hydrodynamic-model calculation of second-harmonic generation at a metal surface. *Phys. Rev. B*, 33:3688–3695, Mar 1986.

[45] Xiao Ming Hua and Joel I. Gersten. Theory of second-harmonic generation by small metal spheres. *Phys. Rev. B*, 33:3756–3764, Mar 1986.

[46] Y.R. Shen. *The principles of nonlinear optics*. Wiley classics library. Wiley-Interscience, 2003.

[47] A. V. Petukhov. Sum-frequency generation on isotropic surfaces: General phenomenology and microscopic theory for jellium surfaces. *Phys. Rev. B*, 52:16901–16911, Dec 1995.

[48] N. Bloembergen, R. K. Chang, S. S. Jha, and C. H. Lee. Optical second-harmonic generation in reflection from media with inversion symmetry. *Phys. Rev.*, 174:813–822, Oct 1968.

[49] P. Guyot-Sionnest and Y. R. Shen. Bulk contribution in surface second-harmonic generation. *Phys. Rev. B*, 38:7985–7989, Oct 1988.

[50] J. E. Sipe, V. Mizrahi, and G. I. Stegeman. Fundamental difficulty in the use of second-harmonic generation as a strictly surface probe. *Phys. Rev. B*, 35:9091–9094, June 1987.

[51] Fu Xiang Wang, Francisco J. Rodriguez, Willem M. Albers, Risto Ahorinta, J. E. Sipe, and Martti Kauranen. Surface and bulk contributions to the second-order nonlinear optical response of a gold film. *Phys. Rev. B*, 80:233402, Dec 2009.

[52] G. Bachelier, J. Butet, I. Russier-Antoine, C. Jonin, E. Benichou, and P.-F. Brevet. Origin of optical second-harmonic generation in spherical gold nanoparticles: Local surface and nonlocal bulk contributions. *Phys. Rev. B*, 82:235403, Dec 2010.

[53] Gustav Mie. BeitrÃ€ge zur optik trÃŒber medien, speziell kolloidaler metallÃ¶sungen. *Ann. Phys.*, 330:377–445, 1908.

[54] Yu lin Xu. Electromagnetic scattering by an aggregate of spheres. *Appl. Opt.*, 34(21):4573–4588, Jul 1995.

[55] Alessio Benedetti, Marco Centini, Mario Bertolotti, and Concita Sibilia. Second harmonic generation from 3d nanoantennas: on the surface and bulk contributions by far-field pattern analysis. *Opt. Express*, 19(27):26752–26767, Dec 2011.

[56] Cristian Ciracì, Ekaterina Poutrina, Michael Scalora, and David R. Smith. Second-harmonic generation in metallic nanoparticles: Clarification of the role of the surface. *Phys. Rev. B*, 86:115451, Sep 2012.

[57] M. Scalora, M. A. Vincenti, D. de Ceglia, V. Roppo, M. Centini, N. Akozbek, and M. J. Bloemer. Second- and third-harmonic generation in metal-based structures. *Phys. Rev. A*, 82:043828, Oct 2010.

[58] Yong Zeng, Walter Hoyer, Jinjie Liu, Stephan W. Koch, and Jerome V. Moloney. Classical theory for second-harmonic generation from metallic nanoparticles. *Phys. Rev. B*, 79:235109, Jun 2009.

[59] Sami Kujala, Brian K. Canfield, Martti Kauranen, Yuri Svirko, and Jari Turunen. Multipole interference in the second-harmonic optical radiation from gold nanoparticles. *Phys. Rev. Lett.*, 98:167403, Apr 2007.

[60] Hannu Husu, Roope Siikanen, Jouni MÃ€kitalo, Joonas Lehtolahti, Janne Laukkanen, Markku Kuittinen, and Martti Kauranen. Metamaterials with tailored nonlinear optical response. *Nano Letters*, 12(2):673–677, 2012.

[61] Jerry I. Dadap, Jie Shan, and Tony F. Heinz. Theory of optical second-harmonic generation from a sphere of centrosymmetric material: small-particle limit. *J. Opt. Soc. Am. B*, 21(7):1328–1347, Jul 2004.

[62] M. Finazzi, P. Biagioni, M. Celebrano, and L. Duò. Selection rules for second-harmonic generation in nanoparticles. *Phys. Rev. B*, 76:125414, Sep 2007.

[63] Lisa V. Brown, Heidar Sobhani, J. Britt Lassiter, Peter Nordlander, and Naomi J. Halas. Heterodimers: Plasmonic properties of mismatched nanoparticle pairs. *ACS Nano*, 4(2):819–832, 2010. PMID: 20092361.

[64] Sassan Sheikholeslami, Young-wook Jun, Prashant K. Jain, and A. Paul Alivisatos. Coupling of optical resonances in a compositionally asymmetric plasmonic nanoparticle dimer. *Nano Letters*, 10(7):2655–2660, 2010.

[65] Timur Shegai, Si Chen, Vladimir D. Miljkovic, Gulis Zengin, Peter Johansson, and Mikael Kall. A bimetallic nanoantenna for directional colour routing. *Nat. Commun.*, 2:481, 2011.

[66] Tal Ellenbogen, Kwanyong Seo, and Kenneth B. Crozier. Chromatic plasmonic polarizers for active visible color filtering and polarimetry. *Nano Letters*, 12(2):1026–1031, 2012.

[67] P. Nordlander, C. Oubre, E. Prodan, K. Li, and M. I. Stockman. Plasmon hybridization in nanoparticle dimers. *Nano Letters*, 4(5):899–903, 2004.

[68] E. Prodan, C. Radloff, N. J. Halas, and P. Nordlander. A hybridization model for the plasmon response of complex nanostructures. *Science*, 302(5644):419–422, 2003.

[69] Daniel W. Brandl, Chris Oubre, and Peter Nordlander. Plasmon hybridization in nanoshell dimers. *The Journal of Chemical Physics*, 123(2):024701, 2005.

[70] Jon A. Schuller, Edward S. Barnard, Wenshan Cai, Young Chul Jun, Justin S. White, and Mark L. Brongersma. Plasmonics for extreme light concentration and manipulation. *Nat. Mater.*, 9:193–204, 2010.

[71] Harry A Atwater and Albert Polman. Plasmonics for improved photovoltaic devices. *Nat. Mater.*, 9:205–213, 2010.

[72] Liang Tang, Sukru Ekin Kocabas, Salman Latif, Ali K. Okyay, Dany-Sebastien Ly-Gagnon, Krishna C. Saraswat, and David A. B. Miller. Nanometre-scale germanium photodetector enhanced by a near-infrared dipole antenna. *Nat. Photon.*, 2:226–229, 2008.

[73] A. N. Grigorenko, N. W. Roberts, M. R. Dickinson, and Y. Zhang. Nanometric optical tweezers based on nanostructured substrates. *Nat. Photon.*, 2:365–370, 2008.

[74] Thomas Nikolajsen, Kristjan Leosson, and Sergey I. Bozhevolnyi. Surface plasmon polariton based modulators and switches operating at telecom wavelengths. *Applied Physics Letters*, 85(24):5833–5835, 2004.

[75] Jon A. Schuller, Thomas Taubner, and Mark L. Brongersma. Optical antenna thermal emitters. *Nat. Photon.*, 3:658–661, 2009.

[76] Martin Moskovits. Surface-enhanced spectroscopy. *Rev. Mod. Phys.*, 57:783–826, Jul 1985.

[77] Satoshi Kawata, Yasushi Inouye, and Prabhat Verma. Plasmonics for near-field nano-imaging and superlensing. *Nat. Photon.*, 3:388–394, 2009.

[78] H. J. Simon, D. E. Mitchell, and J. G. Watson. Optical second-harmonic generation with surface plasmons in silver films. *Phys. Rev. Lett.*, 33:1531–1534, Dec 1974.

[79] Kuiru Li, Mark I. Stockman, and David J. Bergman. Self-similar chain of metal nanospheres as an efficient nanolens. *Phys. Rev. Lett.*, 91:227402, Nov 2003.

[80] Jianhua Dai, Frantisek Čajko, Igor Tsukerman, and Mark I. Stockman. Electrodynamic effects in plasmonic nanolenses. *Phys. Rev. B*, 77:115419, Mar 2008.

[81] Shengli Zou and George C. Schatz. Silver nanoparticle array structures that produce giant enhancements in electromagnetic fields. *Chemical Physics Letters*, 403(13):62 – 67, 2005.

[82] Pavel Ginzburg, Nikolai Berkovitch, Amir Nevet, Itay Shor, and Meir Orenstein. Resonances on-demand for plasmonic nanoparticles. *Nano Letters*, 11(6):2329–2333, 2011.

[83] Carlo Forestiere, Massimo Donelli, Gary F. Walsh, Edoardo Zeni, Giovanni Miano, and Luca Dal Negro. Particle-swarm optimization of broadband nanoplasmonic arrays. *Opt. Lett.*, 35(2):133–135, Jan 2010.

[84] E.K.P. Chong and S.H. Zak. *An Introduction to Optimization*. Wiley Series in Discrete Mathematics and Optimization. Wiley, 2011.

[85] S.N. Sivanandam and S.N. Deepa. *Introduction to Genetic Algorithms*. Springer, 2010.

[86] A. Boag, A. Boag, E. Michielssen, and R. Mittra. Design of electrically loaded wire antennas using genetic algorithms. *Antennas and Propagation, IEEE Transactions on*, 44(5):687, may 1996.

[87] R.L. Haupt. An introduction to genetic algorithms for electromagnetics. *Antennas and Propagation Magazine, IEEE*, 37(2):7 –15, apr 1995.

[88] J. B. Jackson and N. J. Halas. Surface-enhanced raman scattering on tunable plasmonic nanoparticle substrates. *Proceedings of the National Academy of Sciences*, 101(52):17930–17935, 2004.

[89] Yizhuo Chu, Mohamad G. Banaee, and Kenneth B. Crozier. Double-resonance plasmon substrates for surface-enhanced raman scattering with enhancement at excitation and stokes frequencies. *ACS Nano*, 4(5):2804–2810, 2010.

[90] Mohamad G. Banaee and Kenneth B. Crozier. Mixed dimer double-resonance substrates for surface-enhanced raman spectroscopy. *ACS Nano*, 5(1):307–314, 2011.

[91] Chad E. Talley, Joseph B. Jackson, Chris Oubre, Nathaniel K. Grady, Christopher W. Hollars, Stephen M. Lane, Thomas R. Huser, Peter Nordlander, and Naomi J. Halas. Surface-enhanced raman scattering from individual au nanoparticles and nanoparticle dimer substrates. *Nano Letters*, 5(8):1569–1574, 2005.

[92] Matthew Rycenga, Pedro H. C. Camargo, Weiyang Li, Christine H. Moran, and Younan Xia. Understanding the sers effects of single silver nanoparticles and their dimers, one at a time. *The Journal of Physical Chemistry Letters*, 1(4):696–703, 2010.

[93] Encai Hao and George C. Schatz. Electromagnetic fields around silver nanoparticles and dimers. *The Journal of Chemical Physics*, 120(1):357–366, 2004.

[94] David P. Fromm, Arvind Sundaramurthy, Anika Kinkhabwala, P. James Schuck, Gordon S. Kino, and W. E. Moerner. Exploring the chemical enhancement for surface-enhanced raman scattering with au bowtie nanoantennas. *The Journal of Chemical Physics*, 124(6):061101, 2006.

[95] Nahla A. Hatab, Chun-Hway Hsueh, Abigail L. Gaddis, Scott T. Retterer, Jia-Han Li, Gyula Eres, Zhenyu Zhang, and Baohua Gu. Free-standing optical gold bowtie nanoantenna with variable gap size for enhanced raman spectroscopy. *Nano Letters*, 10(12):4952–4955, 2010.

[96] Ashwin Gopinath, Svetlana V. Boriskina, Bjorn M. Reinhard, and Luca Dal Negro. Deterministic aperiodic arrays of metal nanoparticles for surface-enhanced raman scattering (sers). *Opt. Express*, 17(5):3741–3753, Mar 2009.

[97] Ashwin Gopinath, Svetlana V. Boriskina, W. Ranjith Premasiri, Lawrence Ziegler, Bjorn M. Reinhard, and Luca Dal Negro. Plasmonic nanogalaxies: Multiscale aperiodic arrays for surface-enhanced raman sensing. *Nano Letters*, 9(11):3922–3929, 2009.

[98] Bo Yan, Anupama Thubagere, W. Ranjith Premasiri, Lawrence D. Ziegler, Luca Dal Negro, and Bjorn M. Reinhard. Engineered sers substrates with multiscale signal enhancement: Nanoparticle cluster arrays. *ACS Nano*, 3(5):1190–1202, 2009. PMID: 19354266.

[99] Alyssa J. Pasquale, Bjorn M. Reinhard, and Luca Dal Negro. Engineering photonic-plasmonic coupling in metal nanoparticle necklaces. *ACS Nano*, 5(8):6578–6585, 2011.

[100] Zihua Zhu, Tao Zhu, and Zhongfan Liu. Raman scattering enhancement contributed from individual gold nanoparticles and interparticle coupling. *Nanotechnology*, 15(3):357, 2004.

[101] Heykel Aouani, Miguel Navarro-Cia, Mohsen Rahmani, Themistoklis P. H. Sidiropoulos, Minghui Hong, Rupert F. Oulton, and Stefan A. Maier. Multiresonant broadband optical antennas as efficient tunable nanosources of second harmonic light. *Nano Letters*, 12(9):4997–5002, 2012.

[102] Jeremy Butet, Julien Duboisset, Guillaume Bachelier, Isabelle Russier-Antoine, Emmanuel Benichou, Christian Jonin, and Pierre-FrancÌ§ois Brevet. Optical second harmonic generation of single metallic nanoparticles embedded in a homogeneous medium. *Nano Letters*, 10(5):1717–1721, 2010.

[103] Antonio Capretti, Gary F. Walsh, Salvatore Minissale, Jacob Trevino, Carlo Forestiere, Giovanni Miano, and Luca Dal Negro. Multipolar second harmonic generation from planar arrays of au nanoparticles. *Opt. Express*, 20(14):15797–15806, Jul 2012.

[104] C. G. Biris and N. C. Panoiu. Second harmonic generation in metamaterials based on homogeneous centrosymmetric nanowires. *Phys. Rev. B*, 81:195102, May 2010.

[105] Martti Kauranen and Anatoly V. Zayats. Nonlinear plasmonics. *Nat. Photon.*, 6:737–748, 2012.

[106] L. Tong and J.X. Cheng. Label-free imaging through nonlinear optical signals. *Materials Today*, 14(6):264–273, 2011.

[107] Grazia Gonella and Hai-Lung Dai. Determination of adsorption geometry on spherical particles from nonlinear mie theory analysis of surface second harmonic generation. *Phys. Rev. B*, 84:121402, Sep 2011.

[108] TF Heinz. Second-order nonlinear optical effects at surfaces and interfaces. In H.E. Ponath and G.I. Stegeman, editors, *Nonlinear surface electromagnetic phenomena*, Modern problems in condensed matter sciences, chapter 5, pages 353–416. North-Holland, 1991.

[109] G.S. Agarwal and S.S. Jha. Theory of second harmonic generation at a metal surface with surface plasmon excitation. *Solid State Communications*, 41(6):499 – 501, 1982.

[110] J. I. Dadap, J. Shan, K. B. Eisenthal, and T. F. Heinz. Second-harmonic rayleigh scattering from a sphere of centrosymmetric material. *Phys. Rev. Lett.*, 83:4045–4048, Nov 1999.

[111] P. Guyot-Sionnest, W. Chen, and Y. R. Shen. General considerations on optical second-harmonic generation from surfaces and interfaces. *Phys. Rev. B*, 33:8254–8263, Jun 1986.

[112] P. Guyot-Sionnest and Y. R. Shen. Local and nonlocal surface nonlinearities for surface optical second-harmonic generation. *Phys. Rev. B*, 35:4420–4426, Mar 1987.

[113] Vera L. Brudny, Bernardo S. Mendoza, and W. Luis Mochán. Second-harmonic generation from spherical particles. *Phys. Rev. B*, 62:11152–11162, Oct 2000.

[114] Y. Pavlyukh and W. Hübner. Nonlinear mie scattering from spherical particles. *Phys. Rev. B*, 70:245434, Dec 2004.

[115] Jinying Xu and Xiangdong Zhang. Second harmonic generation in three-dimensional structures based on homogeneous centrosymmetric metallic spheres. *Opt. Express*, 20(2):1668–1684, Jan 2012.

[116] Carlo Forestiere, Antonio Capretti, and Giovanni Miano. Surface Integral Method for the Second Harmonic Generation in Metal Nanoparticles. arXiv 1301.1880 [physics.optics], 2013.

[117] Cristian Ciracì, Ekaterina Poutrina, Michael Scalora, and David R. Smith. Origin of second-harmonic generation enhancement in optical split-ring resonators. *Phys. Rev. B*, 85:201403, May 2012.

[118] M. Centini, A. Benedetti, M. Scalora, C. Sibilia, and M. Bertolotti. Second harmonic generation from metallic 2d scatterers. In *Proc. SPIE 7354*, Nonlinear Optics and Applications III, May 2009.

[119] Grazia Gonella, Wei Gan, Bolei Xu, and Hai-Lung Dai. The effect of composition, morphology, and susceptibility on nonlinear light scattering from metallic and dielectric nanoparticles. *The Journal of Physical Chemistry Letters*, 3(19):2877–2881, 2012.

[120] R. Almeida, C.A. Barrios, R. Panepucci, and M. Lipson. All-optical control of light on a silicon chip. *Nature*, 431:1081–1084, Oct 2004.

[121] Fu Xiang Wang, Francisco J RodrÃguez, Willem M Albers, and Martti Kauranen. Enhancement of bulk-type multipolar second-harmonic generation arising from surface morphology of metals. *New Journal of Physics*, 12(6):063009, 2010.

[122] Antonio Capretti, Carlo Forestiere, Luca Dal Negro, and Giovanni Miano. Second harmonic generation in metal nano-spheres: full-wave analytical solution with both local-surface and nonlocal-bulk nonlinear sources. arXiv 1301.1628 [physics.optics], 2013.

[123] J. Butet, G. Bachelier, I. Russier-Antoine, C. Jonin, E. Benichou, and P.-F. Brevet. Interference between selected dipoles and octupoles in the optical second-harmonic generation from spherical gold nanoparticles. *Phys. Rev. Lett.*, 105:077401, Aug 2010.

[124] B. Lamprecht, A. Leitner, and F.R. Aussenegg. Shg studies of plasmon dephasing in nanoparticles. *Applied Physics B*, 68:419–423, 1999.

[125] Brian K Canfield, Sami Kujala, Konstantins Jefimovs, Tuomas Vallius, Jari Turunen, and Martti Kauranen. Polarization effects in the linear and nonlinear optical responses of gold nanoparticle arrays. *Journal of Optics A: Pure and Applied Optics*, 7(2):S110, 2005.

[126] M. D. McMahon, R. Lopez, R. F. Haglund, E. A. Ray, and P. H. Bunton. Second-harmonic generation from arrays of symmetric gold nanoparticles. *Phys. Rev. B*, 73:041401, Jan 2006.

[127] M.D. McMahon, D. Ferrara, C.T. Bowie, R. Lopez, and R.F. Haglund Jr. Second harmonic generation from resonantly excited arrays of gold nanoparticles. *Applied Physics B*, 87:259–265, 2007.

[128] Ch. Awada, F. Kessi, Ch. Jonin, P. M. Adam, S. Kostcheev, R. Bachelot, P. Royer, I. Russier-Antoine, E. Benichou, G. Bachelier, and P. F. Brevet. On- and off-axis second harmonic generation from an array of gold metallic nanocylinders. *Journal of Applied Physics*, 110(2):023109, 2011.

[129] M. Breit, V. A. Podolskiy, S. Grésillon, G. von Plessen, J. Feldmann, J. C. Rivoal, P. Gadenne, Andrey K. Sarychev, and Vladimir M. Shalaev. Experimental observation of percolation-enhanced nonlinear light scattering from semicontinuous metal films. *Phys. Rev. B*, 64:125106, Sep 2001.

[130] Ramona Dallapiccola, Ashwin Gopinath, Francesco Stellacci, and Luca Dal Negro. Quasi-periodic distribution of plasmon modes in two-dimensional fibonacci arrays of metal nanoparticles. *Opt. Express*, 16(8):5544–5555, Apr 2008.

[131] Luca Dal Negro, Ning-Ning Feng, and Ashwin Gopinath. Electromagnetic coupling and plasmon localization in deterministic aperiodic arrays. *Journal of Optics A: Pure and Applied Optics*, 10(6):064013, 2008.

[132] Ashwin Gopinath, Svetlana V. Boriskina, Ning-Ning Feng, Bjorn M. Reinhard, and Luca Dal Negro. Photonic-plasmonic scattering resonances in deterministic aperiodic structures. *Nano Letters*, 8(8):2423–2431, 2008. PMID: 18646833.

[133] L. Dal Negro and S.V. Boriskina. Deterministic aperiodic nanostructures for photonics and plasmonics applications. *Laser & Photonics Reviews*, 6(2):178–218, 2012.

[134] Jacob Trevino, Hui Cao, and Luca Dal Negro. Circularly symmetric light scattering from nanoplasmonic spirals. *Nano Letters*, 11(5):2008–2016, 2011.

[135] Jacob Trevino, Seng Fatt Liew, Heeso Noh, Hui Cao, and Luca Dal Negro. Geometrical structure, multifractal spectra and localized optical modes of aperiodic vogel spirals. *Opt. Express*, 20(3):3015–3033, Jan 2012.

[136] Seng Fatt Liew, Heeso Noh, Jacob Trevino, Luca Dal Negro, and Hui Cao. Localized photonic band edge modes and orbital angular momenta of light in a golden-angle spiral. *Opt. Express*, 19(24):23631–23642, Nov 2011.

[137] A. Doicu, T. Wriedt, and Y.A. Eremin. *Light Scattering by Systems of Particles: Null-Field Method with Discrete Sources: Theory and Programs*. Springer Series in Optical Sciences. Springer, 2006.

[138] Carlo Forestiere, Giovanni Iadarola, Luca Dal Negro, and Giovanni Miano. Near-field calculation based on the t-matrix method with discrete sources. *Journal of Quantitative Spectroscopy and Radiative Transfer*, 112(14):2384 – 2394, 2011.

[139] H. Raether. *Surface plasmons on smooth and rough surfaces and on gratings*. Number v. 111 in Springer tracts in modern physics. Springer, 1988.

[140] G. D'Aguanno, N. Mattiucci, M. J. Bloemer, D. de Ceglia, M. A. Vincenti, and A. Alù. Transmission resonances in plasmonic metallic gratings. *J. Opt. Soc. Am. B*, 28(2):253–264, Feb 2011.

[141] J. Nappa, G. Revillod, I. Russier-Antoine, E. Benichou, C. Jonin, and P. F. Brevet. Electric dipole origin of the second harmonic generation of small metallic particles. *Phys. Rev. B*, 71:165407, Apr 2005.

[142] Guillaume Bachelier, Isabelle Russier-Antoine, Emmanuel Benichou, Christian Jonin, and Pierre-François Brevet. Multipolar second-harmonic generation in noble metal nanoparticles. *J. Opt. Soc. Am. B*, 25(6):955–960, Jun 2008.

[143] Jeremy Butet, Isabelle Russier-Antoine, Christian Jonin, Noelle Lascoux, Emmanuel Benichou, and Pierre-Francois Brevet. Sensing with multipolar second harmonic generation from spherical metallic nanoparticles. *Nano Letters*, 12(3):1697–1701, 2012.

[144] G. T. Boyd, Z. H. Yu, and Y. R. Shen. Photoinduced luminescence from the noble metals and its enhancement on roughened surfaces. *Phys. Rev. B*, 33:7923–7936, Jun 1986.

[145] D.A. Varshalovich, A.N. Moskalev, and V.K. Khersonski. *Quantum Theory of Angular Momentum: Irreducible Tensors, Spherical Harmonics, Vector Coupling Coefficients, 3nj Symbols*. World Scientific Pub., 1988.

Antonio Capretti: *Linear and Nonlinear Plasmonics,* Dissertation submitted in partial fulfillment of the requirements for the Doctoral Degree in Electrical Engineering, March 31st, 2013